SOIL EFFECTIVE TEMPERATURE AND ITS APPLICATION IN PASSIVE REMOTE SENSING OF SOIL MOISTURE AT L-BAND

Shaoning Lv

SOIL EFFECTIVE TEMPERATURE AND ITS APPLICATION IN PASSIVE REMOTE SENSING OF SOIL MOISTURE AT L-BAND

DISSERTATION

to obtain
the degree of doctor at the University of Twente,
on the authority of the rector magnificus,
prof.dr. T.T.M. Palstra
on account of the decision of the Doctorate Board,
to be publicly defended
on Wednesday 10 April 2019 at 12.45 hrs

By

Shaoning Lv

born on 8 May 1985

in Neimongol, China

This thesis has been approved by
Prof.dr. Z. Su, supervisor
Prof.dr. J. Wen, supervisor
Dr. Y. Zeng, co-supervisor

ITC dissertation number 347
ITC, P.O. Box 217, 7500 AE Enschede, The Netherlands

ISBN 978-90-365-4749-9
DOI 10.3990/1.9789036547499

Cover designed by Job Duim
Printed by ITC Printing Department

UNIVERSITY OF TWENTE.

FACULTY OF GEO-INFORMATION SCIENCE AND EARTH OBSERVATION

Graduation committee:

Chairman/Secretary

Prof.dr.ir. A. Veldkamp	

Supervisors

Prof.dr. Z. Su	University of Twente
Prof.dr. J. Wen	Chengdu University of Information Technology

Co-supervisor

Dr. Y. Zeng	University of Twente

Members

Prof.dr. D. van der Wal	University of Twente
Prof.dr. N. Kerle	University of Twente
Prof.dr. C. Simmer	Bonn University
Prof.dr. Y. Kerr	CESBIO, SMOS Mission PI
Dr. S. Yueh	NASA/Jet Propulsion Laboratory
Dr. P. de Rosnay	European Centre for Medium Range Weather Forecasts (ECMWF)

Acknowledgments

Studying overseas was never my dream, but it turned out to be even better than a dream.

When I was a baby, my parents were wondering what kind of person I would be. I know deep in my heart that they wanted me to stay healthy and grow up. Both of my parents are engineers, and they hoped I would go to the same university and study the same subject as my father did in 1978. However, I failed in their expectation and chose Nanjing Institute of Meteorology (NIM) for my college in 2004. NIM is just an incidental choice for me at that time but a life choice afterward. I am grateful to my parents. As their only child, they never asked me to stay near them.

In contrast, they always encourage me to go for my dream that does not follow the Chinese tradition. Thanks for allowing me to realize my potential. All the support they gave over the last thirty years was the greatest gift anyone has ever given me. I chose not to be an engineer and chose meteorology since meteorology is science, not technology.

When college graduation was coming up, everybody got a new choice: to go further with study or go to work. I tried to find a job at first, but there was not much opportunity for me due to the Hukou restriction (Hukou is a system of household registration in mainland China). Either the best offer I could get at that time was to work in Tibet where the subsidy is high, or at an island which is isolated during the typhoon season. Although these offers are not so dreamy, I was not worried at all: I already had a good score in the MSc enrolment test and was ready to interview in Beijing. Surprisingly, I failed in the interview. After realizing the outcome could not change, I made numerous calls to look for a new interview. I was lost both in the city and in my career. That was when I met Prof. Jun Wen, who was my promoter for the next four years at the Chinese Academy of Sciences, Lanzhou. I want to thank my Chinese side promoter Prof. Jun Wen not only for getting me back on track with the career but also to your virtue and eruditeness. Without your support, I would not have had the chance to study in the Netherlands and see such a colorful world. Without your support and

encouragement, the thesis would not have been finished. You are always generous to the mistakes I made.

The first time I met Prof. Bob Su was during a field campaign in Tibet in 2009. At that time, he fell ill due to altitude sickness while I was also left behind in a small county town because of catching a cold. I would never dream that one day the professor who I took care of would be my promoter. To me, Prof. Su was like a being from a galaxy far far away and doing some mysterious work beyond my imagination. Many thanks to the Chinese Scholarship Council, I got an interview opportunity for Ph.D. study in the Netherlands. In 2012, I got a chance to start my second Ph.D. career recommended by Prof. Bob Su. During the interview, Prof. Su said, "Oh, it's you!" I felt kindness, hospitality, and your humor and released my tension right away. That was a historical interview because CSC and KNAW (Koninklijke Nederlandse Akademie van Wetenschappen) stopped organizing such an interview from then on. This unique interview was also my first time to go abroad. Amusingly, I even refused to take travel photos because I wanted to seize this opportunity so much, not just take some pictures that I can recall. The application procedure after the interview was tedious and torturing, but finally, I made it with help from Prof. Bob Su and Prof. Jun Wen.

The study at ITC was never easy because we always challenged human's knowledge frontier. In the beginning, the motivation of this thesis was to use satellite remote sensing soil moisture products in the East Asia Summer Monsoon forecast. However, after going for a while, the research stopped due to the uncertainties in the satellite soil moisture products themselves. After discussing with Prof. Su and Dr. Zeng, we realized that the topic should go back to the passive microwave remote sensing issues considering our innovation on the soil effective temperature scheme. The long march started with our first paper that took 34 months until its publication. I was frustrated, disappointed and sometimes tortured but I could always get confidence, trust, and help from Prof. Su. Without his encouragement, suggestion and promotion, I cannot stand here and make my defense for sure. The first paper is just a short version of our collaboration and the same scene repeated time and time again for the last six years. Great thanks to my supervisor, Dr. Yijian Zeng whom I can always learn a lot from not only his successful supervision but also his integrity and carefulness. Whenever I have an idea or some crazy thoughts, you are my first audience

forever. Every word typed in the manuscript, every formula derived and every figure plotted in the draft contained your hard work and sweat. After creating the new soil effective temperature scheme, we found that the potential contribution might not be just an option in radiative forward modeling. Again, with encouragement from Prof. Su and Dr. Zeng, I turned my topic to the sensing depth and designed part of the experiment at Maqu Network. They gave me enough patience, time, as well as funding to do the research I thought was worthwhile. They fully supported me to achieve this dissertation.

From the dream of my parents to the final topic of this thesis, none of it follows the initial plan I had. Similarly, career or even life is almost like the weather/climate forecast. You can diagnose, model, or even predict it to some extent. However, you always have errors, and these errors increase fast due to nonlinear theory and can collapse my forecast quickly. We cannot predict someone's life just as we cannot be 100% certain of our weather/climate prediction until it happens. Most of all, both life and weather do not repeat. Non-repeatable is a critical feature of meteorological study because unlike physics or chemistry that could repeat under some conditions, real-world weather/climate events are unique. I would never know what my life would be if I went to the same university as my father did. I would never know where I would be if Prof. Jun Wen did not accept me. I would never know what I can achieve if I had not been at ITC. What I know is that I feel satisfied and confident after the Ph.D. study at ITC.

For another thing, I was struggling with the balance between being theoretical and practical during my whole Ph.D. All the work in this dissertation starts with a theoretical, integral and mathematically perfect solution for effective soil temperature that is called the Wilheit's scheme. It is so theoretical that it shares the same formula structure as the atmosphere radiative transfer does and in principle, they should be the same. However, Wilheit's scheme is not practical because it is hard to get delicate soil moisture profiles even in laboratories. Therefore, the studies of the last decades wanted to make it simple. To make it simple means to make it practical, like Choudhury's scheme that has only one fixed value for all the cases. Such a simplification does take out the complexity and minimize the inputs (otherwise, it will be an ill-posed problem), but it loses physics and adaptability. What did we lose in the simplification? Is there a

flexible way that could balance the theory and practice? To what extent, is a simplification acceptable, or tolerable? In other words, is theoretical research worthy of publishing? I want to thank all the anonymous reviewers and editors of my publications these past years. Without your patience and openness, the tedious mathematical derivation in this study would never turn into practical use in the future.

When I was doing this Ph.D., the above question was always an obstacle to my research. Sometimes, the result should be perfect as we inferred from the math, but it turns out to be terrible when you test it with observation. On the other hand, we question the non-physics empirical number and parameterization, but they do work out. There are dozens of equations we developed in this study and the reviewers question almost none of them when we were dealing with publication. Most of the negative comments focus on its practicality.

Also, I enjoyed friendship and discussions with Dr. Tiejun Wang who listened and encouraged me when I was lost. I wish to thank Dr. Xuelong Chen, Dr. Donghai Zheng, Dr. Ying Huang, Dr. Binbin Wang, Dr. Rogier van der Velde, Qiang Wang, Hong Zhao, Dr. Lianyu Yu. I learned a lot from your studies. I am glad to thank Lichun Wang, Chandra, Dr. Xiaolong Yu, Xu Yuan, Junping Du, Dr. Peiqi Yang, Chengliang Liu, and other Chinese friends at ITC for their friendly support. I thank Dr. Xin Wang who did wonderful field work and taught me how to cooperate with others. I want to thank Dr. Hui Tian, who is still supportive and forgiving my missing promise. Many thanks to Zuoliang Wang, Dongyu Jia, Jinlei Chen for their fieldwork on the ELBARA (a radiometer) and Maqu network establishment and maintenance. Many thanks to Anke, Tina, Lindy, Murat for their help with my study, and to ITC student affairs officer for helping me with my personal affairs.

My thanks to all the people I met during the years in Enschede. This thesis was supported by the CSC Talent & Training China – Netherlands program.

Contents

Abbreviations

AMSRe	the Advanced Microwave Scanning Radiometer-Earth Observing System
Cal/Val	Calibration/Validation
CCI	Climate Change Initiative
CMEM	Community Microwave Emission Modeling
COSMOS-UK	UK COsmic-ray Soil Moisture Observing System
ECMWF	European Centre for Medium-Range Weather Forecasts
ECV	Essential Climate Variables
ESA	the European Space Agency
ECOCLIMAP	The ECOCLIMAP programme is a dual database at 1 km resolution that includes an ecosystem classification and a coherent set of land surface parameters that are primarily mandatory in meteorological modeling (notably leaf area index and albedo)
GCM	General Circulation Model
HTESSEL	Hydrology Tiled ECMWF Scheme of Surface Exchanges over Land
ISMN	The International Soil Moisture Network
LAI	Leaf Area Index
L-MEB	the L-band Microwave Emission of the Biosphere
LPRM	Land Parameter Retrieval Model
MERRA-2	The Modern-Era Retrospective analysis for Research and Applications, Version 2 (MERRA-2)
NDVI	Normalized Difference Vegetation Index
RFI	Radio-frequency interference
NASA	National Aeronautics and Space Administration
SMAP	Soil Moisture Active Passive
SMOS	Soil Moisture and Ocean Salinity
SMMR	the Scanning Multichannel Microwave Radiometer
SNR	Signal-to-Noise Ratio

T_b	Brightness temperature
T_{eff}	soil effective temperature
ε	emissivity

Chapter

1 Introduction

1.1 Scientific background

The contribution of land surface conditions to the predictability of meteorological features is of interest to a wide community. The predictability at monthly to seasonal time scales is mainly attributed to anomalies of the sea surface temperature (SST), in particular, those related to El Nino events. However, Koster et al. [1] identified some key regions where soil moisture conditions may systematically affect precipitation variability in the boreal summer season, based on a model experiment involving multiple General Circulation Models (GCMs). The East Asia area is among sensitive regions regarding both soil moisture-precipitation and soil moisture-temperature interactions. In combination with a realistic initialization of soil moisture and a long enough memory in the soil water reservoir, increased predictability may be feasible in these regions [2]. Dirmeyer et al. [3] explored systematic soil moisture-precipitation interactions using a range of observations and (offline) land models across all seasons, roughly confirming the existence of areas where adequate soil moisture information could lead to improved forecasts at the monthly to the seasonal timescales. In general, these areas are found in transitional zones between dry and wet climates, where the coupling between soil moisture and evapotranspiration is expected to be strong and large enough to affect climate [4]. Several observational and modeling-based studies to a great extent agree on the location of these regions [5]. Douville [6] showed that soil moisture conditions in late spring played an important role in successfully modeling contrasting summers concerning precipitation and temperature in the Eurasian continent using a single GCM.

While seeing great potential for improvement in climate forecast skills by using land surface soil moisture with either analysis or assimilation, soil moisture has also been utilized in any regular or operational forecast systems. Soil moisture in land surface models could be updated via assimilating brightness temperature observations. Different to brightness temperature as the Level 1 instrument data, soil moisture is not a direct measurement and thus cannot be used for assimilation. One of the reasons is that the impact of soil moisture on the atmosphere above is extremely complex compared to the impact of other land surface variables like albedo, snow cover, skin temperature, etc. Soil moisture may lead to both positive feedbacks and negative feedbacks at the same time [5, 7-9]. On the one hand, wet soil decreases the land surface albedo, while it increases the short radiation absorbed by the land surface. The sum of latent heat and sensible heat increases with rising soil moisture, but while latent heat does increase along with soil moisture, sensible heat does not. Latent heat, or evaporation regarding water dynamics, increases the water content in the atmosphere, especially in its lowest layer. At the same time, evaporation also reduces the humidity gradient between the atmosphere and the soil surface, restraining the evaporation.

Water vapor either stabilizes the atmospheric layers by increasing atmospheric stability (via specific heat capacity) or provide the source for precipitation. If precipitation occurs, the soil will become wetter again. Thus a complete cycle is formed, with both negative and positive feedbacks in the soil moisture-evaporation-precipitation-soil moisture chain (Figure 1.1 left panel). On the other hand, soil moisture can affect the air temperature as well, because when soil moisture decreases, evaporation will also decrease, which in turn leads to higher air temperature. The higher air temperature accelerates evaporation, making the soil even dryer. This way another complete cycle is formed by soil moisture-evaporation-air temperature-soil moisture (Figure 1.1 right panel). In summary, the mechanism of soil moisture-climate feedback is very complicated and current research is restricted to local effects and case studies [1, 10-19]. No general conclusion has been drawn, whether soil moisture has a clear impact that might help improve forecast skills.

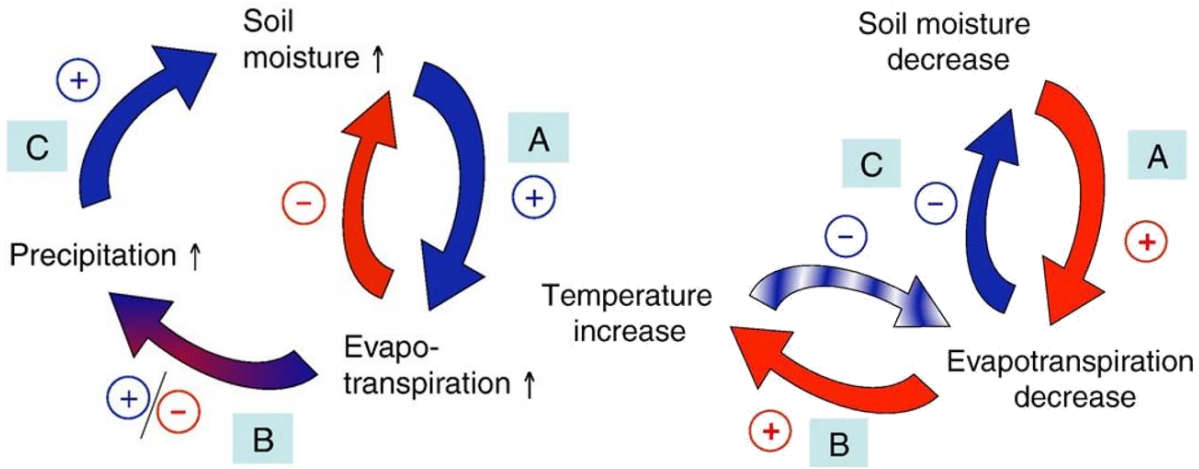

Figure 1.1 The complexity of soil moisture-precipitation/temperature feedbacks cited from Seneviratne et al. (2010).

This complexity hinders the application of soil moisture observation in weather/climate forecasts. Different to sea surface temperature (SST) which is considered as the most important factor in climate/weather forecast, soil moisture over land is not continuous either in spatial or temporal scales. Two soil moisture profiles tens of meters away from each other may be completely different due to topography, soil properties, vegetation, etc. Therefore, the determination of representativeness of *in-situ* soil moisture would always be difficult. Usually, to acquire soil moisture data comparable at model scale (e.g., tens of kilometers), the monitoring network would have to contain all terrain features and land surface cover types, dramatically increasing cost and labor intensity. In general, the current soil moisture networks may be categorized into three types, i.e., operational, auxiliary and special.

1) The operational soil moisture network is a long-term observation network, as financed institutionally. For example, the soil moisture network inherited from the Former Soviet Union's meteorology and agriculture operation system [20], as well as the stations set up by the China

Meteorological Administration [21]. These stations recorded soil moisture, as well soil temperature profiles, according to agricultural requirements, which means that the layers configured in the land surface (about 0-0.5 m) are coarse and may not represent the interaction between land and atmosphere.

2) The auxiliary network incorporates soil moisture networks built for other scientific research purposes, such as the Chinese Ecosystem Research Network [22] and the COSMOS-UK soil moisture network [23]. These networks were mainly set up by ecologists to monitor and estimate Gross Primary Productivity (GPP), drought, and flood, etc. These independent networks may thus adopt different standards and equipment in their set up.

3) The special network incorporates soil moisture networks used for satellite calibration/validation, such as the SMAP Cal/Val project [24], which partly overlapped and included the ISMN (the International Soil Moisture Network) [25]. Even before L-band satellites were in orbit, this kind of network existed for airborne radar/radiometer microwave remote sensing studies. Due to the large footprint of radar/radiometer measurements, these networks should consist of a cluster of *in-situ* soil moisture/temperature profile observations. These profiles are inter-comparable, and their entirety represents the soil moisture variation over a large area. However, although this last category would satisfy the scale requirements for climate models, it is still impossible to extend *in-situ* observations around the globe.

To achieve medium (3-10 days) or seasonal forecasts, a land surface model or ocean model usually needs to be coupled with a General Circulation Model (GCM). The feedback from the land surface model can be on greater time steps when coupled with the GCM, because land surface variables, such as soil moisture, vary much less than the atmosphere. On the other hand, the soil thermal and hydraulic conductivities and the surface energy balance are very sensitive to soil moisture changes. Hence, it is necessary to establish an appropriate data assimilation system of soil moisture to improve the soil moisture initialization at fine temporal scales [26]. Nevertheless, although the impact of soil moisture is relatively large among the land surface variables like LAI, snow cover and so on, it is always one order of magnitude smaller than SST, cloud cover, etc. [5, 27, 28]. Therefore, soil moisture is more a prognostic than a forecasting factor. It means soil moisture is produced by the GCM-LSM coupled system, but not the dominant driving force for medium or longer scale weather/climate systems [29]. The soil moisture fields contained in the model outputs such as ERA-interim and MERRA-2 (The Modern-Era Retrospective analysis for Research and Applications, Version 2) strongly depend on the land surface models [30-32].

Besides *in-situ* monitoring and the reanalysis of soil moisture products, another option is to obtain global soil moisture distribution from satellite remote sensing. Early in the 1970s, Skylab already carried out microwave remote sensing of the earth's surface, and the ensuing exploratory efforts led to the theory of remote sensing of soil moisture. In the 2000's, AMSR-E (the Advanced Microwave Scanning Radiometer-Earth Observing System), with its powerful passive-microwave radiometer, created the first operational global soil moisture map [33-35]. AMSR-E measures horizontally and vertically polarized brightness

temperatures at 6.9 GHz, 10.7 GHz, 18.7 GHz, 23.8 GHz, 36.5 GHz, and 89.0 GHz. The spatial resolution of the individual measurements varies from 54 km at 89 GHz to 56 km at 6.9 GHz. AMSR-E overpass times are around 1:30 a.m. (ascending) and 1:30 p.m. (descending) local time at the equator [36]. AMSR-E is not specifically designed for soil moisture detection and also provides measurements of precipitation rate, sea surface temperature, sea ice concentration, snow water equivalent, wind speed, atmospheric cloud water, and water vapor. The algorithms for AMSR-E soil moisture retrieval are different from precursors to those developed for L-band satellites such as SMOS and SMAP. AMSR-E uses a single-channel or dual-channel empirically to build a relationship between brightness temperature and soil moisture statistically [37]. Also, AMSR-E retrieves soil moisture from the emission model, i.e., LPRM (land parameter retrieval model) [38]. Soil moisture can only be detected to very shallow depth by AMSR-E, and the retrieved surface soil moisture is strongly affected by vegetation cover, as well as by evaporation and precipitation. To overcome these influences, L-band microwave remote sensing is imperative.

SMOS is the first L-band satellite particularly designed for soil moisture detection using an interferometric approach [39, 40]. The satellite was launched in November 2009 and has provided continuous soil moisture data since then. SMOS monitors surface soil moisture with an accuracy of 0.04 m^3/m^3 (at 35–50 km spatial resolution) with repeat visits every three days at least for the middle and low latitude. More details on SMOS will be presented in the chapters containing the data. The next L-band satellite launched was Aquarius, although it was not specially designed for soil moisture detection [41]. Aquarius was a NASA instrument aboard the Argentine SAC-D spacecraft. Its mission was to measure global sea surface salinity to predict future climate conditions better. As is well known, the radiometer mounted on Aquarius, as well as SMOS/SMAP, does not distinguish between land surface and ocean surface. While soil moisture is the dominant factor controlling radiometry over land, sea surface salinity controls the signal over the ocean. So technically, the brightness temperature monitored by Aquarius could also be used to retrieve soil moisture over land. However, little research exists on soil moisture retrieval from Aquarius, mainly because its resolution is quite low (100 km) [42]. SMAP is another L-band microwave satellite [43, 44]. Different to SMOS, SMAP uses a real aperture antenna (incidence angle fixed at 40°) that combines passive and active microwave remote sensing techniques. The real aperture antenna guarantees that its spatial resolution reaches 36 km for passive and 3 km for active techniques. A real aperture antenna is also an advantage when dealing with RFI (Radio-frequency interference). SMAP can pick up spots and moments of strong RFI and then simply remove the unexpected data. In general, the passive soil moisture product is more precise, but the resolution is low compared to the active one. However, a 36 km resolution is good enough for most GCMs, and there is no evidence that 3 km or the active-passive merged 9 km soil moisture products are superior to the passive one [45].

In-situ measurement, reanalysis, and satellite remote sensing are three methodologies to obtain soil moisture, each with their advantages and disadvantages. In an attempt to take advantage of the different methodologies, all three could be merged to develop a soil moisture dataset, as in the ESA-CCI-Soil Moisture project (The European Space Agency-Climate Change Initiative) [46]. The latest version of ESA

CCI SM v04.2 comprises the three well-known active, passive and combined satellite soil moisture datasets. This latest release provides global soil moisture data until 31-12-2016. It merges all active and passive L2 products directly to generate a combined product (previously, this was created from the active and passive products). Also, soil moisture uncertainties are now available globally for all sensors except for SMMR (the Scanning Multichannel Microwave Radiometer) and spatial gaps in the triple collocation-based SNR (Signal-to-Noise Ratio) estimates are now filled using polynomial SNR-VOD regression. These techniques show that the merged data are not real soil moisture observations but more an objective analysis with interpolation, nudging, and even a simple model with water/energy restrictions [47]. This kind of soil moisture data set is useful, but in merging different data sources new errors are generated, either through the mathematical algorithms or from input data that may be incompatible. In principle, this kind of data should not be used in data assimilation to improve the weather forecasting skill as they are not real observations.

In summary, passive remote sensing of soil moisture has good potential to improve weather forecasting via data assimilation in theory [48]. The endeavor to assimilate soil moisture or L-band satellite brightness temperature has been ongoing. Patricia de Rosnay et al. (2013) developed a new land surface analysis system based on a simplified point-wise Extended Kalman Filter (EKF), which was implemented at ECMWF in the global operational Integrated Forecasting System (IFS) in November 2010 [49, 50]. However, the assimilation of passive soil moisture products, especially SMOS and SMAP, has a mitigated impact[51].

First of all, the expected precision regarding soil moisture products designed by SMOS and SMAP is 0.04 m^3/m^3, but this accuracy cannot be attained at a local scale [52, 53]. For example, in each SMOS overpass (i.e., per day, per grid point) we compute the RMSE between SMOS TB (~15 incidence angles) versus the modeled one (~15 incidence angles) over the Tibetan Plateau via personal communications with Dr. Yan Kerr's team. The RMSE over the Tibet Plateau is less than 20 K, but this region is filtered out by the current SMOS version due to suspected RFI. The region nearby has more severe RFI pollution, coinciding with the population distribution. The RMSE, which reflects the difference between brightness temperature and model forward simulation, reveals the missing part we have not been able to fully explain so far. While doing data assimilation, this bias and RMSE will lead to instability rather than improvement in the model. Because soil moisture deduced from T_b, the difference in T_b will also propagate into soil moisture.

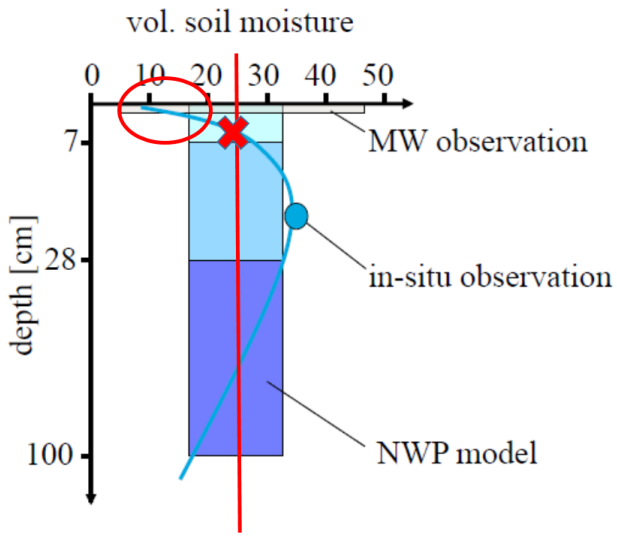

Figure 1.2 An illustration of mismatched soil moisture definition in satellites remote sensing (MW observation, the rectangle between 0-2 cm), field measurement (or *in-situ* observation, the blue point) and models (NWP model, the columns). The blue profile gives an example of a soil moisture profile. The red line and red cross indicate the definition used in this thesis as the average moisture and form the sensing depth with a real soil moisture profile. The red circle shows where the satellites are measuring with the example profile, which gives a mismatch to the blue point.

Secondly, SMOS and SMAP directly measure T_b, the emission, but not soil moisture. Instead of assimilating soil moisture, it is more rational to assimilate T_b [54-56]. With forward models and assimilation tools like the Kalman Filter, it is possible to update soil moisture/temperature profiles while accounting for an observation error matrix [57]. Thirdly, if soil moisture is assimilated in models, a clear definition is necessary regarding where the satellites are measuring, as can be seen in Figure 1.2 [48, 58, 59]. Models, *in-situ* observations, and satellite remote sensing each have their definitions of soil moisture depth, which is often not interchangeable. For example, in models, the soil moisture is usually defined at grid level, and the soil moisture within these nodes is considered uniform. *In-situ* observations measure at specific depths. Satellite remote sensing also has its definition but in principle, each dielectric profile has its unique emission behavior, and this profile constantly varies, even at one fixed point, as will be explained in Section 1.2.

1.2 Problem statement

A detailed description of the microwave transfer process is critical to quantify the energy emitted from the soil, vegetation and the attenuation across different media like the soil-atmosphere surface, soil layers, etc. For shorter wavelengths, soil moisture monitored by a radiometer refers to only the top few centimeters of the soil. To the L-band, the signal can even be detected from meters deep in extreme cases (e.g., over desert or permafrost). In general, the penetration depth is defined as the depth where the residual of the radiation is reduced to a 1/e range, though this heavily depends on the dielectric profile. Based on a complicated description of the microwave transfer process in the soil column, the interface of different

media (e.g. soil-atmosphere), the vegetation and the atmosphere, application of L-band satellites such as SMOS and SMAP make it possible to acquire a higher accuracy in measuring soil moisture than with all other bands [60, 61].

As stated in Section 1.1, one problem of L-band microwave remote sensing is to know which layer the satellite is observing, i.e., what depth exactly corresponds to the remotely sensed soil moisture product. There are two concepts, which can be defined as follows,

1) Soil Temperature Sensing Depth: where the temperature weighting function for a given dielectric profile reduces to 1/e (about 0.36) ;
2) Soil Moisture Sensing Depth: At L-band, the temperature sensing depth could easily reach 20 to 40 cm. Does that mean L-band can detect soil moisture below 20-40 cm? Theoretically, any change in the dielectric profile will cause a change in the brightness temperature T_b , and everything depends on how precise the sensor is. In practice, however, if the change in T_b is less than a few *Kelvin*, it will be very difficult to separate this change from changes resulting from other factors, such as surface roughness and temperature profile variations. The sensor would not capture the soil moisture change at the few centimeters lower down because the surface layers dominate the emission signal. Therefore, Ulaby (1986) defined the moisture sensing depth as the most sensitive layer to correspond with T_b [62].

Although the microwave emission/sensing depth is very important for improving the passive microwave retrieval accuracy of land surface parameters, forward simulation and soil moisture assimilation, quantified microwave emission/sensing depth models were few [63]. The emission/sensing depth has long been a neglected variable that was simplified to soil moisture from the first layers. While considering the error caused by roughness, vegetation, etc., which might be 10-20 K for T_b , the soil moisture gradient at the surface is ignored. However, the soil moisture gradient could be very steep especially after rainfall and is responsible for the different probability distributions between SMAP/SMOS and field observations [64].

Escorihuela et al. (2010) [65] used a typical explanation of moisture sensing depth as defined by "moisture sensing depth" above. The layer is defined as a fixed soil moisture layer if it has the highest correlation coefficient with T_b . Since the surface layer contributes most to emission, the upper few centimeters are expected to form the sensitive layer. This paper is a case study, but it tries to extend the sensitive layer to emissivity computation in forward modelling. A definition of sensitive layer means that the soil moisture at the sensitive layers should be used to compute emissivity in models. This conclusion could be questioned, as the dielectric profile changes all the time and a fixed layer can never be the most sensitive layer for all conditions. Besides, there is a difference between a sensitive layer (the rectangle in Figure 1.2) and an equivalent layer (the cross in Figure 1.2). Soil moisture used for calculating emissivity should represent the emission of the whole soil column because SMOS and SMAP have only one channel.

Otherwise, one brightness temperature observation would corresponds a range of soil moisture values due to the complexity of soil moisture/temperature profile. Liu et al. [66] identify circumstances where current models fail to relate near-surface soil moisture to an observed T_b at L-band reliably. It is deemed inappropriate that current microwave algorithms use just a single depth-fixed soil moisture value to represent the effective moisture at moisture sensing depth [66]. Such a simplification will result in unrealistic T_b estimates for the bare and vegetated soil at L-band, particularly during extreme hydrologic conditions, and leads to the recommendation to adopt an exponentially decaying weighting function. It reveals that as an approximation of a coherent model, the incoherent model has its shortfalls. In this case, incoherent models may not be appropriate for longer wavelengths such as the L-band [66].

Zhou et al. [63] claimed that with the magnitude of radiation, the attenuation by the soil might be tiny and not sensed by the microwave radiometer (i.e., be less than the sensitivity of the radiometer). Whether the emission is sensed by the radiometer or not, is determined by both the magnitude of the radiation and the sensitivity of the radiometer. Only the emission of a soil layer that can be distinguished by the radiometer forms a real target, and the greatest vertical distance below the surface of the real target is the so-called effective emission depth. It states that, although there is still 1/e energy coming from below the penetration depth, the soil temperature and moisture changes there would not be detected by the radiometer [63]. Without a clear definition of sensing depth, especially moisture sensing depth, it is impossible to build up a quantified relationship between T_b and soil moisture (i.e., to which depth the satellite is measuring). The unclear definition of sensing depth can cause a series of issues regarding the understanding and application of the SMOS/SMAP soil moisture products.

It is well accepted that *in-situ* soil moisture monitoring for validation and calibration of the L-band is set up at 5 cm, ignoring temporal and spatial heterogeneity. On the other hand, it is nearly impossible to mount delicate and continuous soil moisture sensors in a network, representing the most sensitive dominant emission layer of the area (e.g., 2 cm as identified by Escorihuela et al. 2010). The sensors have to be installed at a certain distance to avoid electrical signal interference. Besides, it is hard to maintain a sensor at the surface top layer (0-2 cm), where the soil moisture gradient is usually sharp, as the soil surface may be easily disturbed by wind, grazing, rainfall, etc. In this case, 5 cm is a good option to keep the sensor safe and consistently providing data. Furthermore, statistical tools overemphasize correlation instead of physical process. For example, unRMSE (unbiased Root Mean Square Error) replaces RMSE (Root Mean Square Error) to prove that the satellite's soil moisture products are meaningful [24, 67-69]. The difference between unRMSE and RMSE is that the former removes bias and focuses on the variation between T_b (or satellite soil moisture product) and ground soil moisture.

There is little research on moisture/temperature sensing depths, and the following issues have remained unsolved: 1) In forward simulations, emissivity is simplified as the emissivity of the first layer; 2) in ground calibration/validation, soil moisture measured at a fixed level is used, which does not match

the dynamic changes of dielectric profiles; and 3) the assimilation of satellite soil moisture products lacks a theory to support further development (e.g., which depth for assimilation).

To address the above issues, within the framework of current incoherent microwave transfer models (e.g. based on the Fresnel reflectivity model), it is necessary to find a new formula for T_{eff} as it is the only variable that describes the microwave energy flux within the soil column (further details in Chapter 5 & 6) and implicitly contains depth information. Although there is an analytical solution for Wilheit's scheme for calculating T_{eff}, its input requirement is demanding, and it does not fit the field observation or land surface model outputs where the vertical sampling is sparse (see Chapter 2). Furthermore, all existing T_{eff} schemes are simplified into two layers and contain empirical parameters, and cannot give a detailed description of the dielectric profile. In other words, depth information cannot be found in the current soil moisture retrieval models. The following research questions are therefore put forward:

1) Is there a better way to compute T_{eff} with flexible layer configurations?
2) How does T_{eff} affect the retrieval result?
3) Is it possible to determine the depth at which L-band satellites are observing?

1.3 Objectives

To find an answer to these research questions, this Ph.D. project aims to:

1) Develop a new T_{eff} scheme that contains no empirical parameters and accommodates different kinds of dielectric profiles. In principle, the new scheme should be flexible regarding multi-layer configuration and meanwhile approaching to Wilheit's scheme;
2) Analyze the new T_{eff} scheme and its physical implications. Apply this to determine how to evaluate and set up a soil moisture network in which precise estimation of T_{eff} is possible;
3) Evaluate the T_{eff} scheme with the current SMAP or SMOS observations and compare it with other existing T_{eff} schemes. Quantify the impact of adopting the new T_{eff} scheme;
4) Retrieve the sensing depth of passive microwave remote sensing of soil moisture and quantify at which layer the soil temperature value would match T_{eff}.

1.4 Passive microwave remote sensing of soil moisture

Table 1.1 The frame for a passive microwave transfer model. The brackets form a possible option in current CMEM.

ATMOSPHERE	**Atmospheric radiative transfer model**
	(None/Pellarin/Liebe/Ulaby)
VEGETATION	**Vegetation opacity model**
	(None/Kridyashev/Wegmuller/Wigneron)
SOIL	**Smooth surface emissivity model**
	(Fresnel/Wilheit)
	Soil roughness model
	(None=Smooth/Choudhury/Wegmuller/Wigeron)
	Soil dielectric mixing model
	(Wang & Schmugge/Dobson/Mironov)
	Effective temperature model
	(Choudhury/Wigneron/Holmes)

The framework for passive microwave remote sensing of soil moisture (e.g., Community Microwave Emission Modelling platform, CMEM) is introduced in this section. It contains three parts: soil, vegetation, and atmosphere (Table 1.1). In contrast to former microwave satellite radiometers such as AMSR-E, L-band can penetrate the atmosphere, even the clouds. Usually, the attenuation through the atmosphere can be ignored so this will not be discussed in detail here. The main part of the following section is cited from the CMEMv5.1 handbook, which is a concise summary of passive microwave remote sensing of soil moisture [70]. CMEM contains a full physical description of the forward microwave transfer model and is written in Fortran [71, 72]. Apart from citing the CMEM handbook, we have added comments to each paragraph. It should be noted that the CMEM, as other microwave transfer models, is supposed to include state-of-the-art microwave models at L-band.

1.4.1 Radiative transfer equations

Single channel L-band soil moisture retrieval algorithms are based on a simplified solution of the radiative transfer equations as other bands. Its structure is similar to sandwiches that consists of several layers. The layer below emits radiation, and is attenuated by the layers above it. The attenuation capacity in each layer may relates to different factors, and is described by optical depth in general. For polarization p, the brightness temperature over snow-free areas at the top of the atmosphere $T_{Btoa.p}$ can be expressed as

$$T_{Btoa.p} = T_{Bau.p} + e^{-\tau_{atm.p}} \cdot T_{Btov.p} \tag{1.1}$$

and

$$T_{Btov.p} = T_{Bsoil.p} \cdot e^{-\tau_{veg.p}} + T_{Bveg.p}\left(1 + r_{r.p} e^{-\tau_{veg.p}}\right) + T_{Bad.p} \cdot r_{r.p} e^{-2\tau_{veg.p}} \quad (1.2)$$

where $T_{Bau.p}$ (K) is the up-welling atmospheric emission and $\tau_{atm.p}$ is the atmospheric optical depth. Usually, $\tau_{atm.p}$ approximate to 0 at L-band. $T_{Btov.p}$ (K) is the top of vegetation brightness temperature (when the vegetation is represented as a single-scattering layer above a rough surface). $T_{Bsoil.p}$ (K), $T_{Bveg.p}$ (K) and $T_{Bad.p}$ (K) represent soil, vegetation layer, and downward atmospheric contributions, respectively. $r_{r.p}$ is the soil reflectivity of the rough surface (one minus the emissivity $e_{r.p}$) and $\tau_{veg.p}$ is the vegetation optical depth along the viewing pathway (nadir path/cos(incidence angle)). From Equation (1.2), soil moisture, vegetation, and atmospheric terms are described as a combination of physical temperature and exponential decay coefficients. Lv's T_{eff} scheme, which will be introduced in Chapter 2, has a similar form to Equation (1.2) regarding physical temperature and exponential decay coefficient combination. Hence, Lv's T_{eff} scheme is not only an algorithm to compute soil effective temperature but also a complement to the L-band microwave transfer theory. With Lv's T_{eff} scheme, the soil optical depth (τ_{soil}) goes through all components. The concept of soil optical depth will be discussed in Chapter 5 and 6 in detail. The contribution emitted from the soil can be written as the product of the soil emissivity $e_{r.p}$ and the effective temperature:

$$T_{Bsoil.p} = T_{eff} \cdot e_{r.p} \quad (1.3)$$

Equation (1.3) is the zeroth-order incoherent model because the emissivity $e_{r.p}$ refers to a layer model and all the profile information is condensed in T_{eff} . The zeroth-order incoherent model is popular and applied for SMOS and SMAP retrievals. The T_b from SMOS/SMAP can only correspond to one soil moisture. Coherent models, which reads

$$T_{Bsoil.p} = \int_0^{\infty} \alpha(x) T(x) \exp\left(-\int_0^{x} \alpha(x) dx'\right) dx \quad (1.4)$$

where x is gemetric soil depth, T(x) is soil temperature at x, and $\alpha(x)$ is express as $\alpha(x) = \frac{2\pi}{\lambda} \frac{\varepsilon''}{\sqrt{\varepsilon'}}$. Equation (1.4) is much more complex. Equation (1.4) has the depth information but only for classical retrievals. In brief, the coherent model takes account of the emissivity at each soil layer, so does not need T_{eff} . They require detailed soil moisture profiles in the forward simulation. The differences between incoherent and coherent models are tiny for shorter wavelengths but become large for longer wavelengths like L-band.

Soil emissivity models (coherent and incoherent ones) employ the relationship between soil emissivity and soil dielectric constant. For a smooth surface, the Fresnel equation is commonly used in microwave emission models to compute the air-soil interface reflectivity (incoherent model). Wilheit's coherent model is physically based and accounts for both coherent and incoherent components of the signal [73]. It represents the soil as a stratified medium where the vertical profiles of the soil dielectric constant and temperature are used to compute the resulting air-soil interface emission.

1.4.2 Vegetation

Microwave attenuation in both vegetation and soil are dominated by liquid water, i.e., VWC (vegetation water content). However, VWC is not measurable even in a laboratory because it is impossible to completely separate water existing in root, stem or leaf, and may consist of free as well as bound water. The structure of vegetation species affects the distribution of VWC. In practice, microwave remote sensing of soil moisture requires several approaches to include VWC from a few different parameters and variables such as NDVI or Leaf Area Index (LAI). Vegetation is usually represented by so-called τ−ω approaches:

$$T_{Bveg.p} = T_c \cdot \left(1-\omega_p\right) \cdot \left(1-e^{-\tau_{veg.p}}\right) \tag{1.5}$$

where T_c is the canopy temperature and ω_p is the single scattering albedo at polarization p. Jackson and Schmugge proposed a simple parameterization for vegetation optical thickness [74]:

$$\tau_{veg.p} = b \cdot \frac{VWC}{\cos\psi} \tag{1.6}$$

where b and VWC are the vegetation structure parameter and the vegetation water content, respectively, and ψ is the incidence angle. For high vegetation types such as rainforest, deciduous forest, and coniferous forest VWC is set to 6 kg/m^2, 4kg/m^2, and 3kg/m^2, respectively, following Pellarin [75]. For low vegetation types like grass and crops, VWC is described as a function of LAI:

$$VWC = 0.5 \cdot LAI \tag{1.7}$$

Default values for b are 0.2 for grass, 0.15 for crops, and 0.33 for forests. The single scattering albedo is constant at ω = 0.05 for low vegetation types (grass and crops) and ω = 0.15 for high vegetation types (forests).

The Wigneron et al. [76] vegetation optical thickness model differs from Equation (1.7), with the single scattering albedo depending on vegetation types and polarizations. The polarized optical thickness is expressed as:

$$\tau_{veg.p} = \tau_{nadir}\left(\cos^2\psi + tt_p \sin^2\psi\right)\frac{1}{\cos\psi} \tag{1.8}$$

$$\tau_{nadir} = b' \cdot LAI + b'' \tag{1.9}$$

where the parameters tt_p represent the angular effect on vegetation optical thickness for each polarization and vegetation type. τ_{nadir} is the nadir optical depth, b' and b'' are the vegetation structure parameters.

Kirdyashev's [77] parameterization expresses the vegetation optical thickness as a function of the wave number k (between 1 GHz and 7.5GHz), the dielectric constant of saline water, ε''_{sw}, VWC, incidence angle ψ, water density ρ_{water}, and a vegetation structure parameter a_{geo}:

$$\tau_{veg.p} = a_{geo} \cdot k \cdot \frac{VWC}{\rho_{water}} \cdot \varepsilon''_{sw} \cdot \frac{1}{\cos\psi} \tag{1.10}$$

This parameterization was extended to a larger range of frequencies (1-100 GHz) by Wegmuller et al. (1995) [78].

In above, all the schemes are trying to build a relationship between VWC and $\tau_{veg.p}$, and these schemes are empirical mostly. Although L-band has a stronger penetrating capacity compared to X/C band, but vegetation, especially forest is unneglectable. For most forests covered landscape, the brightness temperature singal is not dominate by soil moisture. Thus, no soil moisture can be retrieved. For low vegetation covered landscape, brightness temperature also depends on the vegetation structure. For instance, to simulate wheat is easier than cabbages because the later one has complex leaf structure.

1.4.3 Surface roughness

Rough surfaces are characterized by higher emissivity and less difference between horizontally and vertically polarized brightness temperatures. The role of roughness is like increasing the soil surface area. Wang and Choudhury (1981) [79] proposed a semi-empirical approach to represent soil roughness effects on the microwave emission. The rough reflection is computed as a function of the smooth reflection and three parameters Q, h, N:

$$r_{r.p} = (Q \cdot r_{s.q} + (1-Q) \cdot r_{s.p}) \cdot e^{-h \cdot \cos^N \psi} \tag{1.11}$$

where p and q refer to the polarization states, Q is the polarization mixing factor, N describes the angular dependence, h is the roughness parameter, and ψ the incidence angle. The mixing factor Q is considered to be very low at low frequencies and is generally set to 0 [38, 76]. h is measured as the root-mean-square of land surface. Based on Equation (1.11) two parameterizations have been proposed with $N = 0$ for:

$$h = (2k\sigma)^2 \tag{1.12}$$

$$h = 1.3972 \cdot (\frac{\sigma_s}{L_c})^{0.5879} \tag{1.13}$$

where k is the wave number, and L_c and $\sigma\,(or\ \sigma_s)$ are correlation length and standard deviation of surface roughness, respectively. The slope parameter $m = \frac{s}{L_c}$ is used as a calibration parameter in Equation (1.13) [80]. The global scale study conducted by Pellarin [75] used Wigneron's [80] parameterization, with a constant value of L_c = 6.0 cm, and σ = 0.44 cm, leading to h = 0.3. However, a more recent soil roughness parameterization has been developed and validated against field experiments. It is based on Equation (1.11) and accounts for the dependency of the roughness parameter on soil moisture and soil texture [81].

Also, the roughness parameter can be computed as a function of both soil moisture and vegetation type with N depending on vegetation and polarization. Wigneron et al. (2007) and Wegmuller et al. (1999) [76, 82] proposed a different approach based on smooth horizontal emissivity with a single roughness parameter $h = k \cdot \sigma$.

1.4.4 Dielectric constant model

Microwave remote sensing of soil moisture relies on the large contrast between the dielectric constant of water (~80) and that of dry soil (~4) at L-band. The soil dielectric mixing model computes the soil dielectric constant ε as a function of volumetric soil moisture (θ), soil texture, the frequency of detection and surface soil temperature T_{surf} . It is an essential part of forward modelling, and retrieval approaches. The emissivity ranges from about 0.5 for extremely dry soil to almost 0.95 when the water content exceeds 0.6 cm^3/cm^3, and depending on soil textures. Three semi-empirical dielectric models are available in CMEM: Mironov et al. (2004)[83], Dobson et al. (1985)[84] and Wang & Schmugge (1980)[85]. The Wang and Schmugge model and the Mironov model consider the effect of bound water on the dielectric constant but are limited to rather low frequencies of 1-5 GHz and 1-10 GHz, respectively. The Dobson model is valid for a larger range of frequencies (1-18 GHz), but the dielectric constants computed from the Wang & Schmugge (1980) and the Mironov et al. (2004) models are in better agreement with measurements for a large range of soil texture types [83]. SMOS retrievals use Mironov's model operationally. The dielectric computation in this thesis uses Mironov's model unless otherwise specified.

1.4.5 Soil Effective Temperature

A simple parameterization of the effective temperature was first proposed by Choudhury et al. (1982)[86]:

$$T_{eff} = T_{deep} - (T_{deep} - T_{surf}) \cdot C \tag{1.14}$$

with T_{deep} for soil temperature at depth (at ~ 50 cm) and T_{surf} for surface soil temperature (at ~ 5 cm) and C an empirical parameter that depends on frequencies. This parameterization was modified by Wigneron for L-band radiometry including a dependency of C on soil moisture [80], with the coefficients b and w_0 as $C(\theta) = (\theta / w_0)^b$. Holmes proposed a more complex parameterization where C is expressed as a function of the dielectric constant [87]. Based on the long-term SMOSREX data set, de Rosnay provides an inter-comparison of these three parameterizations [88]. Lv's scheme is a new scheme developed by Lv et al. (2014). It has been successfully implemented in the CMEM beta version (the version we made based on CMEMv5.1). Lv's scheme is not a simple parameterization of the Choudhury scheme, but a discrete method with its scope not just limited to a T_{eff} calculation, but also providing an evaluation of the $T_b - T_{eff} - \tau - depth$ relationship in which the soil depth is preserved in T_{eff}. The $T_b - T_{eff} - \tau - depth$ relationship will be explained in this thesis.

Besides Section 1.4.1-1.4.5, there are other components like snow cover, ice dielectric constant, and open-water fraction that may affect brightness temperature simulation. These cases exceed the scope of our aim and will not be discussed. CMEM is introduced in this section as a background knowledge about passive microwave remote sensing of soil moisture algorism. The improvements about soil effective temperature and tau-z model are applied in a testing version of CMEMv 5.1 in Matlab.

1.5 Structure of the Thesis

Chapter 1 (this chapter) introduces the background to this research, the scientific questions posed, and the specific objectives of the study. A mathematical derivation of the new soil effective temperature scheme (i.e., Lv's scheme) and its comparisons against other T_{eff} schemes is presented in Chapter 2. Chapter 3 further describes the physical basis of Lv's scheme and discusses a cut-off residual for evaluating T_{eff} and the relationship between the parameter B (i.e., equivalent to the soil optical depth as in Lv's scheme) and soil depth. The investigation of the *B* - soil depth relationship was enabled due to the flexible discretization nature of Lv's scheme. Chapter 2 bridges the gap between existing two-layer T_{eff} schemes and the integral one (i.e., the Wilheit scheme). Most of the studies consider T_{eff} as a second-order parameter in incoherent microwave transfer theory. As such, the importance of T_{eff} for the depth at which the satellites are observing was ignored. Chapter 3 discusses the role of T_{eff} in the microwave transfer and suggests the application of Lv's scheme to determine the optimal mounting depth of *in-situ* soil moisture sensors for calculating the effective temperature from the L-band. Chapter 4 gives insights into the influence of different T_{eff} schemes for L-band satellite missions such as SMOS and SMAP. It is the first global evaluation of the impact of T_{eff} on current soil moisture retrievals based on land surface model inputs (MERRA-land here). Chapter 5 focuses on the mathematical derivation that proves T_{eff} is equal to

the soil temperature measured at the penetration depth with a linear assumption. It builds upon a relationship between soil optical depth and soil depth via Lv's scheme. Chapter 6 extends the linear assumption to more general cases and develops a one-parameter formula to describe the relationships with observations. Chapter 7 summarizes this Ph.D. study and presents an outlook for the future.

Chapter

2 An Improved Two-layer Algorithm for Estimating Effective Soil Temperature in Microwave Radiometry using In Situ Temperature and Soil Moisture Measurements[1]

Abstract: The effective soil temperature (T_{eff}) is essential for the retrieval of soil moisture information when satellite microwave remote sensing data are used. In this investigation, a new two-layer scheme (Lv's scheme) is developed to estimate T_{eff} considering wavelength, soil moisture, sampling depth, and soil temperature. The accuracy of the estimated T_{eff} is verified with data collected in a field experiment at the Maqu Climate and Environment Observatory in the source region of the Yellow River. In addition to clearly defining the physical meaning of Lv's scheme, this chapter explains the physical meaning of Choudhury's C parameter, which is empirically determined by a least-square method. It was found that Lv's scheme does not require fitting parameters. Further, Lv's scheme can be used to estimate T_{eff} based on soil moisture data at the surface or any other specified soil depth, thus creating the opportunity to use observations and modeled data from different depths.

Keywords: Soil moisture, effective soil temperature, passive microwave remote sensing

[1] This chapter is based on

Shaoning Lv, Jun Wen, Yijian Zeng, Hui Tian, Zhongbo Su. 2014. An Improved Two-layer Algorithm for Estimating Effective Soil Temperature in Microwave Radiometry using In Situ Temperature and Soil Moisture Measurements. Remote Sensing of Environment, DOI: 10.1016/j.rse.2014.07.007

2.1 Introduction

Soil moisture is a key variable in hydrology, agriculture, as well as weather and climate forecasts because of its large heat capacity and rapid response to precipitation and irrigation [89, 90]. *In-situ* measurements of soil moisture profiles are not always available due to high costs and complicated maintenance. It is therefore impossible to use ground networks to provide global coverage for soil moisture. As a result, remote sensing and model simulation are employed for obtaining continuous global soil moisture products. In past decades, various techniques, models, and algorithms have been developed to estimate surface soil moisture using satellite remote sensing [40, 76, 91-94]. The principle of detecting soil moisture using passive microwave remote sensing is based on the difference in dielectric properties between free water and dry soil and is considered to be the only effective technique for acquiring global soil moisture distributions [95, 96]. With the new satellites launched, microwave sensors play an increasing role in mapping global soil moisture distribution. Examples are the Soil Moisture and Ocean Salinity (SMOS) mission launched in 2009 and the Soil Moisture Active Passive (SMAP) to be launched in 2014 [40, 43].

Passive microwave remote sensing only offers a few bands appropriate for soil moisture retrieval. One of the key factors in passive microwave soil moisture retrieval is the sampling depth. Although the L-band (central wavelength at 21 cm) is most suitable for estimating soil moisture [97-99], its sampling depth may vary from centimeters to even meters beneath the soil surface. The sampling depth will vary depending on soil moisture, texture, as well as soil temperature. However, to calculate the soil emissivity (e) accurately, which is another key factor for soil moisture retrieval, it is necessary to determine the effective soil temperature T_{eff} accurately [40, 100].

T_{eff} can be computed accurately for plane stratified dielectric layers [73, 85, 96, 101-103]. However, plane stratified dielectric layers cannot describe situations in the field, where the soil is neither homogeneous in any dimension. Based on its original form in Wilheit (1978) [73], a simplified two-layer scheme with just one parameter [86] is often used in microwave remote sensing for soil moisture retrieval [38, 104-107]. The scheme was subsequently improved by considering both wavelength and surface soil moisture [80, 87, 88, 108, 109]. The resulting algorithms have also been applied to provide accurate T_{eff} in other research [38, 76, 110, 111]. Nevertheless, the existing schemes require parameter calibration for Holmes' scheme or soil texture for Wigneron's scheme and have relatively stringent requirements regarding field observation depth (e.g., at both the surface and a specified depth). More information about these models may be found in the T_{eff} models inter-comparison study by [112].

In this paper, after analyzing Choudhury's scheme, a new two-layer scheme (Lv's scheme hereinafter) was developed (Section 2.2). After explaining the physical meaning of each variable in Lv's scheme, Section

2.3 demonstrates how wavelength, soil moisture, sampling depth, and soil temperature can affect the calculation of T_{eff} . Comparisons with Wigneron's scheme [109] and Holmes' scheme (Holmes et al. 2006) are presented. In Section 2.4, a numerical scheme is presented and theoretically formulated, and evaluated based on the *in-situ* observations and its limitations discussed. Conclusions are drawn in Section 2.5.

2.2 Method and Materials

2.2.1 Derivation of the Two-Layer (Lv's) Scheme

A satellite microwave radiometer measures the intensity of microwave radiation emitted from the earth's surface and below. From its emission at any point in the soil to the soil surface, the radiation is attenuated by the intervening soil, whose absorption depends heavily on soil water content via the imaginary part of the dielectric constant. The radiation intensity beneath the soil surface is, therefore, a superposition of intensities emitted at a different depth within the soil layers [73]. In the absence of vegetation and atmospheric influences, the observed microwave intensity formulated as brightness temperature T_B can be formulated as a product of emissivity (e) and T_{eff} :

$$T_B = eT_{eff} \tag{2.1}$$

with T_{eff} expressed follow [98, 113]:

$$T_{eff} = \int_0^\infty T(x)\alpha(x)\exp\left[-\int_0^x \alpha(x')dx'\right]dx \tag{2.2}$$

where x is the vertical distance (depth) from the surface to the soil layer concerned. $T(x)$ is the physical temperature at depth x and $\alpha(x)$ is an attenuation coefficient which depends on the dielectric constant ε and wavelength λ . The detailed form of $\alpha(x)$ is given by [73]:

$$\alpha(x) = \frac{4\pi}{\lambda}\varepsilon''(x)\Big/ 2\left[\varepsilon'(x)\right]^{\frac{1}{2}} \tag{2.3}$$

T_{eff} may be calculated by using Equation (2.2) with measured and interpolated soil moisture and temperature profiles. Choudhury et al. (1982) developed a simple two-layer algorithm with one parameter to calculate T_{eff} , based on the microwave radiative transfer Equation (2.2) in a plane stratified dielectric layer, assuming a linear soil temperature profile is expressed as [86]:

$$T(x) = T_\infty + (T_1 - T_\infty) f(x) \tag{2.4}$$

where T_1 and T_∞ are the surface and deep soil temperatures, respectively, and $f(x)$ is a function dependent on depth with $f(0)=1$ and $f(x=\infty)=0$. T_{eff} can then be described by:

$$
\begin{aligned}
T_{eff} &= \int_0^{\infty}\left[T_{\infty}+\left(T_1-T_{\infty}\right)f\left(x\right)\right]\alpha\left(x\right)\exp\left[-\int_0^{x}\alpha\left(x'\right)dx'\right]dx \\
&= \int_0^{\infty}T_{\infty}\alpha\left(x\right)\exp\left[-\int_0^{x}\alpha\left(x'\right)dx'\right]dx \\
&\quad+\int_0^{\infty}\left(T_1-T_{\infty}\right)f\left(x\right)\alpha\left(x\right)\exp\left[-\int_0^{x}\alpha\left(x'\right)dx'\right]dx \\
&= T_{\infty}\int_0^{\infty}\alpha\left(x\right)\exp\left[-\int_0^{x}\alpha\left(x'\right)dx'\right]dx \\
&\quad+\left(T_1-T_{\infty}\right)\int_0^{\infty}f\left(x\right)\alpha\left(x\right)\exp\left[-\int_0^{x}\alpha\left(x'\right)dx'\right]dx
\end{aligned}
\tag{2.5}
$$

where it is assumed that α is constant or linear within each layer. Alternatively, assuming that these two layers have the same soil moisture, and texture, the derivation could be further stated as:

$$
T_{eff}=T_{\infty}+\left(T_1-T_{\infty}\right)C \tag{2.6}
$$

where $C=\int_0^{\infty}f\left(x\right)\alpha\left(x\right)\exp\left[-\int_0^{x}\alpha\left(x'\right)dx'\right]dx$. Equation (2.6) has been used in a series of ground calibration experiments and was further developed by estimating C from soil permittivity [87] and soil moisture information [80, 109]. The sampling depth of microwave radiation is implicit in Equation (2.2) [65]. If we suppose that there are two homogeneous soil layers, Choudhury's scheme follow. The last term of Equation (2.5) may be simplified to $\left(T_1-T_{\infty}\right)C$, while the first term equals T_{∞}. Thus presented, the T_{eff} scheme by Choudhury（1982）is a simplified form of Wilheit's (1978) scheme. The empirical Equation (2.6) is a simplification of Equation (2.2). However, this simplification is derived without a detailed physical explanation. The parameter C is comprised of a series of empirical constants that can only be acquired in a few specified bands. For other bands, it is not possible to infer C by an interpolation method, because C is supposed to be an empirical parameter determined by a least-square method. In practice, this may lead to huge differences [100].

Understanding C based on a physical explanation using a soil moisture profile has been investigated in many studies. Wigneron et al. (2001) developed a new algorithm to estimate soil effective temperature using the L band: $T_{eff}=T_{\infty}+\left(T_1-T_{\infty}\right)\cdot\left(w_s/w_0\right)^b$, where w_s is the 0–3 cm surface soil moisture (this depth interval corresponds well with the effective soil moisture value contributing to soil emission in the L band), and w_0 and b are semi-empirical parameters depending on specific soil characteristics [80]. The scheme is further improved by considering soil properties when estimating w_0/b, using a range constraint of $min\left[\left(\frac{w_s}{w_0}\right)^b,1\right]$ [109]. $min\left[\left(\frac{w_s}{w_0}\right)^b,1\right]$ is required by the definition of $f\left(x\right)$. This scheme is successfully adopted in the SMOS soil moisture retrieval algorithm (Kerr et al. 2012). Holmes et al. (2006) presented a similar algorithm using the L band: $T_{eff}=T_{\infty}+\left(T_1-T_{\infty}\right)\cdot\left(\left(\varepsilon''/\varepsilon'\right)/\varepsilon_0\right)^b$ with parameters ε_0 and b,

and where $(\varepsilon''/\varepsilon')$ is calculated from soil moisture according to the dielectric mixing model. Parameters in these two models are retrieved empirically through experiments.

Any integral equation can be numerically simplified based on certain assumptions. Hypothetically, $x_0 = 0$ represents the soil surface as well as the upper boundary for the first layer; x_{i-1} and x_i are the upper and lower boundaries, respectively, of the i th layer, whereas the thickness of the i th layer is Δx_i . For a specified wavelength and soil texture, if soil temperature and moisture within a layer are constant ($T(x)\big|_{x_{i-1}}^{x_i} = T_i$ and $\alpha(x)\big|_{x_{i-1}}^{x_i} = \alpha_i$), Equation (2.2) can approximate the real. Assuming that soil temperature and moisture are constant within both the $(0, x_1)$ and the (x_1, ∞) layer (which is also the assumption in Choudhury's scheme), the equation can be simplified as:

$$\begin{aligned} T_{eff} &= \int_0^{x_1} T_1\alpha_1 \exp\left[-\int_0^x \alpha_1 dx'\right]dx + \int_{x_1}^{\infty} T_2\alpha_2 \exp\left[-\int_0^x \alpha dx'\right]dx \\ &= T_1\alpha_1\int_0^{x_1} e^{-\alpha_1 x}dx + T_2\alpha_2\int_{x_1}^{\infty} e^{-\alpha_1 x_1 - \alpha_2(x-x_1)}dx \\ &= -T_1\left(e^{-\alpha_1 x_1} - 1\right) + T_2 e^{-\alpha_1 x_1} \end{aligned} \tag{2.7}$$

where we assumed that $\alpha_1 \approx \alpha_2$ (uniform soil moisture) in the last step. The dielectric constant in Choudhury's scheme does not require information about α , which implies that soil moisture is constant along the vertical profile. The above equation can be further simplified as:

$$T_{eff} = T_1\left(1 - e^{-B_1}\right) + T_2 e^{-B_1} \tag{2.8}$$

where $B_1 = \alpha_1 x_1$. The above equation will be used as Lv's scheme. By comparing Equation (2.8) with Equation (2.6), C is given as:

$$\begin{aligned} C &= 1 - e^{-B_1} \\ &= 1 - \exp\left(-\Delta x \cdot \frac{4\pi}{\lambda} \cdot \frac{\varepsilon''}{2\sqrt{\varepsilon'}}\right) \end{aligned} \tag{2.9}$$

Hence, C is related to wavelength λ , soil moisture (e.g., the dielectric constant, with ε'' the imaginary part and ε' the real part), and sampling depth Δx . The soil surface temperature is implicitly connected to C as well since it can affect the dielectric constant [114]. All variables in Equation (2.9) have physical implications. As such, C is no longer an empirical parameter but an analytical expression. Since λ and Δx are known for the target microwave sensors and experiment configurations, it will be possible, once soil moisture and temperature data are available, to calculate C (or B_1) according to Equation (2.9). Defined as the optical thickness related to the wavelength, B_1 can be rewritten as follows:

$$B_1 = \Delta x \cdot \frac{4\pi}{\lambda} \cdot \frac{\varepsilon''}{2\sqrt{\varepsilon'}} \tag{2.10}$$

If B_1 is taken as a constant in the L band, then the ratio between Δx and λ is:

$$\frac{\Delta x}{\lambda} = \frac{\sqrt{\varepsilon'}}{2\pi\varepsilon''} B_1 \tag{2.11}$$

where $\frac{\sqrt{\varepsilon'}}{2\pi\varepsilon''}$ is determined by both soil moisture and temperature. In this chapter, Peplinski's scheme [114] is adapted to calculate the dielectric constant components.

2.2.2 *In-situ* Dataset

To test Lv's scheme stated in Equation (2.8), a series of soil temperature and moisture profiles, observed at the Maqu Climate and Environment Observatory in the water source region of the Yellow River, is used [115-117]. Maqu is located at the eastern margin of the Tibetan Plateau at an elevation of about 3000 meters above sea level. The Maqu network was set up in 2008 with 20 sites for monitoring soil moisture and temperature profiles, providing the information for the validation of satellite-derived soil moisture products. Here, we only use the soil temperature/moisture data from the Maqu station, which is the main station of the network. Table 2.1 summarizes an insight into the variation in soil moisture and soil temperature at Maqu station. These data will be used in the configuration of Lv's scheme and the comparisons made in Section 2.3. The assumption $C = const$ in Choudhury's scheme is not applicable to the Maqu region due to the heterogeneity in soil properties [100]. For most sites of Maqu networks the data are collected at a depth of 5 cm and 10 cm, which differs from the surface layer (e.g., at 3 cm) and the deep layer (e.g., at 2 m depth) used in Choudhury's scheme.

Table 2.1 Data from observations at the Maqu station (May 1, 2009-April 30, 2010). The experiment field is located at the east edge of Qinghai-Xizang Plateau and covered in grass in summer (Su et al 2011; Dente et al. 2012a, b). Observation of the soil temperature/moisture data is performed at six depths (with an extra infrared surface temperature sensor).

Layer	Depth	Soil Temperature(℃)			Soil Moisture ($m^3 \cdot m^{-3}$)		
		Mean	Max	Min	Mean	Max	Min
1	0 cm	4.594	32.639	-21.665	—	—	—
2	5 cm	4.503	26.669	-10.043	0.138	0.304	0.026
3	10 cm	4.289	19.149	-7.302	0.271	0.428	0.094
4	20 cm	4.644	16.754	-5.085	0.235	0.342	0.095
5	40 cm	5.887	16.377	-1.814	0.239	0.328	0.117
6	80 cm	4.979	13.785	-0.487	0.178	0.229	0.126
7	160 cm	5.450	11.979	0.875	0.161	0.174	0.139

2.3 Results

In this section, the meaning of C to introduce Equation (2.9) is analyzed. Its mathematical behavior is tested synthetically to show the impact of different factors on C (e.g., wavelength, sampling depth, soil moisture, and soil temperature). Next, Lv's scheme is compared to Choudhury's, Wigneron's and Holmes' schemes.

2.3.1 Physical Implication of Parameter *C*

Based on Equation (2.9), Figure 2.1 shows the dependency of the parameter C on wavelength, soil moisture, sampling depth, and soil temperature. One of the advantages of Lv's scheme is that the parameter B_1 does not need to be calibrated with the *in-situ* observation data or model simulation outputs.

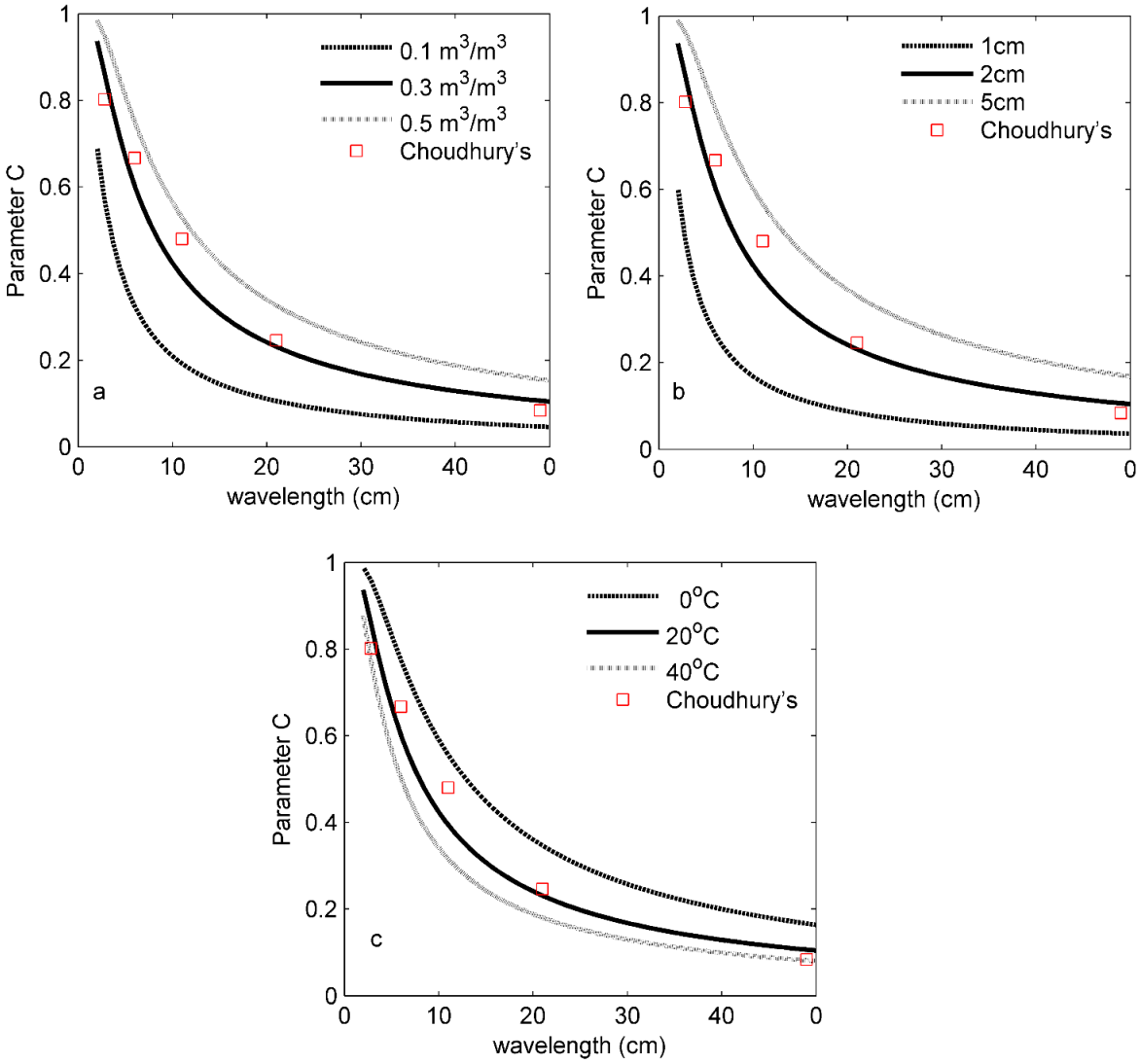

Figure 2.1 Relation between C (Equation 2.9) and wavelength for ranges of surface soil moisture (a), sampling depth (b), and surface soil temperature (c). For each varying parameter, the two others are fixed, namely: soil moisture at 0.3 m^3 m^{-3} (b,c), sampling depth at 3cm (a,c), and surface soil temperature at 20 °C (a,b). Red squares show the relation obtained using Choudhury's model. The rightmost squares in each panel indicate C at L band.

Figure 2.1 shows that soil moisture and soil temperature at the first monitoring and sampling depth (i.e., the first depth for T_{eff} inputs) affect C, which will subsequently affect the calculation of T_{eff}. The soil temperature and soil moisture at the first monitoring and sampling depth represents the soil temperature/moisture from zero to the depth that divides the two layers. Since then, T_{∞} is not necessary for Figure 2.1. Choudhury et al. (1982) listed empirical parameters C for five specific wavelengths. For the wavelengths 2.8, 6.0, 11.0, 21.0, and 49.0 cm, these C values were 0.802, 0.667, 0.48, 0.246, and 0.084, respectively (the red squares in Figure 2.1), implying a dependence of C on a wavelength only.

Comparison between Lv's scheme and Choudhury's scheme reveals good agreement at a surface soil temperature of 20°C, and surface soil moisture of 0.3 m^3/m^3, both typical values for the monsoon season at Maqu, and a sampling depth of 3 cm. This proves the ability of Equation (2.9) to explain the physical meaning of parameter C. Equation (2.9) is an (almost) exact equation under the two-layer model. It also provides an estimation of C beyond the five specific bands used by Choudhury.

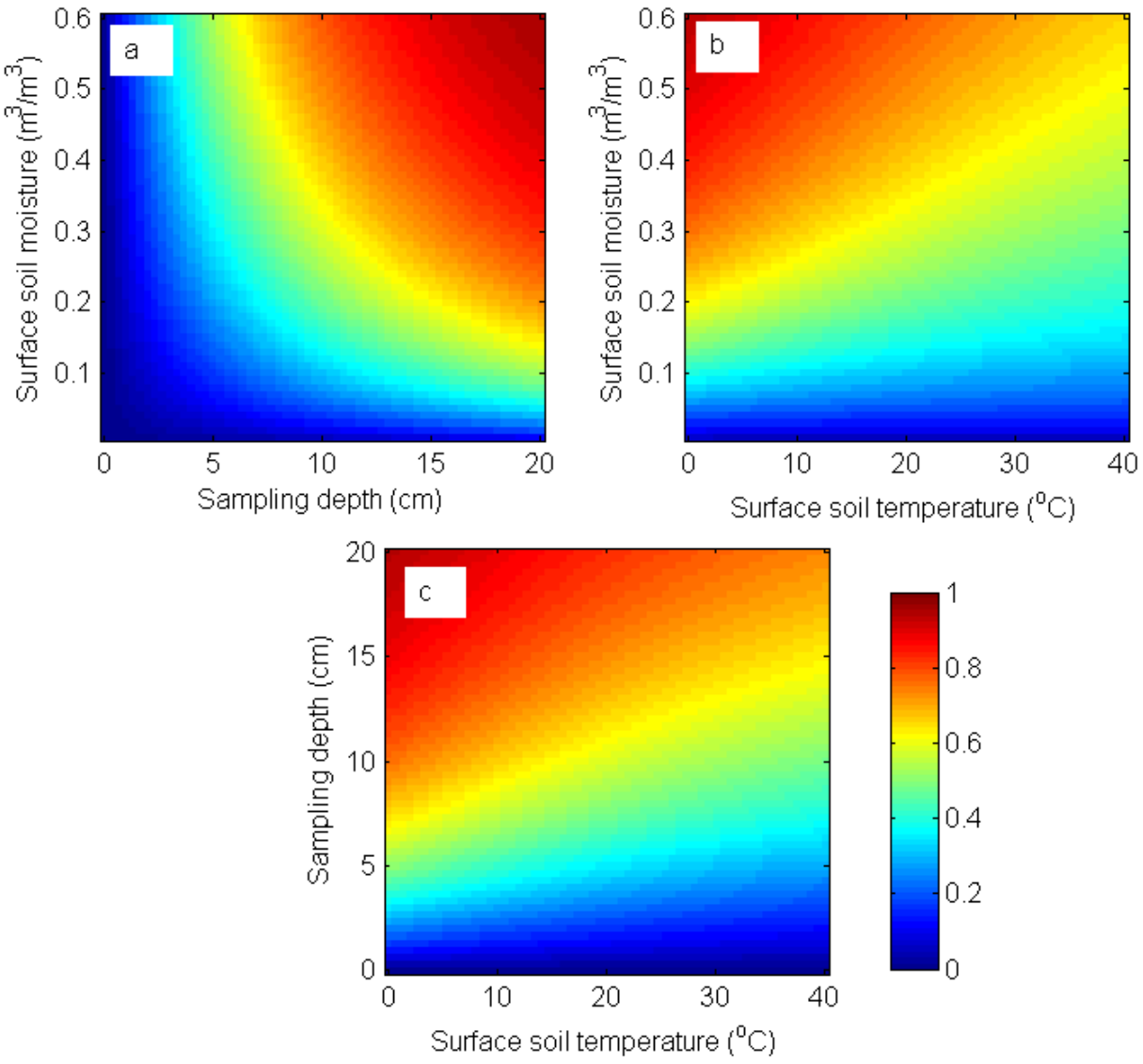

Figure 2.2 For the L band (wavelength = 21 cm), the dependence of parameter C on surface soil moisture, soil temperature, and sampling depth. For each pair of varying parameters, the third one is fixed, namely: surface soil temperature at 20°C (a), sampling depth at 3cm (b), and soil moisture at 0.3 m^3 m^{-3} (c).

Identical to what has been found in Wigneron et al. (2008) and Holmes et al. (2006), Figure 2.1 also shows that C is positively proportional to both surface soil moisture and sampling depth, while it is

negatively proportional to surface soil temperature. Even though these three variables affect the calculation, the pattern of C varying according to the wavelength is similar, which is decreasing with increasing wavelength (Figure 2.1). According to Equation (2.10) and Figure 2.1, it can be inferred that the deeper soil temperature may be disregarded for wavelengths of less than 1 cm, at which the C can be more than 0.9. It means that the weight assigned to the deeper soil temperature for calculating T_{eff} is less than 0.1. On the other hand, the deeper layer will account for more than 80% of the weight in calculating T_{eff} with wavelengths exceeding 50 cm. Figure 2.1a shows that the value of parameter C decreases when the soil moisture decreases, so that Choudhury's scheme becomes unsuitable for extreme dry soil when using the L band, as its C is a constant of 0.246.

Figure 2.2 shows the dependence of C on surface soil moisture, soil temperature, and sampling depth, for the L band. The range of the inputs is defined to cover the variation in soil moisture, soil temperature and sampling depth at the Maqu station. With the sampling depth varying from 0 to 20 cm, C varies from 0 to over 0.8 with increasing soil moisture content (Figure 2.2a). It shows that a large part of the signal $(C > 0.5)$ can be attributed to the first layer, namely where the sampling depth exceeds 10 cm, and the soil moisture content exceeds 0.15 $m^3 \cdot m^{-3}$ (Figure 2.2a). Surface soil moisture and temperature also affect C (e.g., through the dielectric constant) (Figure 2.2b, 2.2c). The difference in C can be more than 0.3 when soil temperatures vary between 0°C and 40°C (Figure 2.2b), and soil moisture content exceeds 0.15 $m^3 \cdot m^{-3}$ (only soil temperatures above 0°C are considered in this chapter). Generally, soil moisture and sampling depth affect C in a comparable manner (Figure 2.1a, 2.1b & Figure 2.2a, 2.2b).

2.3.2 Inter-comparison of Parameterization Schemes

For Choudhury's, Wigneron's, Holmes', and Lv's scheme listed in Table 2.2, the Choudhury's parameter are cited, while the parameters in Wigneron's and Holmes' schemes are calibrated and fitted with the *in-situ* observation at the Maqu station for the L band. For Wigneron's scheme, the soil properties (clay 9.38%, silt 56.34%, sand 34.28%) and bulk density (1.264 $g \cdot cm^{-3}$) collected at Maqu station are also adapted to calculate the parameters. The fitting parameters are also listed in Table 2.2. In Lv's scheme the proposed new parameter B_1 is calculated by Equation (2.10), using the averaged soil moisture and soil temperature at a depth of 5 cm. The comparisons between the schemes are shown in Figure 2.3 and Figure 2.4.

Table 2.2. Different schemes used for calculating T_{eff} . The Choudhury's parameter is cited, while the parameters in Wigneron's and Holmes' schemes are calibrated and fitted with the in situ observation. The parameter B_1 for Lv's scheme in this table is calculated from measurements collected from May 21 to June 9, 2009.

Name	Parameterization	C	Parameters
Choudhury	$T_{eff} = T_\infty + \left(T_1 - T_\infty\right)\underline{C}$	C	0.246
Holmes	$T_{eff} = T_\infty + \left(T_1 - T_\infty\right)\underline{\left((\epsilon''/\varepsilon')/\varepsilon_0\right)^b}$	$\left((\epsilon''/\varepsilon')/\varepsilon_0\right)^b$	$\varepsilon_0 = 0.13,$ $b = 0.85$
Wigneron	$T_{eff} = T_\infty + \left(T_1 - T_\infty\right)\underline{(w_s/w_0)^b}$	$min\left[\left(\frac{w_s}{w_0}\right)^b, 1\right]$ b and w_0 are function of the soil type	$w_0 = 0.5996$ $b = 0.358$
Lv	$T_{eff} = T_\infty + \left(T_1 - T_\infty\right)\underline{(1 - e^{-B_1})}$	$(1 - e^{-B_1})$	$B_1 = 0.965$

Table 2.2 shows that all schemes consider T_{eff} being a linear function of T_1 and T_∞. We define the coefficient after the term $\left(T_1 - T_\infty\right)$ as the weight function (the C column in Table 2.2). The weight functions, or their parameters (in the L-band, $\lambda = 21cm$), of all schemes, are also listed in Table 2.2. In Choudhury's scheme, the weight coefficient is constant, while in both Wigneron's and Holmes' scheme the weight function varies with soil moisture.

Figure 2.3 compares Wigneron's and Holmes' scheme with Lv's scheme for the L band, leaving Choudhury's scheme out as its parameter C is constant. When the soil surface is extremely dry, C calculated by each of the three schemes drops dramatically, approaching zero as surface soil moisture is approaching to zero. This is reasonable, as microwave radiation emitted from a deeper layer will easily reach the soil surface when the soil is dry. As the soil is moister, the radiation emitted from a deeper layer becomes weaker (e.g., C in Equation (2.9) will be greater), and the wet surface layer carries more weight. Equation (2.9) indicates that C can be infinitely approaching 1 with increasing soil moisture. In Wigneron's scheme, the calculation of the weight function under the constraint of $min\left[\left(\frac{w_s}{w_0}\right)^b, 1\right]$ is used to match this theoretical limit of C. Figure 2.3a shows that the C of Wigneron's scheme is close to 1 when the soil moisture is 0.6 $m^3 \cdot m^{-3}$. With the same soil moisture content, the Holmes's C is about 0.65 and Lv's C varies from 0.5 to 0.9 with the sampling depth changing from 1 to 15 cm. Figure 2.3 clearly shows that C

can vary to a certain extent depending on sampling depth and temperature. Figure 2.3 also shows that Lv's scheme can reflect changes in C, while other schemes show no difference in C for different sampling depths and soil temperatures. Finally, Figure 2.3 shows that the difference between Lv's scheme and Choudhury's scheme can exceed 50%, when soil moisture is larger than 0.1 $m^3 \cdot m^{-3}$.

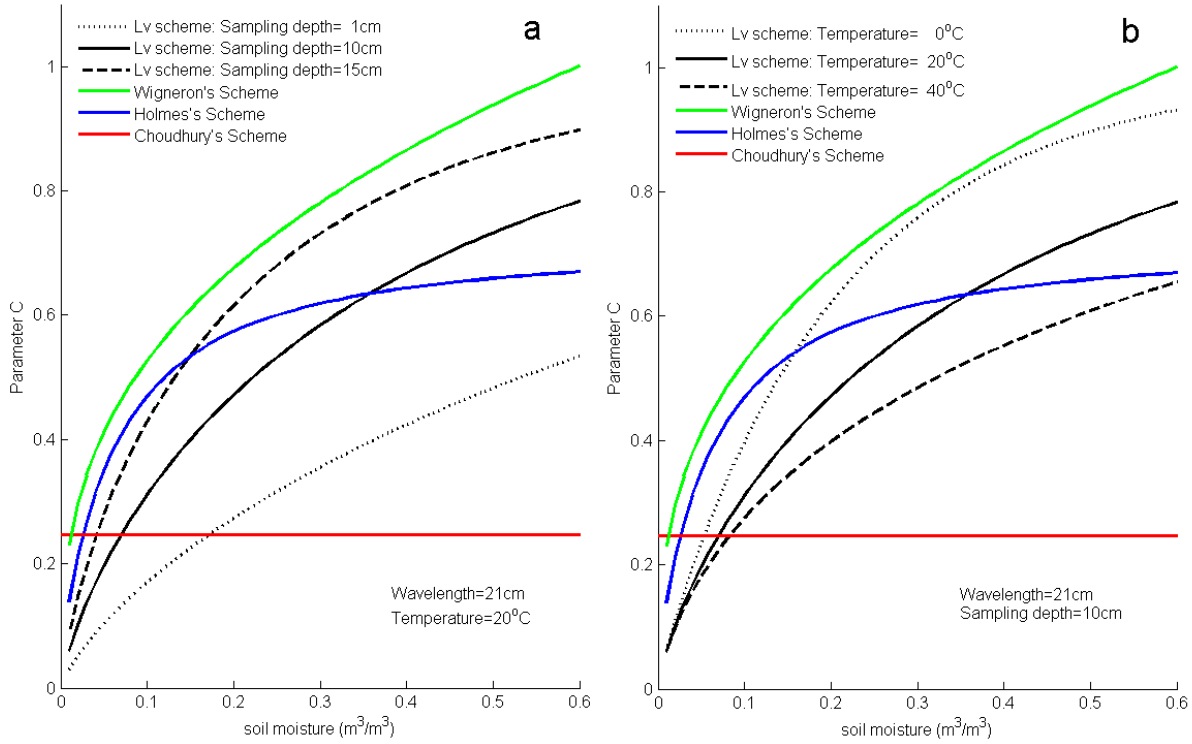

Figure 2.3 Comparison of different parameterization schemes of C concerning their dependence on soil moisture, sampling depth, and soil temperature, for the L band (wavelength = 21cm). The black lines represent Lv's scheme.

So far, Lv's scheme has shown its capacity to physically explain extreme soil moisture conditions. Figure 2.4 compares Choudhury's, Holmes', Wigneron's, and Lv's schemes to the integral scheme (e.g. "'theoretical" values of T_{eff} calculated from Equation (2.2)). For the schemes used in Table 2.2, the soil moisture/temperature is supposed to be measured at 5 cm depth for the surface layer and 160 cm depth for the deep layer. Soil moisture and soil temperature at all layers are used in the integral scheme. Since the empirical parameters of Holmes' and Wigneron's schemes are calibrated using the *in-situ* observations at Maqu station, we can see a clear correlation in Figure 2.4b and 2.4c, but the Choudhury's result deviates much further from the 1:1 line in Figure 2.4a. On the other hand, without calibrating B_1, which is estimated directly from observations, Lv's scheme achieves an accuracy matching that of the calibrated schemes (Figure 2.4d). The correlation coefficient (CC) for Lv's scheme is 0.93 (RMSE=2.4386 K), for Wigneron's scheme 0.95 (RMSE=1.8453 K), for Holmes' scheme 0.82 (RMSE=3.4890 K), and for Choudhury's scheme 0.71 (RMSE=4.0053 K).

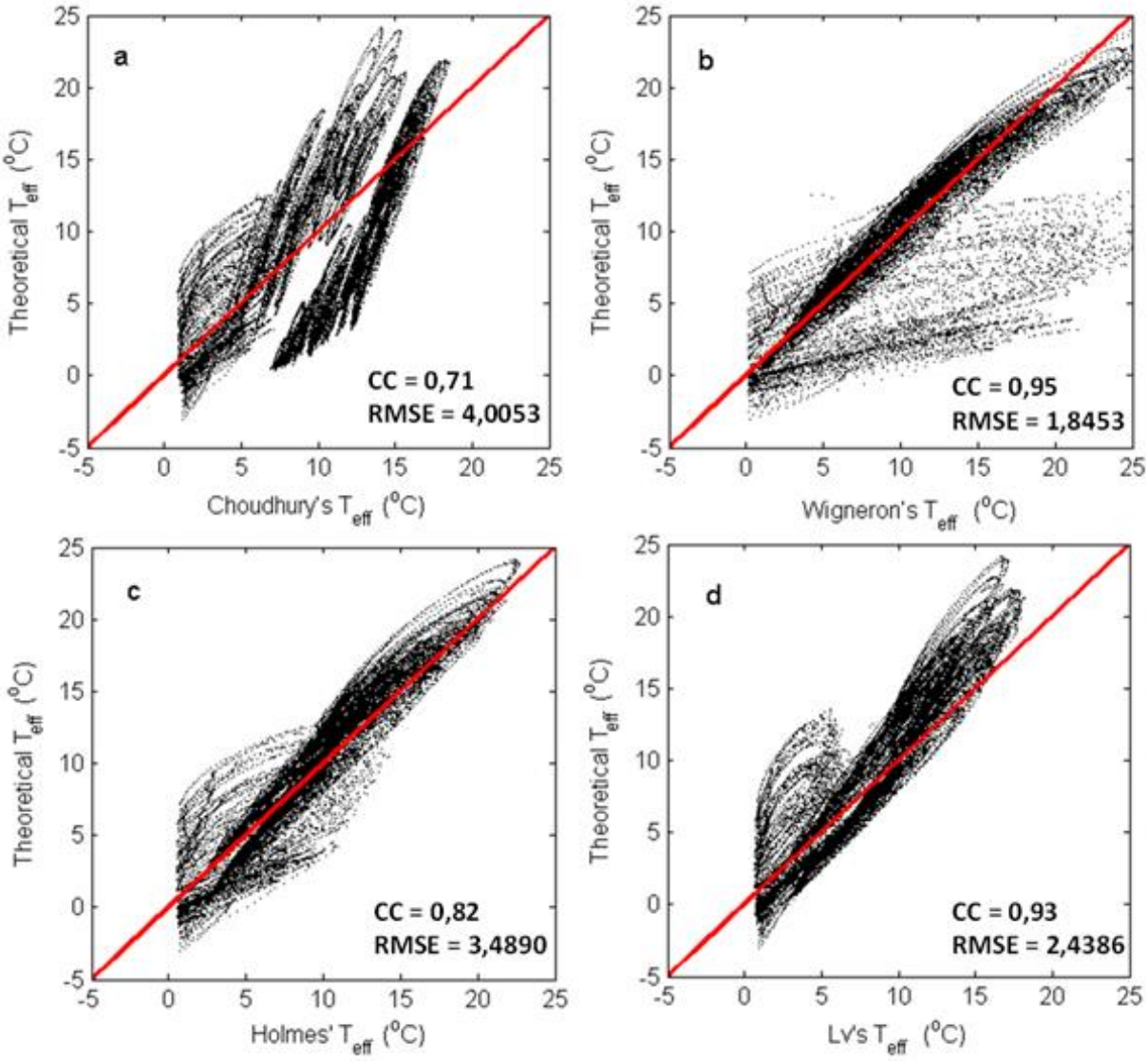

Figure 2.4 Comparison between different parameterization schemes of T_{eff} and the "'theoretical" value of T_{eff} calculated by Equation (2.2). The Holmes' and Wigneron's schemes have been calibrated with in situ data from Maqu station

The reasons for the differences shown in Figures 2.3 and 2.4 could also be inferred from their mathematic forms listed in Table 2.2. Compared to Choudhury's scheme, Wigneron's and Holmes' schemes are improved by the introduction of soil moisture into C. Actually, soil temperature is also indirectly considered in Holmes' scheme since surface soil temperature is used as input in the calculation of the dielectric constant. In addition to soil moisture, soil properties are also considered in Wigneron's scheme. Both Wigneron's and Holmes' schemes refer to surface soil moisture when describing the impact of the upper soil layer on the deeper soil layer. In Wigneron's scheme w_s denotes surface soil moisture, and $\left(\frac{\varepsilon''}{\varepsilon'}\right)$

is calculated from w_s in Holmes' scheme using the dielectric mixing model that depends on both soil moisture and temperature at the surface. In this case, the weighting function will not only vary with surface soil moisture but also with surface soil temperature. Lv's scheme is a simplified form of Wilheit's scheme, conserving its physical meaning with a two-layer scheme (see Section 2.4 for discussion on this point). It is more flexible, with a parameter of B_1 linking the weight coefficient C to soil moisture/temperature, sampling depth, and wavelength. One note is appropriate here, because vegetation as well as freezing/thawing processes will affect the radiation received by the satellite sensors [118], and further study is needed on an improved, effective temperature scheme for such conditions.

2.4 Discussion

2.4.1 Determination of Δx

From Equations (2.8) and (2.9), wavelength, soil moisture, Δx , and soil temperature are all needed to calculate the real-time or averaged parameter B_1. Soil temperature and soil moisture can be provided by in situ data or by a numerical model output, and wavelength is a constant once the satellite sensors are identified. Hence, only the knowledge of Δx is needed to calculate B_1. Since the wavelength is known for each frequency of interest (for instance, 1.4 GHz for SMOS and SMAP), and both soil moisture and soil temperature are observed, the only unknown parameter in Equation (2.8) is Δx . Δx is not readily determined just based on experience. Equation (2.8) assumes that T_1 stands for the mean soil temperature of the first layer, while $1-e^{-B_1}$ is its weight function. The same assumptions are made for the second layer regarding T_2 and e^{-B_1}. With the assumption in Lv's scheme, it could be inferred that the result would only be optimal if 1) the depth-averaged soil temperature represented by T_1 matched with Δx in $1-e^{-B_1}$ and 2) the depth-averaged soil temperature represented by T_2 matching with the integration from Δx to infinite deep as in Equation (2.2). In order to simplify the problem, we only discuss the first requirement. Considering the integral exponential function $\int e^{-x}dx = 1-e^{-x}$, the weight for the first layer could be rewritten as $1-\mathrm{e}^{-B_1} = \int_0^{B_1} \mathrm{e}^{-B}\, dB$. As soil moisture/temperature is supposed to be uniform in the assumption of Equation (2.8), B is also uniform and does not vary with depth, i.e. $\int_0^{B_1} \mathrm{e}^{-B}\, dB = \mathrm{e}^{-B}\cdot B_1$. Replacing the subscript with physical depth could infer that, for the data at Maqu center station, solving $1-\mathrm{e}^{-B_{\Delta x}} = \mathrm{e}^{-B_{0.05cm}}\cdot B_{\Delta x}$ using average soil moisture/temperature values would result in Δx being set to 0.11 m. $\Delta x = 0.11$ m is also used in previous figures. The same strategy can be adopted for the second layer to acquire an optimal T_{eff} estimation, but this is a complex problem and will be explained in further work.

2.4.2 Discrete formulation of the Lv Scheme

From the discussion presented in Section 2.3 can be deducted that the deeper the first layer is, the larger the weight on T_1 will be for calculating T_{eff}. All four T_{eff} schemes work on the assumption that both soil moisture and soil temperature should be homogeneous within the first layer as well as within the deeper layer. Thus, if the sampling depth Δx straddles a jump layer in the field, the B_1 will lose its representativeness and affect the T_{eff} remarkably. Such an abruption may be caused by texture, organic matter, soil moisture/temperature profiles, as well as by micrometeorological conditions (e.g., storms, rainfall). Therefore, it is necessary to evaluate whether a multi-layer scheme is needed.

A rainfall event with an intensity of nearly 2 mm/day, as occurred on 21 May 2009, causes a dramatic change in the soil temperature profile, especially at the top layer. The daily average soil temperature varies dramatically by about 10°C within the top 40 cm, whereas the average soil temperature remains stable in the bottom layer. This partly indicates the need for the development of a discrete algorithm to calculate T_{eff}, in preference to simply using two layers. To develop such an algorithm for estimating T_{eff}, the soil was divided into multiple layers in accordance with the available data.

Equation (2.9) can be extended into a multilayer scheme based on soil profile information. T_{eff} can then be estimated using a set of numerical simulations. The T_2 in Equation (2.8) can be composed of the subsurface temperature right beneath the first layer plus the temperature of the bulk of the soil, situated below this subsurface layer. T_2 can then be expressed as:

$$T_{\infty} = T_2\left(1-e^{-B_2}\right)+T_3e^{-B_2} \tag{2.12}$$

where T_3 is the soil temperature of the deeper layer. In Equation (2.12), T_3 is an update of T_2 after the first interpolation. After inserting Equation (2.12) into Equation (2.8), a triple-layer algorithm is derived as follows:

$$T_{eff} = T_1\left(1-e^{-B_1}\right)+\left[T_2\left(1-e^{-B_2}\right)+T_3e^{-B_2}\right]e^{-B_1} \tag{2.13}$$

Leading into a multilayer algorithm, to be expressed as:

$$T_{eff} = T_1\left(1-e^{-B_1}\right)+\sum_{i=2}^{n-1}T_i\left(1-e^{-B_i}\right)\prod_{j=1}^{i-1}e^{-B_j}+T_n\prod_{j=1}^{n-1}e^{-B_j} \tag{2.14}$$

where $B_i = \Delta x_i \cdot \frac{4\pi}{\lambda}\cdot\frac{\varepsilon_i''}{2\sqrt{\varepsilon_i'}}$; Δx_i is defined by the space interval in accordance with the configuration of the different experiments, and $\frac{\varepsilon''}{2\sqrt{\varepsilon'}}$ is calculated by the dielectric mixing model.

The above discrete procedure has a clear physical implication. Equation (2.14) allows for all measurements made in the soil column to be incorporated in order to obtain a more accurate T_{eff}, without disturbing the original part concerning the topsoil layer of Equation (2.8), and only modifying the weights for the residual terms related to deeper soil layers. As a result, an accurate T_{eff} could be calculated from observations of each layer. Equation (2.14) can also be used as a numerical reference to evaluate the adequacy of different schemes in estimating T_{eff} as shown in Figure 2.4.

2.5 Conclusions

A detailed mathematical derivation has been presented to show that Lv's scheme is a simplified form of Ulaby's and Wilheit's radiative transfer theories [98]. Lv's scheme explains the physical meaning of Choudhury's semi-empirical parameter C. Mathematical and physical implications are assigned to the parameter C, as a function of sampling depth, soil moisture, soil physical temperature, and wavelength. The performance of Lv's scheme has been evaluated using in situ soil moisture and temperature measurements.

It can be inferred that with wavelengths shorter than 1 cm the deeper soil temperature may be neglected, and with wavelengths exceeding 50 cm the deeper soil layer shall account for more than 80% weight in computing effective temperature. Also, Lv's scheme may be applied in a wide range of soil conditions, even extreme conditions (e.g., extremely dry or wet). Lv's scheme is physically close to Wilheit's radiative transfer theory, and there is no need to estimate an empirical parameter. The parameter B_1 can be calculated directly from observations or model outputs.

To further explore the capabilities of Lv's two-layer scheme, a discrete form was developed. By calculating T_{eff} using this discrete form, the strong effect caused by jumping in the soil layer (e.g., through texture change) can be avoided. Furthermore, all measurements may be incorporated, thus enabling the provision of an accurate estimation of T_{eff}. However, no straightforward validation using passive microwave data has been incorporated in this chapter. All calculations are based on in situ soil temperature and soil moisture measurements from Maqu station. In situ passive microwave data are necessary when further validating Lv's scheme, and more field experiments in areas with different soil properties are needed.

Chapter

3 Determination of the Optimal Mounting Depth for Calculating Effective Soil Temperature at L-Band: Maqu Case[2]

Abstract: Effective soil temperature T_{eff} is a basic parameter in passive microwave remote sensing of soil moisture. At present, dedicated satellite soil moisture monitoring missions use the L-band as the operating frequency. However, T_{eff} at the L-band is strongly affected by soil moisture and soil temperature profiles. In Chapter 2, a two-layer scheme and a corresponding multilayer form have been developed that accommodate such influences. In this Chapter, soil moisture/temperature data collected and simulated by the Noah land surface model across the Maqu Network are used to evaluate the newly developed scheme. There are two key findings. Firstly, the new two-layer scheme can assess which site provides relatively higher accuracy when estimating T_{eff} . It is found that, on average, nearly 20% of the T_{eff} signal cannot be captured by the Maqu Network, in the currently assumed common installation configuration. This is important since the spatially averaged brightness temperature (a function of T_{eff}) is used to determine soil moisture. Secondly, the developed method let us identify 5 cm and 20 cm as optimal mounting depths for observation pairs for calculating T_{eff} at the central station in the Maqu Network, and provides an objective way to configure optimal soil moisture/temperature networks.

Key Words: microwave remote sensing; soil effective temperature; soil moisture; Maqu Network; Tibetan Plateau

[2] This chapter is based on

Shaoning Lv, Yijian Zeng, Jun Wen, Donghai Zheng, Zhongbo Su. 2016. Determination of the Optimal Mounting Depth for Calculating Soil Effective Temperature at L-band: Maqu Case. Remote Sensing, DOI: 10.3390/rs8060476

3.1 Introduction

3.1.1 Motivation

Soil moisture is one of the essential climate variables (ECVs) [1, 5, 118, 119]. Over land, soil moisture relates to the storage of water and heat that can be released several months later similar to vegetation cover and snow [11, 14, 120]. Even though the total energy represented by soil moisture is not comparable to that of the sea surface temperature, soil moisture could still constitute the weather forecast turning point in studies on land-atmosphere interaction, seasonal climate forecasting and numerical simulations [16, 121, 122]. Soil moisture is also an indicator of drought and flood events, which are key threats to agriculture, hydrology, and ecology, among others.

For decades, scientists have tried to estimate the global soil moisture distribution through *in-situ* observations, numerical simulations, and remote sensing. Passive remote sensing from satellites using L-band (1.4 GHz) is considered the most promising tool for generating such maps. Both the Soil Moisture and Ocean Salinity (SMOS, launched in 2009) and the Soil Moisture Active Passive (SMAP, launched in January 2015) missions use L-band as their operating channel [40, 123]. The accuracy of soil moisture retrievals at L-band depends on the knowledge of the effective soil temperature (T_{eff}) and sampling depth (i.e., the layer of the soil column mainly generating the radiometer signal [124, 125]). At L-band, the sampling depth varies from 0 to several centimeters below the surface (e.g., for wet soil) [126] which will directly affect the estimation of T_{eff}. To calibrate and validate the soil moisture estimates from SMOS and SMAP, *in-situ* observations are needed. Thus the quality of the T_{eff} estimate is important [76, 87]. When installing soil moisture sensors, their mounting depth is of great importance. To date, a mounting depth for the sensors most relevant to absorbs, have not been identified. This chapter identifies the optimal mounting depth through analyzing the definition of T_{eff}, and derive a mathematical formulation which provides instructions on how to configure this mounting depth.

3.1.2 Background

The physical concept of effective soil temperature T_{eff} was developed to describe the emissive capacity of a soil column. According to the Rayleigh-Jeans approximation, switched for the microwave domain, the emitted energy from the soil is proportional to the thermodynamic temperature [112] and the brightness temperature T_B, which is proportional to the emitted radiation intensity is expressed as:

$$T_B = \varepsilon T_{eff} \tag{3.1}$$

where T_B relates to the radiation intensity received by a passive microwave sensor fixed near the soil surface or on the satellite platforms while neglecting the attenuation and emission of the atmosphere. ε is

the emissivity that is strongly related to soil moisture. T_{eff} is the effective temperature and is formulated by Wilheit [73] as:

$$T_{eff} = \int_0^{\infty} T(x)\alpha(x)\exp\left[-\int_0^{x}\alpha(x')dx'\right]dx \tag{3.2}$$

where $\alpha(x) = \frac{4\pi}{\lambda}\varepsilon''(x) \Big/ 2\left[\varepsilon'(x)\right]^{\frac{1}{2}}$. Equation (3.2) states that T_{eff} at the soil surface is a superposition of the intensities emitted at various depths within the soil.

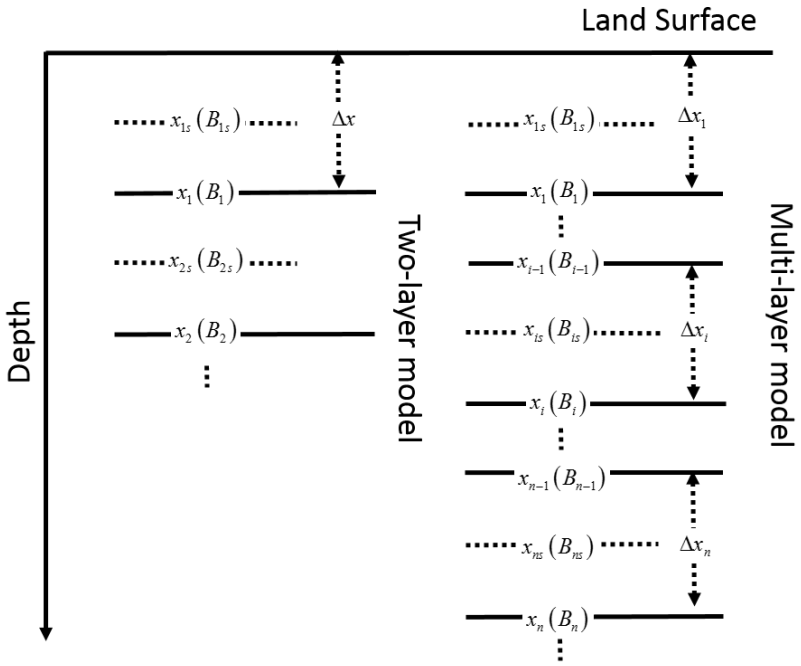

Figure 3.1. Schematic of subscripts related to individual soil layers notation.

The knowledge of T_{eff} is critical for accurate values of soil emissivity from brightness temperature measurements because only the soil moisture can be retrieved from the estimates of soil emissivity [112]. However, to find soil moisture and soil temperature profile is usually limited. Observation points are installed empirically or assume to be continuous with constant vertical intervals. Recently, a new two-layer scheme (hereafter Lv's scheme) has been derived directly from Equation (3.2). This is expressed by Lv *et al.* [127] as:

$$T_{eff} = T_1\left(1 - e^{-B_1}\right) + T_2 e^{-B_1} \tag{3.3}$$

in which $B_1 = \Delta x \cdot \frac{4\pi}{\lambda} \cdot \frac{\varepsilon''}{2\sqrt{\varepsilon'}}$ is a parameter related to wavelength (λ), soil moisture through the dielectric constant (ε'' is the imaginary part and ε' is the real part), and to depth (Δx). The dielectric model used in

this chapter is Mironov's model which has also been adopted by SMOS [83]. Soil moisture/temperature profiles (hereafter SM/ST) can be obtained from *in-situ* observation networks (e.g., Maqu Network). λ is a constant for the specific sensors, i.e., $\lambda = 21$ cm for SMOS and SMAP. This leaves the depth, which is interval if more than two layers are available, as the only unknown in Equation (3.3). Equation (3.3) can be further developed into a multi-layer scheme by [127]:

$$T_{eff} = T_1\underline{\underline{\left(1-e^{-B_1}\right)}} + \sum_{i=2}^{n-1} T_i\underline{\underline{\left(1-e^{-B_i}\right)\prod_{j=1}^{i-1} e^{-B_j}}} + T_n\underline{\underline{\prod_{j=1}^{n-1} e^{-B_j}}} \tag{3.4}$$

where the first, second and third term of the right-hand side represents the combination of the 1st, the 2nd to the nth layer (e.g., i th represents the layers in the middle, while nth represents the last layer). When the first layer has been fixed in field sites, the accuracy Equations (3.3) and (3.4) can achieve in estimating T_{eff} depends on the determination of sampling depth (intervals) Δx_i (i for i th layer). Figure 3.1 illustrates the subscripts related to Equation (3.3) and (3.4).

In this chapter, the features of B and how B is related to Δx will be discussed in Section 3.2. Section 3.3 will discuss two aspects regarding the application of Lv's scheme: (1) the assessment of existing sites in the Maqu Network regarding their representativeness for calculating T_{eff}; (2) how to determine the optimal mounting depth for the second layer when provided with a fixed first layer. The proposed approach is validated using observations and model outputs. A discussion and conclusion are found in Section 3.4.

3.2 Methodology and Data

In Section 3.2.1, a series of concepts for evaluating T_{eff} from Lv's multi-layer scheme will be established. A mathematical derivation of an optimal mounting depth from Lv's multi-layer scheme will be presented in Section 3.2.2. An evaluation method inferred from these concepts will be applied to the SM/ST field observation at Maqu Network in Section 3.3.1. Since the field observation contains a maximum of six layers, Noah simulation data will be a supplement to involve more layers (37 layers). The simulated true T_{eff} is obtained by using Lv's multi-layer scheme. Then, all two-layer combinations will be presented to generate T_{eff} with Lv's two-layer scheme. The theory derived in Section 3.3.1 will be checked in Section 3.3.2.

3.2.1 Characteristics of Parameter B

Lv's scheme uses an exponential function to distribute the weight among different layers (see Equation (3.4)). The only parameter in this scheme is B. A series of extended concepts used to analyze the characteristics B are listed in Table 3.1.

Table 3.1. The mathematical details regarding the concepts mentioned in this chapter.

Name	The First Layer	Middle Layers	The Deepest Layer
B	$B_i = \Delta x_i \cdot \frac{4\pi}{\lambda} \cdot \frac{\varepsilon''}{2\sqrt{\varepsilon'}}$, Δx_i is the physical depth interval as in Figure 3.1. Soil moisture/temperature are from the i th layer as well.		
Residual (R)	e^{-B_1}	$\prod_{j=1}^{i} e^{-B_j}$	$\prod_{j=1}^{n} e^{-B_j}$
Weight Function	$1-e^{-B_1}$	$\left(1-e^{-B_i}\right)\prod_{j=1}^{i-1} e^{-B_j}$	$\prod_{j=1}^{n-1} e^{-B_j}$

For the assessment of the Maqu Network and the determination of optimal mounting depth/combinations, the multilayer scheme will be deployed. When excluding both the top and bottom layers in the multilayer model, the in-between layers (the i th layer) share the common expression: $T_i\left(1-e^{-B_i}\right)\prod_{j=1}^{i-1} e^{-B_j}$, with $\left(1-e^{-B_i}\right)\prod_{j=1}^{i-1} e^{-B_j}$ called the weight function (double underlined in Equation (3.4)). Thus, the weight function is divided into the term $\left(1-e^{-B_i}\right)$ dealing with B at the i th layer, and the term $\prod_{j=1}^{i-1} e^{-B_j}$, which determines how much the i th layer contributes to T_{eff}. In other words, if the $(i+1)$th layer exists, whatever the soil temperature at the $(i+1)$th layer is, the soil temperature at the $(i+1)$th layer has to be multiplied by $\prod_{j=1}^{i} e^{-B_j}$. Hence, $\prod_{j=1}^{i} e^{-B_j}$ can be called the residual weight (single–underline in Equation (3.4)) of the i th layer. With these concepts in mind, it is possible to estimate the potential contributions by different layers when calculating T_{eff}, as discussed in Section 3.1.

In the following, Lv's scheme will be used to derive the optimal mounting depth. In Equation (3.3), T_1 depicts the approximation of the layer-mean soil temperature of the first layer, with $1-e^{-B_1}$ its weight in the calculation of T_{eff}. The same can be said for the second layer, for T_2 and e^{-B_1}. The result will only be optimal (exact T_{eff} estimates) if the following conditions are met:

(1) T_1 matches the layer-averaged soil temperature integrated from the surface to the sampling depth Δx, which is used for calculating $1-e^{-B_1}$ (see Equation (3.3));

(2) T_2 matches the layer-averaged soil temperature integrated from the sampling depth Δx to infinity, as in Equation (3.2).

Table 3.2. The explanation of the parameters used in determining the optimal mounting depths.

B	Δx	**Soil Moisture**	**Soil Temperature**
B_{1s}	Δx_{1s}, the mounting depths of sensors in the first layer	The first layer samples	The first layer samples
B_1	Δx, deduced from $1-e^{-B_1}=e^{-B_{1s}}B_1$	Layer-averaged (1st layer)	Layer-averaged (1st layer)
B_{2s}	Δx_{2s}, the mounting depths of sensors in the second layer	The second layer samples	The second layer samples
B_2	Not necessarily defined	Not necessarily defined	Not necessarily defined

When both conditions are met, the weights calculated by Equation (3.3) are exact for the first and second layer, regarding calculating T_{eff}. The representative depth for which temperature (i.e., depth intervals) are defined in numerical model outputs; for instance, 0 to 7 cm for the first layer, 7 to 28 cm for the second layer, 28 to 100 cm for the third layer, and 100 to 289 cm for the bottom layer in ERA-interim reanalysis data. The same concept exists for observation data like the Maqu Network, but the measurement is at a certain depth, not the representable average temperature. The depths interval a SM/ST sensor could represent is critical, considering Conditions 1 and 2.

Table 3.2 explains the definition of parameters used in determining the optimal mounting depths. To keep consistent with the B_1 in Equation (3.3), B_{1s} and B_{2s} are proposed to stand for the corresponding B values at the mounting depth of Δx_{1s} and Δx_{2s}, where the sensors are actually installed.

3.2.2 Optimal Mounting Depth

Considering the integral exponential function $\int e^{-x}dx=1-e^{-x}$, it could be deduced that for each layer in the soil profile dx, its weight should be e^{-B}. To satisfy Condition 1, the first layer $e^{-B_{1s}}$ is supposed to be the mean value of $e^{B}\Big|_0^{B_1}$, e.g., $e^{-B_{1s}}=\frac{1}{B_1}\int_0^{B_1}e^{-B}dB=\frac{1}{B_1}\left(1-e^{-B_1}\right)$. This demonstrates that the weight $e^{-B_{1s}}$, calculated by using SM/ST at sampling depth Δx_{1s}, should match the layer-averaged e^{-B}. Here e^{-B_1} should be calculated by using the layer-averaged SM/ST with a layer thickness of Δx.

For the second layer, to satisfy Condition 2, T_2 is assumed to match the layer-averaged soil temperature integrated from the interval $[B_1,\infty]$. The infinite is usually represented numerically by using a cutting-off error with a finite number (in this case: $\infty\approx B_2+cutting\_off\_error$). Consequently, T_2 is here defined as the layer-averaged ST between $[B_1,B_2]$ where $B_1<B_{2s}<B_2$. With a cutting-off error B_2, the First

Mean Value Theorem for Integration [128] can be applied to prove that there must be a value of B_{2s} that satisfies Condition 2. In fact, B_2 can be numerically defined without necessarily being used in the calculation of the subsequent derivation with the math introduced below.

The above implies that the weight $e^{-B_{2s}}$ calculated by using the SM/ST at the sampling depth Δx_{2s} should match the layer-averaged e^{-B} (e.g., $e^{-B_{2s}} = \frac{1}{(B_2 - B_1)} \int_{B_1}^{B_2} e^{-B} dB \approx \frac{1}{(B_2 - B_1)} \int_{B_1}^{\infty} e^{-B} dB$). Therefore, for the two-layer scheme, the total weight is the sum of

$$\begin{cases} 1 - e^{-B_1} = e^{-B_{1s}} B_1 \\ e^{-B_1} = e^{-B_{2s}} (B_2 - B_1) \end{cases} \tag{3.5}$$

Since B_{1s} is determined by field observation (e.g., the first SM/ST sensor below the soil surface), Equation (3.5) contains three unknowns: B_1; B_2 and B_{2s}, but with two formulas. With the present B_{1s} known, B_1 can be calculated by using the first expression in Equation (3.5). There are two remaining parameters, B_2 and B_{2s}, that need to be solved in Equation (3.5).

To meet Condition 2, T_2 should match the layer-averaged ST for the second layer, which means T_2 is equal to the ST at the sampling depth Δx_{2s} (see Table 3.2) because at this sampling depth the weight $e^{-B_{2s}}$ is representative for the second layer. On the other hand, to be representative of the second layer, the B_{2s} (corresponding to Δx_{2s}, Table 3.2) must be located between B_1 and B_2. Since the First Mean Value Theorem for Integration is defined within a closed interval $[B_1, B_2]$, an optimal mounting depth of Δx_{2s} (e.g., at $[B_1, \infty]$) has to be determined to enable its layer representativeness. The determination of an optimal mounting depth can be achieved by using the characteristic ratio $\frac{B_2 - B_{2s}}{B_{2s} - B_1}$ for the second layer. Expanding this characteristic ratio, considering Equation (3.5), leads to:

$$\begin{aligned} \frac{B_2 - B_{2s}}{B_{2s} - B_1} &= \frac{e^{-B_1} / e^{-B_{2s}} - (B_{2s} - B_1)}{B_{2s} - B_1} \\ &= \frac{e^{B_{2s} - B_1} - (B_{2s} - B_1)}{B_{2s} - B_1} \end{aligned} \tag{3.6}$$

The form of the function with this characteristic ratio is $f(x) = \frac{e^x - x}{x}$. Therefore, mathematically, to obtain an optimal characteristic ratio, the first order derivative of $f(x)$ needs to be equal to zero. There is also a physical meaning: in Figure 3.2a, as will be discussed, to meet Condition 1 and 2, the pink area has to be made equal to the purple area (i.e., for the first layer), and the green area to the grey area (i.e., for the

second layer). As can be seen, if B_{2s} is situated closer to either B_1 or B_2, the weight of $e^{-B_{s2}}$ will not represent the second layer. Under the precondition that the annual averaged soil temperature tends to be homogeneous throughout the soil profile [129-131], to enable the layer representativeness of B_{2s}, the difference between $B_2 - B_{2s}$ and $B_{2s} - B_1$ has to be made as small as possible. Meanwhile, to enable the grey and the green area to be equal in size for the second layer in Figure 3.2a, the ratio should not be smaller than a constant, considering the shape of the $f(x) = \frac{e^x - x}{x}$ curve. To find a solution for $f(x)$ that reduces the ratio as much as possible actually means the first order derivative of $f(x)$ should be equal to zero. This leads to $x = 1$, for the current function form, which means

$$B_{2s} - B_1 = 1 \tag{3.7}$$

In this way, B_{2s} does not need to be defined exactly (Table 3.2), with the cost of causing a cutting-off error. However, due to the infinite form of Equation (3.2), the cutting-off error determined by the approach indicated above cannot be 0 but can be infinitely approaching 0. With the relation obtained in Equation (3.7), Equation (3.5) may be rewritten as,

$$\begin{cases} 1 - e^{-B_1} = e^{-B_{1s}} B_1 \\ B_{2s} = B_1 + 1 \end{cases} \tag{3.8}$$

where $B_{1s} = \Delta x_{1s} \cdot \frac{4\pi}{\lambda} \cdot \frac{\varepsilon''}{2\sqrt{\varepsilon'}}$ is computed by the SM/ST data collected at the first layer in the field experiment ($\Delta x_{1s} = 0.05\,m$ for the Maqu Network). With Equation (3.8), the determination of B_1 is easy in the first expression once B_{1s} is known. This then naturally leads to the determination of B_{2s} in the second expression.

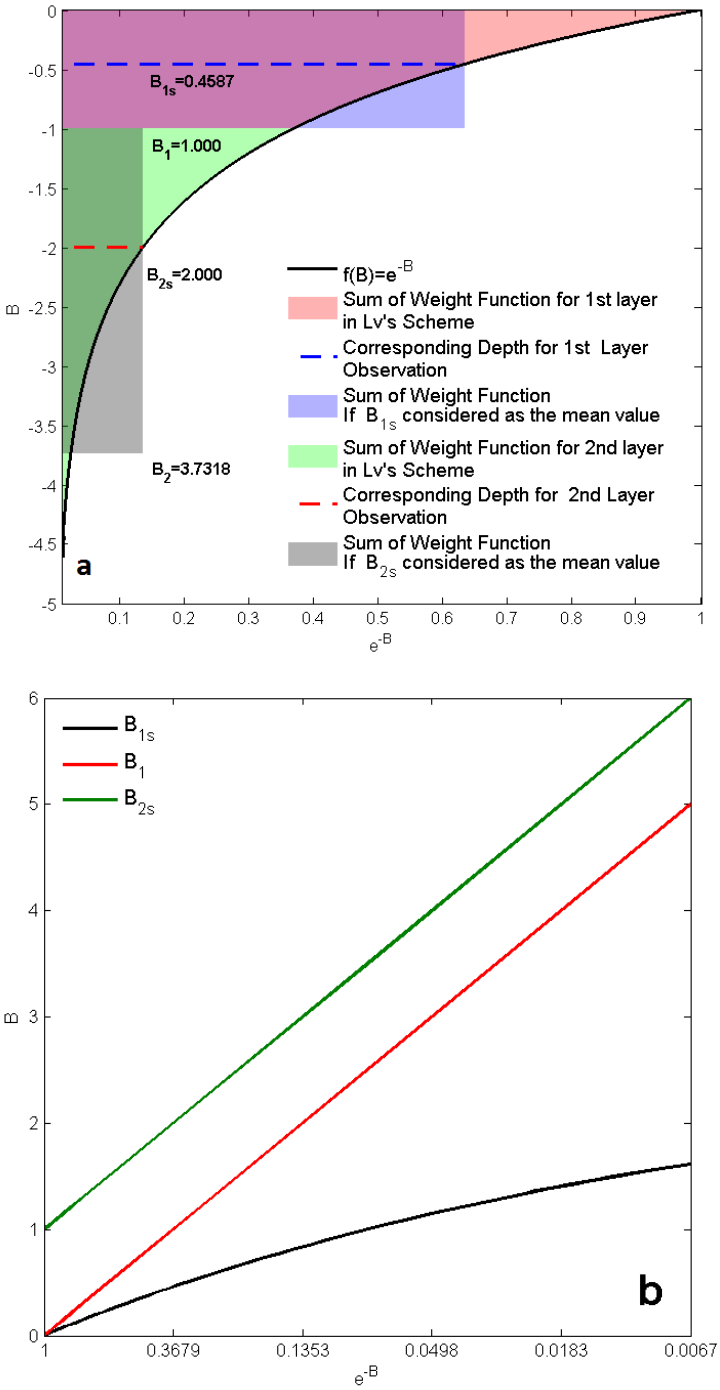

Figure 3.2. (a) Schematic diagram of sampling depth for $\lambda = 21\,cm$. B_{1s} and B_{2s} correspond to the physical depths where the sensors shall be installed if $B_1 = 1$; (b) The extension of Figure 3.2a to any B_1 values. B_{1s} and B_{2s} are reference lines increasing with B_1

Figure 3.2a explains the concept of Equation (3.8) in a schematic diagram, by showing the relationship between the parameter B and the residual e^{-B} in a two-layer T_{eff} model. If the present value

$B_1 = 1$ is used, then B_{1s} and B_{2s} can be derived by using Equation (3.8). For each B value, a corresponding depth can be calculated by $B_i = \Delta x_i \cdot \frac{4\pi}{\lambda} \cdot \frac{\varepsilon''}{2\sqrt{\varepsilon'}}$, where SM/ST is measured for each layer at the sampling depth of Δx_i. Therefore, the explanation of physical depth Δx is tied up with B. This relationship may be expressed as $B = g(\Delta x)$. According to Equation (3.8), if the first layer sensor is installed at Δx_{1s}, this will correspond with B_{1s}, while the depth interval Δx should correspond with B_1 (e.g., layer-averaged). Then, to meet Condition 1, the pink area should be equal to the purple area in Figure 3.2a.

After determining $B_1(\Delta x)$, the remaining area (i.e., the green area) represents the weight given to the second layer, from which $B_{2s}(\Delta x_{2s})$ can be inferred. The ratio (e.g., B_1/B_{1s}, B_{2s}/B_{1s}) obtained by Equation (3.8) can be used to infer the optimal mounting depth if the thickness of the first layer is fixed. For instance, if B_{1s} obtained from this ratio is 0.46, which corresponds to a sampling depth of Δx_{1s}, then B_1 is assumed to equal 1. Furthermore, B_{2s} should equal 2, based on Equation (3.8), and this corresponds to another sampling depth, Δx_{2s}. Figure 3.2a and Equation (3.8) both indicate the capability of Lv's scheme in identifying the optimal mounting depth. They are the simplified form of the multilayer model described in Equation (3.4).

Figure 3.2b mathematically shows B_{1s}, B_1 and B_{2s} distributed in a "$B\ vs.\ e^{-B}$" domain, based on Equation (3.8). As discussed above, with a sensor positioned at a certain mounting depth, the "$B\ vs.\ e^{-B}$" domain can help to understand how the weight of the soil layer at that depth contributes to the calculation of T_{eff}. By assuming B_{1s} =0, 1, 2, we can obtain the black line in Figure 3.2b. Furthermore, B_1 is a function of B_{1s} ($B_1 = f(B_{1s})$) and B_{2s} is a function of B_1. Therefore, with B_{1s} varying, B_1 and B_{2s} form curves, as shown in Figure 3.2b. It should be noted that the *y*-axis in Figure 3.2b indicates a special case: if there is only one layer left to represent the whole soil volume, then $B_{2s} = 1$ is the optimal option. In this case, the real optimal mounting depth (Δx_{2s}) could be inferred from $B_{2s} = 1 = \Delta x_{2s} \cdot \frac{4\pi}{\lambda} \cdot \frac{\varepsilon''}{2\sqrt{\varepsilon'}}$, considering the SM/ST conditions for dielectric constant. It is coincidental with the concept of penetration depth or what is called the temperature sensing depth as that depth satisfies $1/e$ of Equation (3.2) [132, 133]. The distribution of curves in Figure 3.2b is generic, and the curves are characteristic and derived from Equation (3.8). Figure 3.2a can be seen as a single vertical cross-section of Figure 3.2b. With Figure 3.2b, it is possible to identify the optimal mounting depth Δx_i (i = 1, 2), as long as B_{1s} and B_1 computed from specified ST/SM profiles align with the black and the green reference lines, respectively. As long as computed B_{1s} and B_{2s} meet the reference lines, Equation (3.8) is satisfied. To sum up, the basic steps in determining the optimal sampling depth could be:

(1) Using SM/ST observation at first layer (Δx_1) to calculate B_{1s} with $B_i = \Delta x_i \cdot \frac{4\pi}{\lambda} \cdot \frac{\varepsilon''}{2\sqrt{\varepsilon'}}$;

(2) Using B_{1s} to calculate B_1 and B_{2s} with Equation (3.8); B_{2s}

(3) Determining the optimal sampling depth for the second layer with $B_i = \Delta x_i \cdot \frac{4\pi}{\lambda} \cdot \frac{\varepsilon''}{2\sqrt{\varepsilon'}}$ again.

If a network already exists whose sensors are installed at several depths (Δx_i), then select a two-layer combination and calculate its B_{1s} and B_{2s}. The pair B_{1s} of and B_{2s} that fits Equation (3.8) is the optimal sampling depth. The application of Figure 3.2b to an existing network (Maqu Network) will be discussed in Section 3.3.2.

3.2.3 The Maqu Network

In 2008, a soil moisture monitoring network was set up at Maqu [134, 135]. Maqu is located in the source region of the Yellow River at the east margin of the Tibetan Plateau. The average elevation is around 3300 m above sea level. The vegetation consists of alpine shrublands and meadows, with grasses less than 1 meter in height with roots extending tens of centimeters in depth. An accumulated humus layer of around 10 cm is mixed with the soil. Shrubs and trees are scarce in this region, while desert dunes sometimes appear along the river. The network includes 20 sites with a variety of terrain and soil textures, such as silt loam and sandy loam. The observation depth is set to 5 cm/10 cm for most sites, but a few sites have enhanced layer settings of 20 cm, 40 cm, and 80 cm. Three of these sites, C01, N01, and N02, are relatively close to each other, i.e., within 200 m. There is also a boundary layer meteorological tower at C01, which takes its own SM/ST measurements; this station is hereafter called the center station [116]. The layer settings for the center station are 5 cm, 10 cm, 20 cm, 40 cm, 80 cm and 160 cm, with an additional infrared sensor for the skin temperature. Since its establishment, the Maqu Network has provided accurate soil parameters for retrieving soil moisture data from satellites at the L-band [115-117, 136]. The time series of SM/ST at the center station were collected from May 2009 to April 2010. To avoid introducing the additional complexity of frozen soil, the calculation in Section 3.2 is based only on the time series where ST > 0. Additionally, to obtain time series via the Wilheit's scheme, the NOAH Land surface model [134] was adopted to generate ST/SM profiles with 37 layers (0 to 500 cm) between 12 and 28 June 2010. The driving force including radiation, precipitating, wind and surface temperature are collected from the Maqu central station.

3.3 Results

3.3.1 Evaluation of Installation Configuration

The spatial resolution of passive microwave radiometers on satellite platforms is coarse compared to an area represented by a single SM/ST site. For instance, SMOS produces brightness temperature observations with a resolution of about 40 km on average [11]. For the whole region covered by the Maqu Network, T_{eff} calculated from a single site is not representative enough considering the degree of spatial

variability in soil moisture and texture. It is common practice to take the average arithmetic value for all sites in the network and compare this to the brightness temperature observation [53, 116]. In this section, the values (i.e., weights) for different layers contributing to T_{eff} and thus also T_B at the central station are calculated using Equation (3.4). The same method can be applied over the whole network. This section will evaluate the value of a single station for comparison with selected estimates, beginning with the central station.

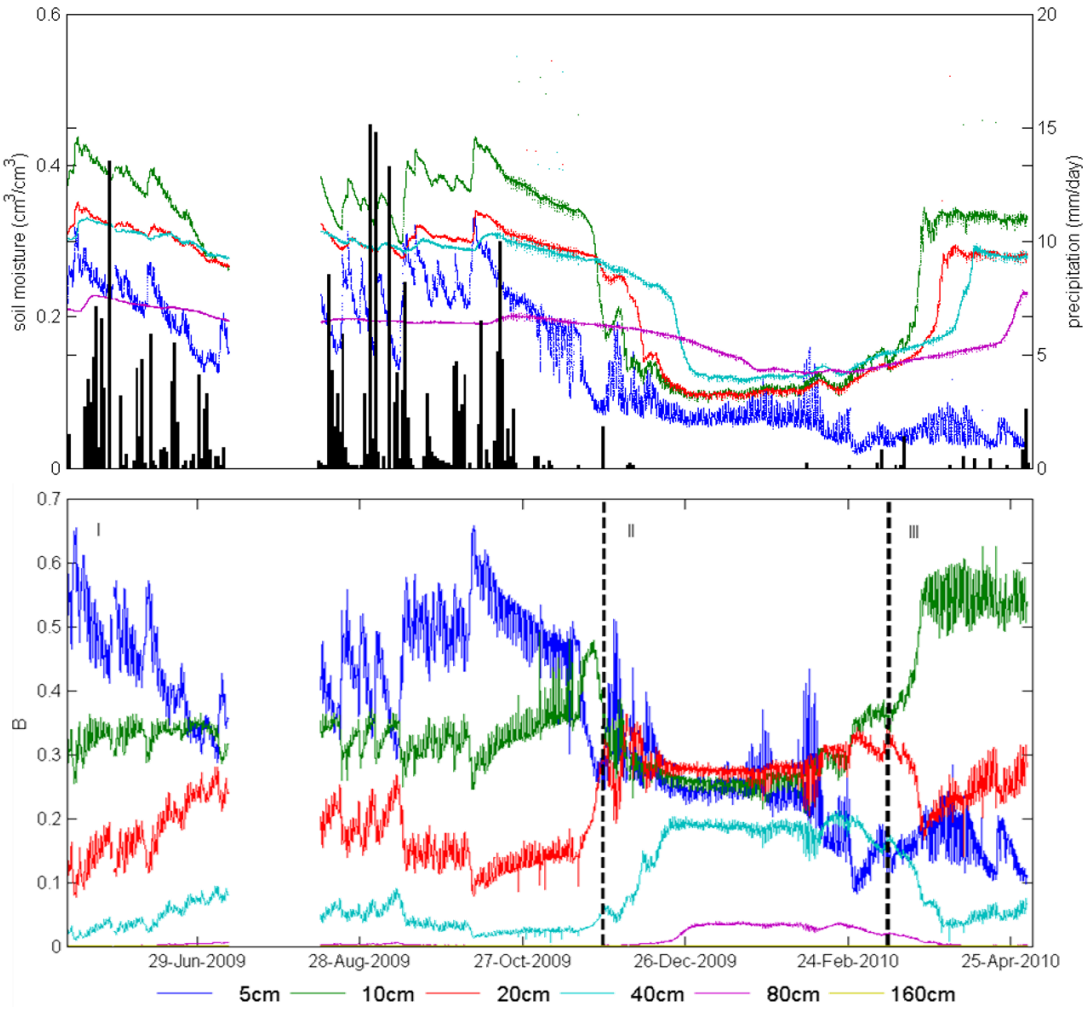

Figure 3.3. Soil moisture and rainfall time series at the center station of the Maqu network (**upper** panel); B values in Equation (3.4) for the six layers using Lv's multilayer scheme (**bottom** panel). The time series is divided into three periods: April 2009–mid November 2009 (Period I); mid November 2009–March, 2010 (Period II); April, 2010 (Period III). The blank in July is due to data missing.

Figure 3.3 shows the time series for values (e.g., the contribution of weight, Table 3.1) at different mounting depths (or layers) at the center station, divided into three periods: April to November 2009; November 2009 to February 2010; and the period after February 2010. The curves (e.g., for the upper layers

≤20 cm) for the second period can be explained by the soil being frozen (when soil temperature is below 0 °C). Frozen soil, no matter to the solid water fraction, has a similar dielectric constant compared to dry soil. It makes the SM/ST profile homogenous, which leads to similar B values for the upper layers (≤40 cm). Usually, the upper layer contributes most to T_{eff}, as seen in the first period. However, this is not the case in the third period, when the contribution from the 10 cm layer is dominant. This implies that a two-layer model, which considers only the 5 cm and 160 cm layers, for instance, may lead to significant errors (e.g., loss of signal from the 10 cm layer).

As expected, B varies throughout the seasons [127]. Normally due to soil moisture variations. Several rainfall events increased soil moisture at 5 cm and subsequently the B values for that layer. The other layers (10, 20, 40, 80, and 160 cm) may even have opposite phases. The B values of the 5 cm and the 10 cm layer have opposing patterns (as in Period I and III in Figure 3.3). The reduction of B at 5 cm, for Period III, is caused by surface dryness due to lack of rainfall while the mean soil moisture content at 10 cm at that time is around 0.35 m^3/m^3.

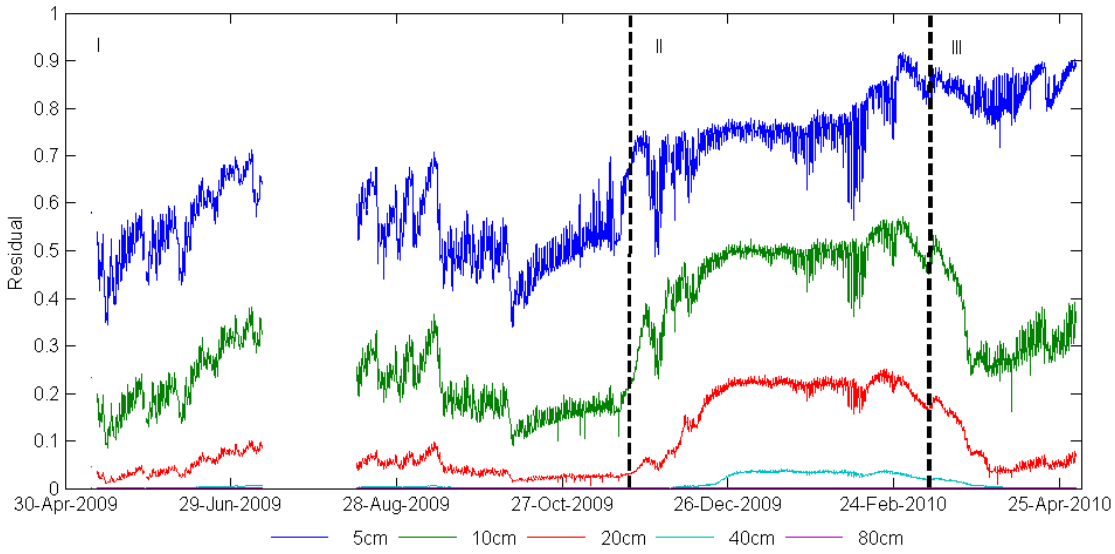

Figure 3.4. The residual (see Table 3.1) for each layer, where residual refers to the percentage of T_{eff} signals from deeper layers contributing to the result, as the land surface is reached.

Figure 3.4 indicates the time series of the residual (see definition in Table 3.1) for all layers. During Period I about 50% of the weight comes from the soil layer 0 to 5 cm, while the other 50% originate from the soil layers below 5 cm. The soil layer at 10 cm contributes about 30% of the weight. The remaining 20% comes from the soil layers below 10 cm. Thus, the soil layers at 5 cm and 10 cm combined will contribute about 80% of the signal when estimating T_{eff} at the central station. If we include more layers in the calculation, more weight will be included. For example, if information from the 20 cm layer is also included, only 5% of weight from the soil layers beneath the 20 cm layer will be considered.

During Period II, the soil is frozen, which makes the soil column vertically homogeneous. The dielectric behavior of frozen soil is similar to dry soil; hence, the penetrating depth increases, which means that the microwave emission reaching the surface may come from deeper soil layers, implying an increased residual for each soil layer. In Period II all residuals are higher compared to other periods.

During Period III, the weight from the first layer (i.e., 5 cm) is greatly reduced, and the 10 cm layer contributes more than 60%. Thus, by taking 5 cm as the corresponding depth in the first layer, the residual of weight is greatly increased (e.g., to be about 80%, blue line in Figure 3.4). On the other hand, the residual of weight for the 10 cm layer drops dramatically, to less than 30%, since the inclusion of the 10 cm increases the upper layer's contribution in the calculation of T_{eff} .

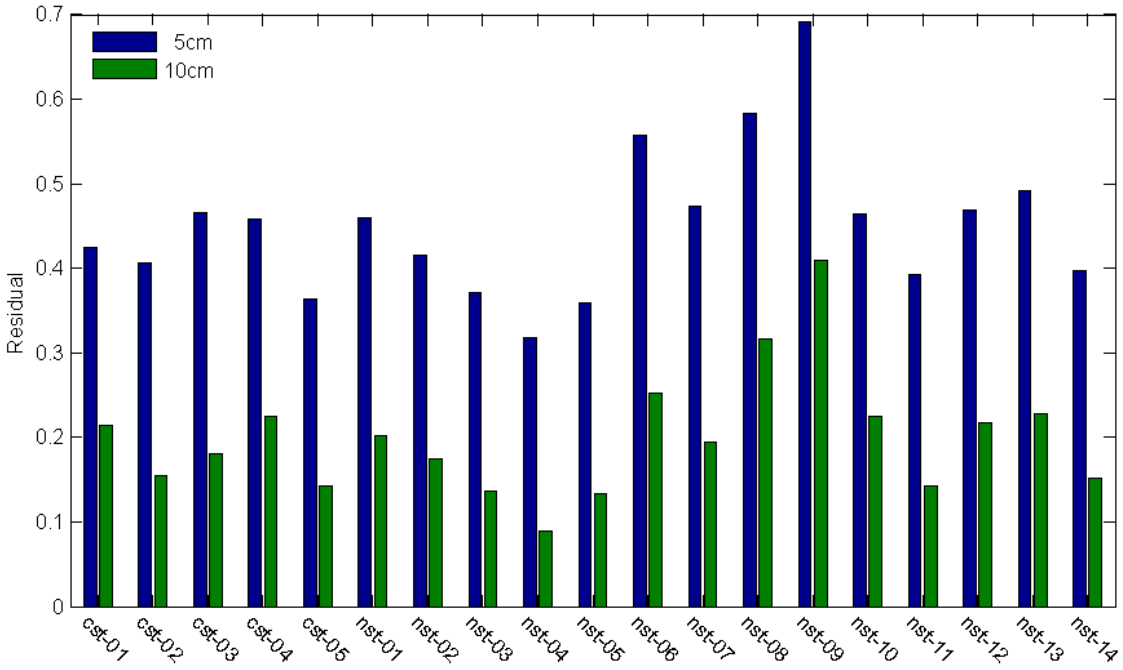

Figure 3.5. The residual for each site for the first two layers as shown in Figure 3.4.

Thus, by considering only the weight contributions from the combination of 5 cm and 10 cm (Figures 3.3 and 3.4) is insufficient to T_{eff} estimates, as the total represented weight will be only about 80%. If the 20 cm weight is also taken into account, the total weight will be around 90%. Thus, the calculation of parameter *B* or the residual weight can be used to assess the representativeness of each site in the Maqu Network when estimating T_{eff} .

To best estimate T_{eff} , the physical mounting depth should be designed to minimize the residual. When the same mounting depth is used throughout the Maqu Network, with $\Delta x_1 = 5\ cm$ for the first layer and $\Delta x_2 = 10\ cm$ for the second layer residuals vary largely (Figure 3.5). Smaller residuals indicate smaller errors for estimating T_{eff} . Obviously, NST-04 site is relatively reliable, with a contribution form lower than

10 cm is less than 10%. Thus with observation of 5 cm and 10 cm, the NST-04 site can be used to calculate T_{eff} with high accuracy compared to other sites in the Maqu Network. The contrary is found for the NST-09 site since the residual weight from the other soil layers can be about 40. Therefore, the NST-09 site should be given less credit when composing a spatial averages. There are many ways to choose representative sites based on statistics like the Optimal Selection of Alteration Information Extraction Method. However, for the L-band, the pixel could be tens of kilometers, which means that all sites within the Maqu Networks make a contribution to the final signal detected by SMOS/SMAP. None of the sites should be simply removed or given full credit (weight number = 1) because of the complexity of soil moisture profiles, etc. and the uncertainty (residual) should be related to the weight when averaging. To quantify this credit C, the use of the normalized residual signal is suggested, to be expressed as:

$$C_i = 1 - \frac{R_i - R_{\min}}{R_{\max} - R_{\min}} \tag{3.9}$$

where i represents the i th site, i = 1 to n (i.e., the total number of sites in a network); R_{max} and R_{min} represent the maximum and minimum residual among all sites. Then, for the Maqu Network, an averaged value of T_{eff} could be given by

$$T_{eff} = \frac{\sum_{i=1}^{n} T_{effi} \times C_i}{\sum_{i=1}^{n} C_i} \tag{3.10}$$

where T_{eff} is calculated at the i th site with the 5 cm and 10 cm installation configuration. None of the sites in the Maqu Network has soil moisture less than 0.2, while the larger residuals imply a deficiency of instrument installation in describing T_{eff}. Without Equation (3.9) and Equation (3.10), at least 20% of T_{eff} signals on average would lose at the Maqu Network with this assumed sensor installation configuration (5 cm & 10 cm). This approach is generic and can be applied to other observation networks to estimate their representativeness in estimating T_{eff}.

Theoretically, according to Equation (3.2), T_{eff} will vary daily and seasonally with the SM/ST profiles and the optimal mounting depths will vary as well. For most of the sites in the Maqu Network, however, 5 cm/10 cm is the default installation setting for measuring SM/ST. There is no fixed depth configuration that can accommodate all variations in SM/ST throughout the year, but we can investigate the optimal mounting depth by finding the optimal combination of sensor installations that will represent the mean SM/ST for that site. The center station will be used as an example of such an investigation. The same procedure can then be applied across the whole Maqu Network.

3.3.2 Test of the Optimal Mounting Depth

This section describes how to determine the optimal mounting depth for the two-layer approach. Based on this discussion, the current installation configuration at the Maqu Network can be enhanced by adding sensors to the current configuration. The proposed approach is sketched in Figure 3.6. We show two examples: for the first example we chose $x_{1s} = 5$ cm for the second example we chose $x_{1s} = 10$ cm. B_1 is then calculated via Equation (3.8) and the depth for the second layer determined (i.e., Δx_{2s}). Two columns are shown to present two different cases of study: (1) For, $x_{1s} = 5$ cm $B_{5\,cm} = 0.267$ (y-axis) and the 2nd layer may be 20 cm/40 cm/80 cm/160 cm to be the second layer; 10 cm is not shown because $\Delta x > 10$ cm (Table 3.2) when 5 cm is the first layer; (2) For $x_{1s} = 10$ cm, $B_{0.1m} = 1.268$ and the 2nd layer may be 40 cm/80 cm/160 cm; 20 cm is not included for the same reason noted above. With the same technique, we acquired the positions of all other layers (indicated by asterisks with the depth information). Not all layers deeper than the assumed first layer could be the second layer because according to Equation (3.8), Δx may be larger than the supposed second layer. For instance, when 5 cm is the first layer, $\Delta x = 11.8\,cm$ which is bigger than 10 cm. It is not necessary to take 10 cm into consideration since most of its information could be represented by 5 cm. This approach has been utilized to plot Figure 3.2b. The existing sites already have a fixed Δx_1 (therefore a fixed B_{1s}) for the first layer. Thus, B_1 can be easily calculated here using Equation (3.8). The core concept is that the choice of depth combination (e.g., 5 cm and 10 cm, or 5 cm and 20 cm, etc.) reduces the residual to a minimum (e.g., ideally = 0) under the constraint of Equation (3.8). The data collected at the center station contain six layers of SM/ST observations, which will be used to show which two of these layers can best estimate T_{eff}. The similar approach can be applied at other sites in the Maqu Network.

Table 3.3. Correlation coefficient and RMSE with available six-layer soil moisture/soil temperature profiles. The selected two layers are illustrated in Configuration.

Configuration	**5 cm/ 10 cm**	**5 cm/ 20 cm**	**5 cm/ 40 cm**	**5 cm/ 80 cm**	**5 cm/ 160 cm**	**10 cm/ 20 cm**	**10 cm/ 40 cm**	**10 cm/ 80 cm**
Residual (R)	0.311	0.074	0.039	0	~	0.034	0.002	≈0
Weight function for the first layer $1-e^{-B_1}$	0.496	0.496	0.496	0.496	0.496	0.950	0.950	0.950
$B_{2s} - B_1$	−0.067	0.943	2.907	5.367	10.442	−0.610	1.374	4.168
Correlation Coefficient	0.99	0.99	0.99	0.97	0.95	0.98	0.98	0.98
RMSE(K)	0.93	0.44	1.12	1.77	2.46	1.09	1.02	1.05

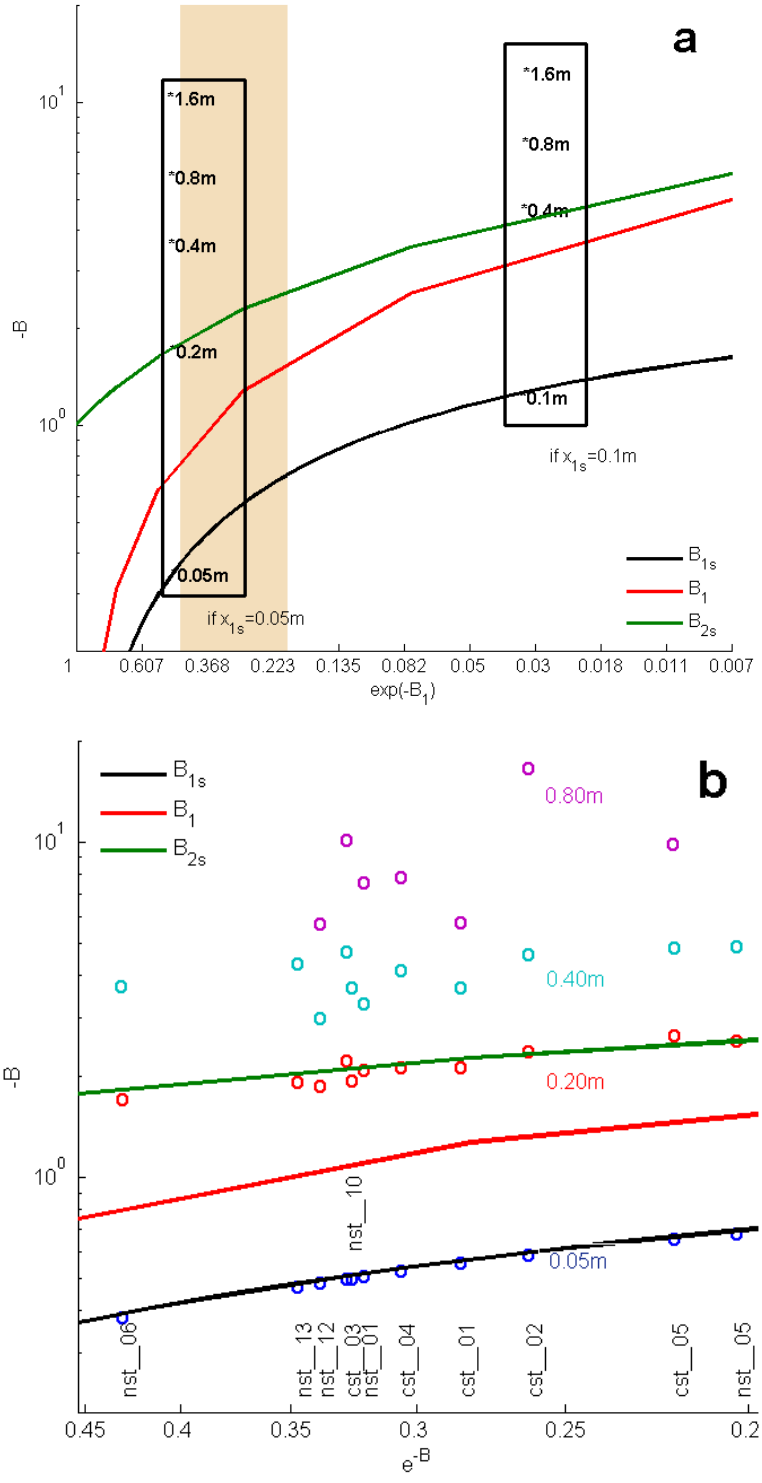

Figure 3.6. (a) An illustration of the ratios for $B_{1s}/B_1/B_{2s}$ at the center station when 5 cm and 10 cm are taken as the first layer in the Maqu Network. The shaded area depicts the e^{-B} range used for Figure 3.6b; (b) The other sites in the Maqu Network with 5 cm as the first layer and assuming 20 cm/40 cm/80 cm to be the second layer. 10 cm is not included for the same reason shown in the left column of Figure 3.6a.

According to Equation (3.8), based on the installation depth and the associated mean SM/ST, the sensor installation configuration can be mapped on the "$B\ vs\ e^{-B}$" domain as well (Figure 3.6). The observations at 5 cm, 10 cm, 20 cm, 40 cm, 80 cm, and 160 cm depth at the center station were plotted in this way and pooled in Figure 3.6a. The B_1 curve (corresponding to Δx) divides the soil column into two parts. The curve indicates that the -B (y-axis) and residual for the second layer e^{-B} (x-axis) can be achieved if a sensor is installed at Δx_{1s}, and the B_{2s} curve indicates -B for Δx_{2s} while the first layer determines e^{-B}. Figure 3.2b shows that B_{1s}, B_1 and B_{2s} curves are derived directly from Equation (3.8), which is generic and independent of mounting depth and SM/ST information. This implies that if the sensor installation configuration is mapped in the "$B\ vs\ e^{-B}$" domain, it can have matching points with B_{1s} and B_{2s} curves. Then the corresponding installation configuration is. In other words, if the sensors can be installed at mounting depths corresponding to B_{1s} and B_{2s} lines, the residual calculated from such an installation configuration would be minimized and the mounting depths considered optimal. For the center station, two pairs of lines emerge (Figure 3.6a): 5 cm and 20 cm, as well as 10 cm and 40 cm. From Figure 3.6a it can be deduced that the second pair contributes less than 5% to T_{eff} calculation (x-axis, $e^{-B_1} < 0.05$). Therefore, the optimal mounting depths are 5 cm and 20 cm for the center station of the Maqu Network. The same strategy can be used at the other sites in the Maqu Network, which have sensors installed at 5 cm/10 cm/20 cm/40 cm or 5 cm/10 cm/20 cm/40 cm/80 cm (Figure 3.6b).

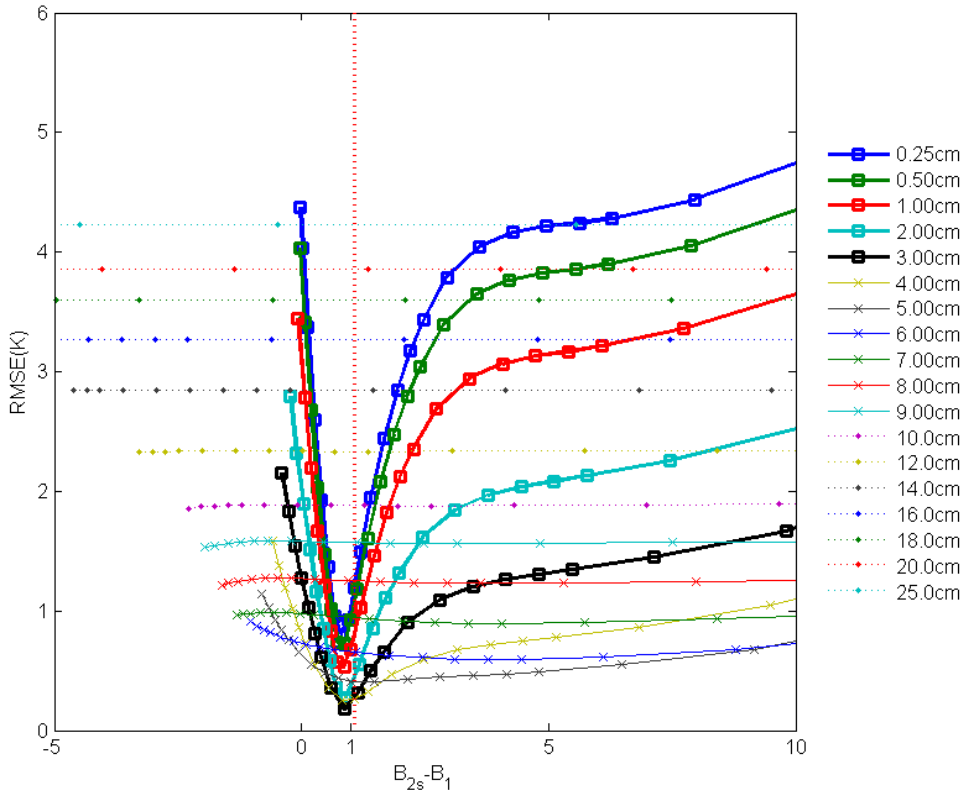

Figure 3.7. Test of the optimal mounting depth relationship with Noah 37 layers SM/ST simulation, 12–18 June 2010. The *X*-axis depicts $B_{2s} - B_1$ in accordance with Figure 3.2a during the computation, while the *Y*-axis is the root-mean-square-error (RMSE) against Wilheit's. The legend shows the first layer Δx_{1s}

$$\Delta x_{1s} \geq 25\,cm$$

Assuming Wilheit's scheme provides the true value of T_{eff} , Table 3.3 compares the possible combinations of layer pairs at the central station for calculating T_{eff} . Accordingly, the optimal mounting depths are 5 cm and 20 cm for estimating T_{eff} . The residual of the 5 cm and 10 cm combination is 0.311 which means 31.1% of T_{eff} signal beneath is unknown and implies potential uncertainty. The same information is deduced from Figures 3.4 and 3.5, where the residuals of all sites are compared. Most combinations arrive at a small residual, but only the 5 cm and 20 cm and the 10 cm and 40 cm combinations meet the $B_{2s} - B_1 = 1$ rule. It may be inferred that if the first layer is fixed at 10 cm, it is impossible to reach good agreement, since the representative term $\left(1 - e^{-B_1}\right)$ for the 10 cm layer is more than 95% with only 5% left for the second layer (i.e., the first layer is set too deep to represent the top layer information, which will lead to the underestimation of T_{eff}). The SM/ST information near the surface is overlapped by the 10 cm. In this case, the accuracy of output from Lv's scheme cannot be guaranteed. To summarize, the 5 cm and 20 cm combination have proven to be the best combination used as input for Equation (3.3).

To apply Wilheit's integral T_{eff} scheme, the minimum number of soil layers should be more than 20 [137]. Therefore, model investigation of SM/ST was done for the period from 12 to 18 June 2010 and was simulated using the NOAH Land-surface model. The total number of layers in NOAH is 37, from the soil surface to 5 m deep. Of these layers, 25 are within the upper 1 meter, which guarantees that an accurate T_{eff} will be acquired as the reference value by applying Wilheit's integral equation. The guaranteed means the vertical intensity is large enough for direct discretion to Wilheit's scheme, and 1 m is deep enough to capture all the layers contributing to T_{eff} . With these 37 layers, all combinations of two different layers are used to generate a T_{eff} time series by the method of exhaustion, and then the reference value is computed with RMSE (Figure 3.7). For instance, the blue line with squares stands for the case where the first layer is 0.25 cm. The first square from the left in this blue line is the combination of 0.25 and 0.5 cm; the second one is 0.25 and 1 cm, the third is 0.25 and 2 cm, etc. Each solid line with squares stands for a fixed first layer mounting depth and the dashed line with crosses for the RMSE variation along with the changing second layer mounting depth. It demonstrates that if the first mounting depth is shallow, the best T_{eff} estimation can only be achieved when $B_{2s} - B_1 = 1$ (for the lines from 0.25 cm to 5 cm in Figure 3.7). Conversely, RMSE will increase dramatically if the first mounting depth is very deep (regardless of the second mounting depth). In Figure 3.7, the optimal combination of mounting depths is 3 cm and 14 cm because it reaches the lowest RMSE (the black line with black square stands for 3 cm, and the 9th square counting from the left stands for 14 cm),. Figure 3.7 also proves that with the appropriately configured mounting depth T_{eff} , accuracy can be improved by at least several *Kelvin*. As indicated earlier, this combination is suitable only for the simulated period. To find the optimal mounting depth at the central station for the whole year, the annual mean SM/ST values from the existing mounting layer are needed. For the Maqu Network, the same principle seen in Equation (3.8) shows that the second mounting depth should be around 20 to 25 cm (with different dielectric mixing models) instead of the current 10 cm, with a mean SM = 0.138 cm^3/cm^3 and ST = 4.503 °C. In addition, the penetration depth/temperature sensing depth is also seen in Figure 3.7 because some lines (the lines with cross marks) could also reach nearly the minimum RMSE while B_1 (B_{1s}) is fixed. In these lines, RMSE does not increase with B_{2s} . It means $B_{1s} \approx 1$ and the first mounting depth already accounts for most of the weight for calculating T_{eff} .

3.4 Discussion

$B = \Delta x \cdot \frac{4\pi}{\lambda} \cdot \frac{\varepsilon''}{2\sqrt{\varepsilon'}}$ is the optical thickness of medium where radiation energy passing that layer is reduced to $1/e$ in accordance with the concept of the sensing or penetrating depth in remote sensing. In this case, Wilheit's integral T_{eff} scheme could be expressed as $T_{eff} = \int_0^\infty T(\tau) de^{-\tau}$, where $\tau = B$. The residual can be understood as the percentage of energy not captured by the ST/SM observation. Similarly, the

optimal mounting depth is a description of the mounting depths of two sensors in view of an optical thickness that corresponds to the microwave wavelength.

The main difficulty of residual estimation and optimal mounting depth is due in part to the definition of a parameter B which assumes the SM/ST is constant or has only a linear gradient within one fixed layer. This assumption is only an approximation, especially under extreme dry environment [138, 139]. The extent to which this assumption is satisfied depends on how many layers are involved. It is not surprising that in Figure 3.2b, if there is only one layer left then $B_{2s}=1$ declares the optimal mounting depth. The soil temperature observed at the soil temperature sensing depth equals T_{eff} if soil temperature changes linearly with depth.

Lv's scheme could be applied to frozen/thaw studies as well. As seen from Figure 3.3, B is strongly affected by the frozen/thaw events during the transfer period from Period I to II. However, the soil moisture detected by the sensors in the field becomes vertical uniform values when the soil temperature drops below 0 °C. The freeze/thaw signal can be captured by the B parameter, i.e., T_{eff} can capture the emission signal even during the freezing/thawing process. For the same reason, with a complex dielectric model that considers the water-ice mixing case, T_{eff} calculation is possible and may be further applied to T_B simulation at L-band over frozen ground.

3.5 Conclusions

As stated in the introduction, many networks exist around the world for calibrating and validating soil moisture retrieval from microwave satellite observations. The representativeness of these networks for calculating T_{eff} and in particular, they're in situ sensor configuration can be evaluated by the method developed in this chapter. The operational SMOS retrieval uses the ECMWF simulated global soil temperatures of the first layer and either the deepest or next-deepest layer, as the surface and deep temperature, respectively. Wigneron's two-layer T_{eff} scheme took this pair of soil temperatures as inputs with auxiliary information [40]. Similarly, the SMAP retrieval assumes a homogenous soil temperature and soil moisture profile at 6:00 A.M. and 6:00 P.M. and uses the surface skin temperature and soil temperature at 0–10 cm from the MERRA-Land model as the surface and deep temperature, respectively [140]. The arithmetical average of these two temperatures is taken as T_{eff}. This chapter illustrates how Lv's scheme is used for assessing the Maqu Network, in terms of identifying the optimal mounting depths for estimating T_{eff}. With better installation configurations, more accurate estimates of T_{eff} can be achieved and the soil moisture remote sensing product can be improved.

The main conclusions of this paper are: (1) Lv's scheme can be used to assess the quality of sites for estimating T_{eff} accurately. Section 3.1 showed that on average 20% of the T_{eff} and thus T_B signal is lost with the default 5 cm/10 cm installation; (2) The 5 cm/20 cm depth combination is optimal for the central

station of the Maqu Network. A similar approach may be applied to determine the optimal installation configuration for other monitoring networks, which can contribute to an improved validation [141] for satellite soil moisture products. By using the newly developed Lv's scheme, it will be feasible to determine which layer of soil moisture can be detected by the radiometer. This could be useful in improving the capacity of *in-situ* monitoring networks to calibrate and validate satellite soil moisture observations over different climate zones. It can also be used to derive the actual soil depths of the retrieved soil moisture and estimate the related errors, thus providing additional important information for applications.

Chapter

4 A Reappraisal of Global Soil Effective Temperature Schemes[3]

Abstract: T_{eff} is defined as the weighted temperature of the emitting layers, where the weighting involved depends on the soil moisture profile. In current passive microwave retrievals, T_{eff} is the assumed temperature, which multiplied by an emissivity gives the brightness temperature T_B, while the emissivity represents the soil layer from which the bulk signal of T_B originates. Traditionally, Effective Soil Temperature (T_{eff}) has been considered to be a secondary intermediate variable in microwave remote sensing. However, its impact on the retrieved is comparable to that of vegetation cover, soil surface roughness, and dielectric constant. In this chapter, we evaluate the suitability of various models for estimating T_{eff} using temperature and moisture profiles obtained from a land surface model. MERRA-Land (The Modern-Era Retrospective analysis for Research and Applications-Land) soil moisture profiles and temperature profiles are used to drive global T_{eff} datasets with single parameter schemes (e.g. the Beta Soil Moisture Active Passive, SMAP scheme), two-layer Choudhury's schemes (e.g. the current SMAP's scheme), two-layer Wigneron schemes (e.g. the current Soil Moisture and Ocean Salinity scheme, SMOS), and multilayer T_{eff} schemes (Lv's scheme). The results show that differences in T_{eff} from these schemes are usually less than 5 K. Especially Wigneron's and Lv's schemes give very similar comparable estimates (RMSD, root mean squared difference <1K). In exceptional cases (<1%), the RMSD between Choudhury's T_{eff} scheme and Lv's scheme can reach 5 K. The Beta SMAP T_{eff} has a difference of around 5K compared to Lv's scheme, which would lead to an emissivity difference of around 0.015, revealing in soil moisture errors of 0.06 m^3/m^3 . The most extreme emissivity differences are found in desert areas, at 42.5° incidence angle (the incidence angle used by the SMAP mission is about 40°).

Key Words: effective soil temperature, Soil Moisture and Ocean Salinity (SMOS), Soil Moisture Active Passive (SMAP), soil moisture

---

[3] This chapter is based on

Shaoning Lv, Yijian Zeng, Jun Wen, Zhongbo Su. 2016. A reappraisal of global soil effective temperature schemes. Remote Sensing of Environment, DOI: 10.1016/j.rse.2016.05.012

4.1 Introduction

Soil moisture is an essential variable in terrestrial water and energy budgets. Detailed knowledge of soil moisture would improve our current knowledge of hydrological processes and potentially seasonal climate forecasting [142-144]. Satellite microwave remote sensing is currently the only feasible method for estimating global soil moisture levels. However, the accuracy of this method depends heavily on the sensors and retrieval algorithms used. Remote sensing of soil moisture using microwaves assumes that the energy emitted from the soil is proportional to a thermodynamic temperature and soil emissivity [145]. The brightness temperature observed by satellite sensors is expressed accordingly as,

$$T_B = \varepsilon T_{eff} \tag{4.1}$$

where ε is an effective emissivity that depends on soil moisture via the soil dielectric constant and the vegetation conditions. T_{eff} is the effective soil temperature, which depends on soil moisture, wavelength, and temperature [73]. To obtain ε (and thus soil emissivity) from Equation (4.1), T_{eff} must be known a priori. T_{eff} used in current global operational processors for SMOS and SMAP is taken from the modeled soil temperature profiles. For example, the Soil Moisture and Ocean Salinity (SMOS) retrieval [40] uses ECMWF (European Centre for Medium-Range Weather Forecasting) land surface model data to estimate T_{eff}. Similarly, the Soil Moisture Active Passive (SMAP) retrieval uses MERRA-Land, which is a land data product of the Modern-Era Retrospective analysis for Research and Applications [140]. The rationale for deriving T_{eff} from model simulations is that the resultant errors will only have a significant impact for very dry soils [40].

More specifically, the operational SMOS retrieval uses ECMWF simulations of soil temperature for the top layer and for the deepest layer (or next to deepest layer) to estimate T_{eff}. Wigneron's two-layer T_{eff} scheme used these two soil temperatures as input, together with auxiliary information [40]. The previous Beta SMAP retrieval assumed a homogenous soil temperature and soil moisture profile at 6:00 a.m. and 6:00 p.m. local time. The surface skin temperature and soil temperature at 0-10 cm derived from the MERRA-Land model as the surface, and deep temperature, respectively [140], and the arithmetic average of both temperatures is taken as T_{eff}. Since September 2015, the SMAP team has updated its T_{eff} using Choudhury's two-layer scheme, because a more sophisticated model was required to accommodate non-uniform soil temperature profiles [44].

The use of soil temperatures from various layers and models used for SMOS and SMAP lead to differences in the values of T_{eff}. Recent investigations by Lv et al. (2014) indicate that the use of different sampling (model) depths for estimating T_{eff} could result in large deviation (around 7 K at Maqu Network [117]). This uncertainty ultimately affects the final soil moisture product. One study [146] reported that, in

extreme cases, an error of 5 K in T_{eff} could lead to a 5% error in the soil moisture product. Even when using the C-band, which is less sensitive to the T_{eff} parameterization than the L-band, accurate estimates of T_{eff} are still essential for converting emissivity into brightness temperature [135].

The primary objective of the current study is to compare T_{eff} estimated and used by the current SMOS and the SMAP schemes (both the Beta version and Choudhury's scheme) and to examine their influence on the retrieved emissivity (the intermediate variable directly related to soil moisture). The method and data discussed here will hopefully influence the retrieval approach to the SMAP mission launched in January 2015 and enhance its global soil moisture products.

4.2 Method and Data

4.2.1 MERRA-Land Data

The Modern-Era Retrospective analysis for Research and Applications (MERRA) was a global atmospheric reanalysis undertaken by NASA/GMAO [147]. With the updated catchment land surface model and precipitation data, MERRA-Land provides a globally integrated, coherent (means coupled with the atmosphere) estimate of soil moisture and temperature from 1979 to the present [148]. In this chapter, hourly global soil moisture and temperature profiles were taken in 2013 to reproduce T_{eff} , using Lv's multilayer scheme (hereafter referred to as TM), the current SMOS scheme (e.g., a two-layer scheme, hereafter referred to as T2W), the SMAP scheme (hereafter referred to as T2C), and the Beta SMAP scheme (e.g. one layer scheme, hereafter referred to as T1). MERRA-Land has a spatial resolution of 0.67 x 0.50 degrees. This product makes it possible to create daily global T_{eff} maps at 6:00 a.m. (ascending/descending for SMOS/SMAP) and 6:00 p.m. (descending/ascending for SMOS/SMAP) local solar time for all time zones. To enable soil moisture and temperature values to be acquired at the exact local solar time, all pixels are temporally interpolated according to their longitudes.

4.2.2 SMOS Brightness Temperature

The CATDS Centre (Centre Aval de Traitement des Données; http://catds.ifremer.fr/) SMOS Level 3 brightness temperature T_B products (SMOS L3c) were used to assess the influence of T_{eff} on emissivity. SMOS L3c offers daily brightness temperature intensities on a grid with a resolution of 0.25 x 0.3125 degrees. SMOS L3c includes V and H full polarized T_b at incidence angles between 0 and 65°. This chapter only analyzed incidence angles of 42.5°, which is close to the incidence angle of 40° used by the SMAP mission. As horizontal polarization is primarily used in the context of soil moisture retrieval, this paper uses only H brightness temperature.

4.2.3 Effective Temperature Models

As indicated above, the T1, T2C, T2W and TM schemes will be used to reproduce T_{eff} comp with retrievals scheme. The Beta SMAP T_{eff} scheme [140], referred to here as T1, is interpreted as a single layer T_{eff} scheme because it needs sensing depth or weighting between different layers. For the SMAP soil moisture retrieval algorithms, T_{eff} is considered to be the average (or effective) temperature of the top 5 cm layer of the soil. T_{eff} is obtained from MERRA-Land data by taking the arithmetic mean of two parameters – TSURF (soil skin temperature at DZTS in Table 4.1) and TSOIL1 (soil temperature at DZGT1) – at their native resolution of 0.67 x 0.50 degrees. See Table 4.1 for a definition of TSOIL1 and other layering information used in the following description.

Table 4.1 MERRA-Land soil temperature/moisture data for layers 1-7, prepared as input for Equation (4.2). MERRA-Land also provides data on layers 8 and 9, but this was not used in the present study.

Layer		**1**	**2**	**3**	**4**	**5**	**6**	**7**	**8**	**9**
Soil Moisture	Variable Name	DZSF[1]		DZRZ[2]				None		
	Depth(m)	0-0.02		0.02-0.3401						
Soil Temperature	Variable Name	DZTS[3] (TSURF)	DZGT1[4] (TSOIL1)		DZGT2(TSOIL2)	DZGT3 (TSOIL3)	DZGT4		DZGT5	DZGT
	Depth(m)	0 -0.018	0.018 -0.0988		0.0988 -0.294	0.294 -0.6799	0.6799 -1.4425		1.4425 -2.9496	2.949 -10

1 DZSF: Thickness of soil layer associated with top soil layer soil moisture content.
2 DZRZ: Thickness of soil layer associated with root zone soil moisture content.
3 DZTS: Thickness of soil layer associated with non-snow surface temperature components.
4 DZGT: Thickness of soil layer associated with i^{th} layer.

The updated SMAP T_{eff} scheme (T2C) uses Choudhury's model as follows:

$$T_{eff} = T_{soil\_deep} + C(T_{soil\_top} - T_{soil\_deep}) \tag{4.2}$$

where T_{soil_top} refers to the soil temperature (TSOIL1) of MERRA-Land layer 1 (at a depth of 0-10 cm) and T_{soil_deep} the soil temperature (TSOIL2) of MERRA-Land layer 2 (at a depth of 10-20 cm). C= 0.246 is given for 1.4GHz [86].

The current SMOS T_{eff} scheme (T2W) is also a two-layer scheme. T2W with $C=\left(\frac{W_s}{W_0}\right)^b$ in Equation (4.2), where W_s is the 0–3 cm surface soil moisture (this depth interval corresponds well with the effective soil moisture value contributing to soil emission in the L band), W_0 and b are semi-empirical parameters depending on specific soil characteristics. With clay fractions <0.6 and sand fractions <0.5 [80, 109]. In SMOS ATDB [81], the default setting is $W_0=0.3$ m³/m³ and $b=0.3$. This default setting will be applied in this chapter.

Table 4.2 Different schemes used for calculating T_{eff}.

Name	Parameterization	Layers
T1	$T_{eff}=(T_1+T_\infty)/2$	$T_1=TSURF$ $T_\infty=TSOIL1$
T2C	$T_{eff}=T_\infty+(T_1-T_\infty)C$, $C=0.246$	$T_1=TSOIL1$ $T_\infty=TSOIL2$
T2W	$T_{eff}=T_\infty+(T_1-T_\infty)\left(\frac{W_s}{W_0}\right)^b$, $\min\left[\left(\frac{W_s}{W_0}\right)^b,1\right]$, $\begin{cases}W_0=0.3\\b=0.3\end{cases}$	$T_1=TSOIL1$ $T_\infty=TSOIL3$ $W_s=DZSF$
TM	$T_{eff}=T_1\left(1-e^{-B_1}\right)+\sum_{i=2}^{n-1}T_i\left(1-e^{-B_i}\right)\prod_{j=1}^{i-1}e^{-B_j}+T_n\prod_{j=1}^{n-1}e^{-B_j}$	All

TM is the multilayer T_{eff} scheme developed by Lv et al. (2014), which introduces a simple two-layer model and without infinite integral model. With an increasing number of layers, TM approaches Wilheit's integral theory. TM can be expressed as:

$$T_{eff}=T_1\left(1-e^{-B_1}\right)+\sum_{i=2}^{n-1}T_i\left(1-e^{-B_i}\right)\prod_{j=1}^{i-1}e^{-B_j}+T_n\prod_{j=1}^{n-1}e^{-B_j} \tag{4.3}$$

with $B_i=\Delta x_i\cdot\frac{4\pi}{\lambda}\cdot\frac{\varepsilon_i''}{2\sqrt{\varepsilon_i'}}$. T_1, T_i and T_n are the average soil temperatures of the 1st, i^{th}, and bottom layers. λ is the wavelength, which for both SMOS and SMAP is 21 cm. ε_i'' and ε_i' are the dielectric constants

computed from Mironov's model [83, 149] using soil moisture and soil temperature data. Δx_i is the soil layer thickness at which soil moisture and soil temperature are considered to be constant. In this application, this corresponds exactly to the layer depths defined in the MERRA model. Details of the soil layer definition used in MERRA are given in Table 4.1 also listed in the MERRA-Land handbook [150]. Using Equation (4.3), all soil moisture data and soil temperature data from MERRA-Land are be used to calculate T_{eff} . The soil moisture profile layers do not correspond to the one of the soil temperature profile in MERRA-Land because the catchment model does not have a traditional 'layer-based' structure. The layer depth associated with the root zone moisture content is given as a temporally constant field (abbreviated to DZRZ, see Table 4.1). All schemes are listed in Table 4.2.

4.2.4 Dielectric Models

According to Equation (4.3), TM depends on the dielectric model especially for the simplest two-layer form of TM because the impact of the dielectric model will be amplified by the soil temperature difference between the two layers (Lv et al. 2014). However, this impact is minimized by the relatively small temperature differences between neighboring layers when additional layers are taken into consideration. The Mironov dielectric model was adopted by the SMOS mission for emissivity computations. The Mironov model performs more effectively than the Dobson model [84] or Wang and Schmugge's model [85], especially at low microwave frequencies, because it requires less input, and it is based on a physical approach [151]. Section 4.3.2 compares Mironov's, Wang and Schmugge's, and Dobson's models with one another, to characterize this effect and to find out how different dielectric models affect T_{eff} .

4.2.5 Statistical Metrics

Three metrics were calculated for evaluating different models against the reference: (i) bias, (ii) root mean squared difference (RMSD), and (iii) emissivity difference (ED). The equations used to calculate the three indicators are [152]:

$$bias = \overline{\left(T_{eff-x} - T_{eff-ref}\right)} \tag{4.4}$$

$$RMSD = \sqrt{\overline{\left(T_{eff-x} - T_{eff-ref}\right)^2}} \tag{4.5}$$

$$ED = \frac{T_{B-L3c}}{T_{eff-x}} - \frac{T_{B-L3c}}{T_{eff-ref}} \tag{4.6}$$

where T_{B-L3c} is the observed SMOS L3c brightness temperature, $T_{eff-ref}$, T_{eff} comp with Wilheits model, and T_{eff-x} , T_{eff} comp with the refered mdels x.

4.3 Results and Discussions

4.3.1 Soil Temperature Profile

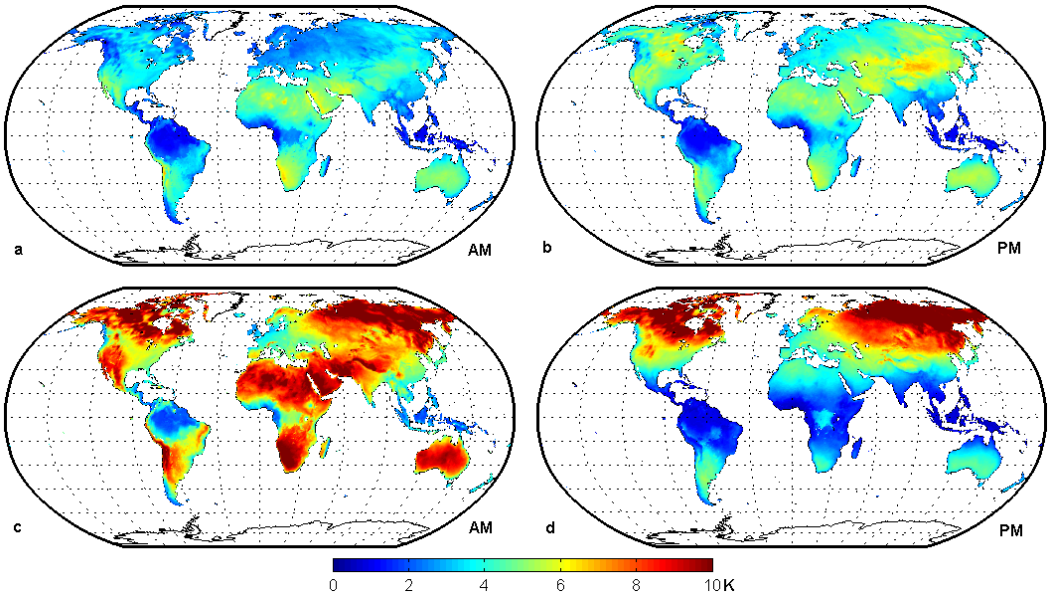

Figure 4.1 The soil temperature RMSD (K) of MERRA-Land for 2013 between a) TSOIL1 and TSOIL3 at 6:00 a.m.; b) TSOIL1 and TSOIL3 at 6:00 p.m.; c) TSURF and TSOIL3 at 6:00 a.m.; d) TSURF and TSOIL3 at 6:00 p.m. The depth of TSURF, TSOIL1 and TSOIL 3 are given in Table 4.1.

The previous SMAP T_{eff} scheme assumed that vegetation and soil temperature are equal for half-orbits that involve equator crossing (descending) at 6:00 a.m. This means that the terms for soil temperature and land surface temperature (referred to as T_s) can be used interchangeably [140]. The assumption of local thermal equilibrium at 6:00 a.m. (and 6:00 p.m.) is moderated by *in-situ* measurements and simulations [129, 153, 154].

Figure 4.1 shows the RMSD between the soil temperatures TSOIL1 and TSOIL3, as well as TSURF and TSOIL3 (see Table 4.1 for definition) in the MERRA-Land data for 2013. At 6:00 a.m., the difference between the two layers (ca. 6 K) is small (Figure 4.1a). Maximum RMSD (6 K) are only found in the arid regions around the subtropics. At 6:00 p.m., for Central Asia and North America, the RMSD between TSOIL1 and TSOIL3 can reach 8K (Figure 4.1b). The difference between TSURF and TSOIL3 are large outside of tropical areas at 6:00 p.m (>10 K) (Figure 4.1c). The assumption of local thermal equilibrium is only approximately valid for tropical to subtropical regions (c.a. 1K) at 6:00 p.m. (Figure 4.1d). In the temperate zones, the differences between TSURF and TSOIL3 increases to 4 K and reaches 10 K in the boreal zone. Thus the assumption of a local thermal equilibrium [140] reflects TSURF and TSOIL1 is critical in T1 (Beta version SMAP).

Figure 4.2 shows the applicability of Wigneron's scheme at 6:00 a.m. and 6:00 p.m., based on MERRA-Land data. The blank areas are invalid regions, while the remaining areas are color-coded to indicate the number of days on which the soil was frozen (TSOIL1<273.15-0.5K) in 2013. Accordingly, Wigneron's scheme cannot be used for 43.6% of the land area and on average 67 days per pixel for the colored areas.

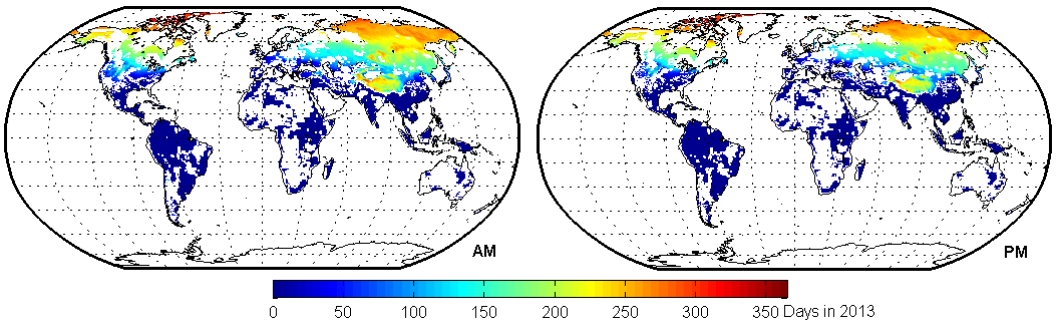

Figure 4.2 The applicability of Wigneron's scheme. The blank land area is invalid due to soil texture restrictions while the color coding indicates the number of invalid days in 2013 due to frozen soil.

4.3.2 Comparison of Dielectric Constant Models

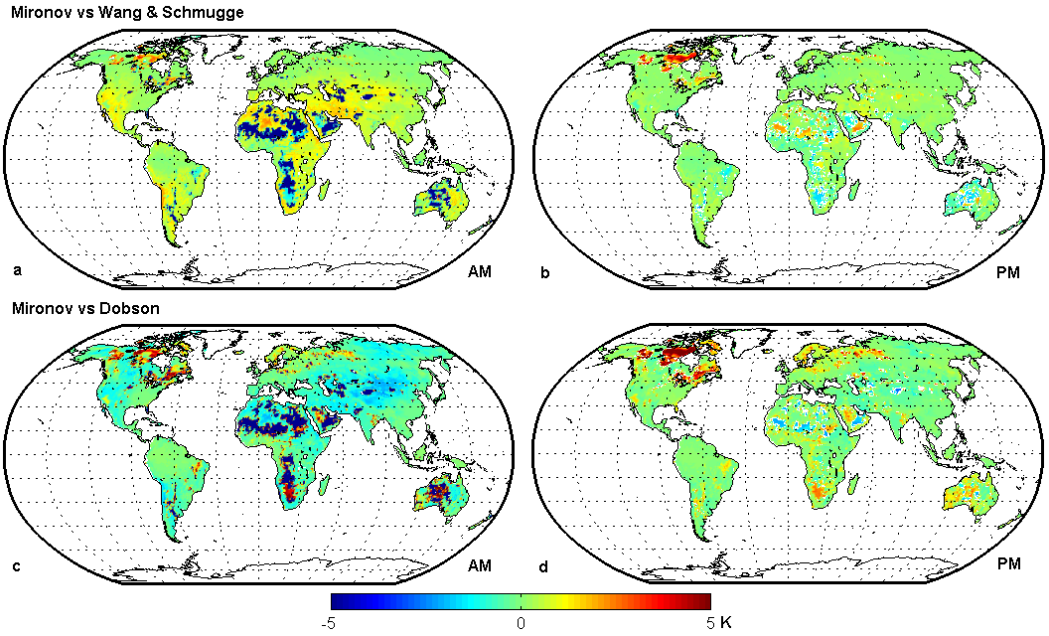

Figure 4.3 The annually averaged bias (K) between T_{eff} calculated by TM using Mironov's dielectric constant model vs. that of Wang and Schmugge (a and b), and between Mironov's model and Dobson's (c and d). The data used was from MERRA-Land and frozen/thaw days are not included.

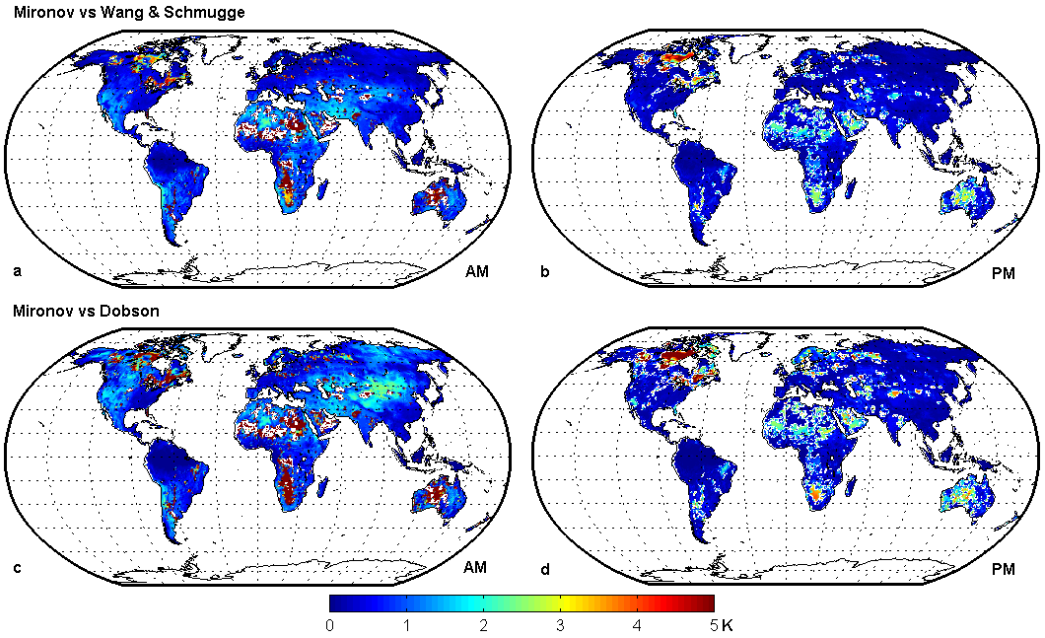

Figure 4.4 The RMSD (K) between the T_{eff} value calculated by TM using Mironov's dielectric constant model vs. that of Wang and Schmugge (a and b), and between Mironov's model and Dobson's (c and d), for 2013. The data used was from MERRA-Land and frozen/thaw days are not included.

The study by Lv et al. (2014), indicates that Lv's multilayer T_{eff} can be applied to the full range of soil moisture conditions and corresponding weight ranges from 0 to 1, which are however heavily dependent on the dielectric constant model used. Figure 4.3 shows that the bias (introduced by using either Wang and Schmugge's model or Dobson's model) in T_{eff} calculated using TM is less than 1 K for most areas. Exceptions are subtropical deserts in Africa and Australia, as well as the northeastern part of North America. Within these regions, there is no significant difference between Dobson's model or Mironov's model regarding the T_{eff} values calculated using TM (bias<1 K and RMSD<1 K, see Figures 4.3c and 4.3d, Figures 4.4c and 4.4d). In general, the bias and RMSD resulting from the use of different dielectric constant models are less than 1K, except for arid or frozen areas (less than 35% for the total land mask). To ensure that comparisons are consistent, the color bar used in Figures 4.3 and 4.4 has the same range as in other bias and RMSD maps.

4.3.3 Comparison of soil effective temperature schemes

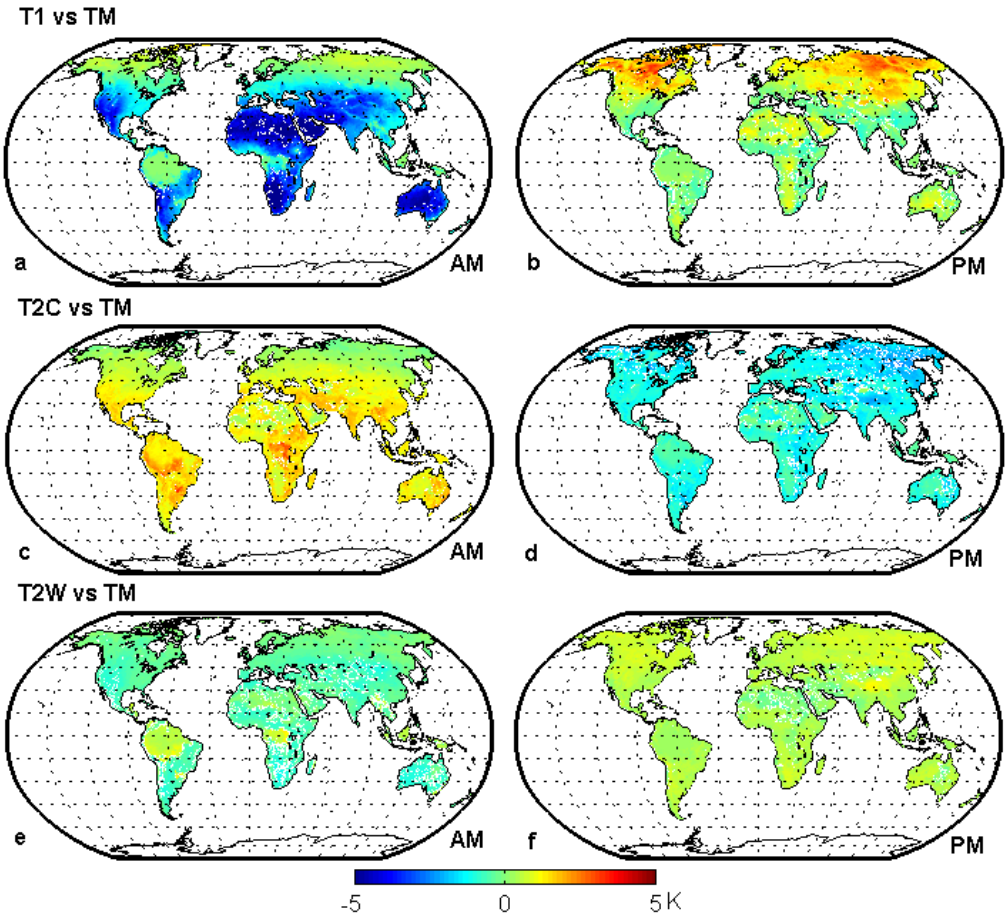

Figure 4.5 The annually averaged bias (K) between T_{eff} calculated by T1 and TM (a and b), T2C and TM (c and d), and T2W and TM (e and f). The data used was from MERRA-Land and frozen/thaw areas are not included.

In this section, TM is used as the reference scheme ($T_{eff-ref}$) as it achieves the best approximation of Wilheit's integral theory when using all the available soil moisture data and soil temperature data from MERRA-Land. Wilheit's scheme is not used as the reference because with seven layers, the integration would not be precise. Bias and RMSD throughout 2013 were calculated to assess the performance of different T_{eff} schemes relative to the result obtained using the reference scheme. Furthermore, TM will be used to analyze each layer's contribution to the calculation of T_{eff} .

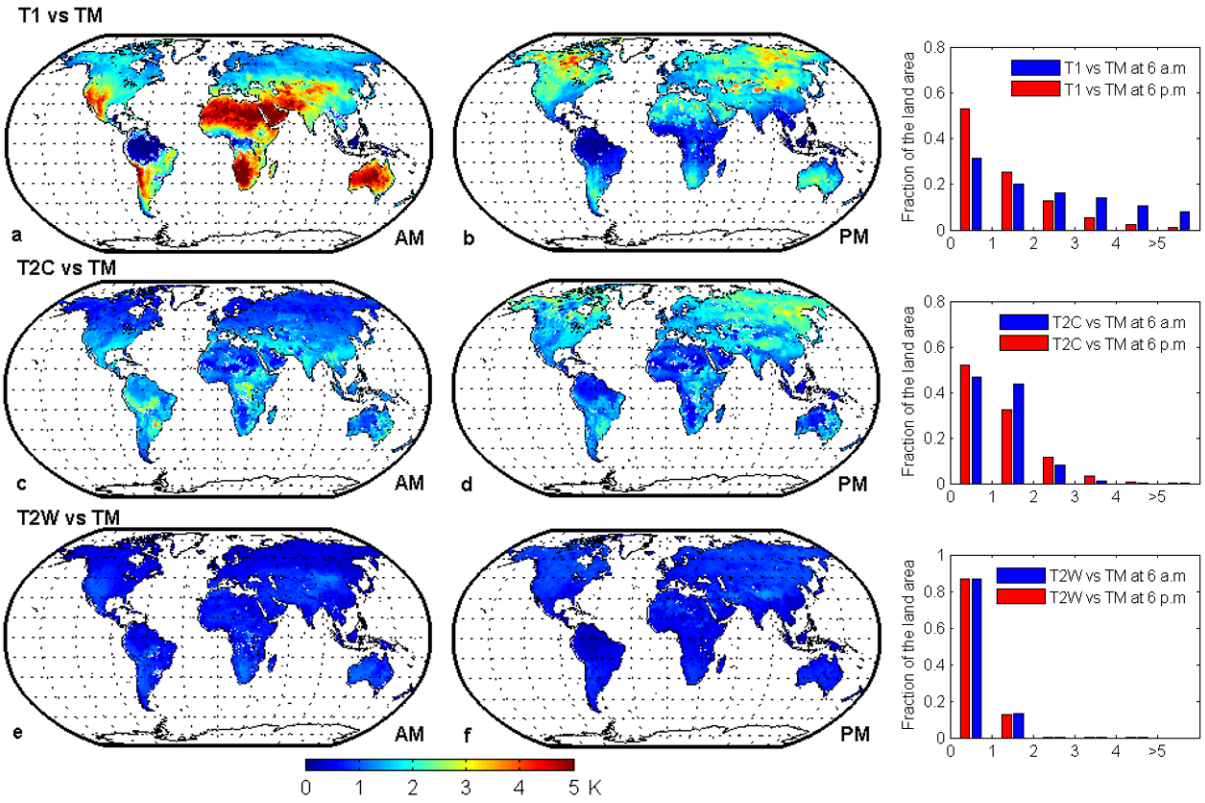

Figure 4.6 Global RMSD distribution(in K) between T1 and TM (a and b), T2C and TM (c and d), T2W and TM (e and f). The corresponding histograms are shown in the panels on the right. Frozen/thaw days are not included.

Deviations in T_{eff} between T1 and TM, at 6:00 a.m. (descending) and 6:00 p.m. (ascending) are illustrated in Figures 4.5a and 4.5b. T1 is calculated using the average of TSOIL1 and TSURF, as indicated in Section 4.2 (c). T1 is lower at 6:00 a.m. but higher at 6:00 p.m. In general, a maximum bias of 5 K is found in all continents and even ranges up to 10 K in some areas. Areas with large biases include not only arid and semi-arid regions (where the effect of T_{eff} is thought to be significant, due to the greater sensing depth), but also vegetated land cover types such as crops and forest, where T_{eff} is thought to be much less important. The bias between T2C and TM is much smaller than that between TM and T1 (Figures 4.5c and 4.5d), declining from approximately 5 K to around 2~3 K, except for areas at high latitudes.

Figures 4.5e and 4.5f show that the difference between T_{eff} values calculated by T2W and by TM is quite small, it is less than 1.5 K for most of the land area. In this chapter, we used MERRA-Land TSOIL1 soil temperature data for both T_{eff} schemes. MERRA-Land data was used to facilitate consistent comparisons between SMOS and SMAP. Accordingly, when compared to TM, T2W gives lower T_{eff} values

at 6:00 a.m. and higher ones at 6:00 p.m. T_{eff} results obtained around the world by T2W and TM are very similar even in situations where Wigneron's scheme is invalid.

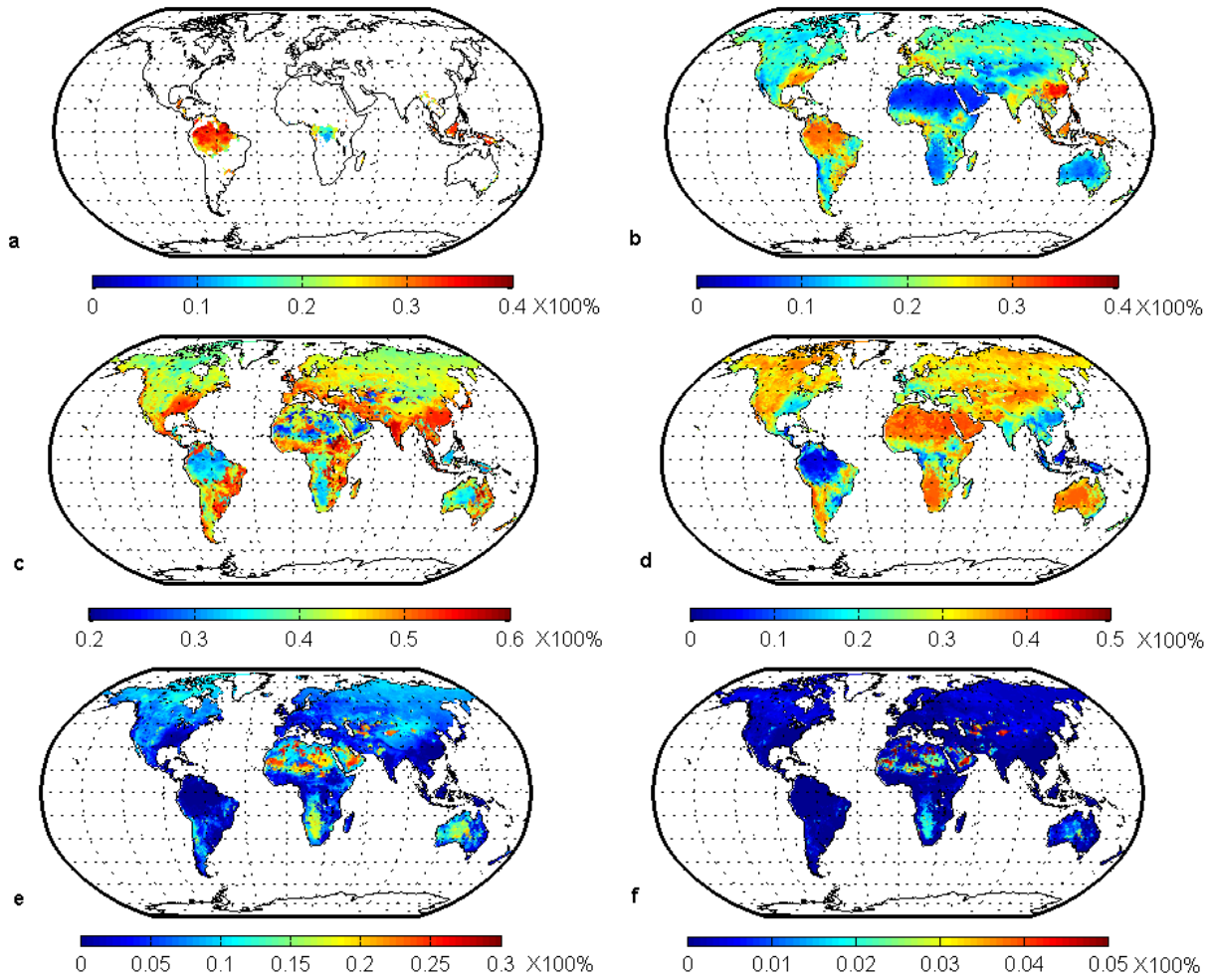

Figure 4.7 The annually averaged contribution of each layer in calculating T_{eff}. Their depths (a-f) correspond to the layers in Table 4.1 (Layers 1-6) as defined by MERRA-Land. Layers 7, 8 and 9 are not shown, as the small contribution from Layer 6(f) means that the contributions of underlying layers will be negligible.

It is interesting to note that the greater difference in soil temperature observed between TSURF and TSOIL3 in high latitude regions (>10 K in Figures 4.1c and 4.1d) does not lead to larger bias in T_{eff}, when compared to the corresponding values in Figures 4.5a and 4.5b. This is mainly because frozen soil is included in Figure 4.1 while not in Figure 4.5.

Figure 4.6 illustrates the differences between the various schemes regarding root-mean-square deviation (RMSD). T1 shows the greatest deviation, both regarding bias and of RMSD, relative to TM. At 6:00 a.m., regions with an RMSD more than 5K are distributed around the globe, except in high latitude

areas of the Northern Hemisphere. By contrast, at 6:00 p.m., almost all regions (aside from high latitudes areas of the Northern Hemisphere) show a deviation of less than 5 K. The RMSD distribution between T2C and TM, which corresponds to Figures 4.6c and 4.6d, is intermediate to those between T2W and TM and those between T1 and TM. The RSMD exceeds 2 K in only 10 percent of the land area. T2W and TM are close to each other under any condition.

Any overestimation/underestimation of T_{eff} will result in dryer/wetter soil moisture estimates. Although any variation of the brightness temperature caused by T_{eff} would be less than the variation in T_{eff} itself, biases in excess of 5 K cannot be ignored. According to [155], while it is one order of magnitude lower than the uncertainty due to vegetation, roughness and soil moisture. 5 K could involve a potential error in the calculation of brightness temperature. The comparison in Figure 4.6 shows that large deviations can occur in the calculation of T_{eff} , potentially resulting in errors in the final soil moisture products. This nevertheless effect has been assumed negligible, relative to the error caused by soil temperature deviations [40].

Since the current T1/T2C/T2W two-layer schemes include Holmes's [87], can only use for the MERRA-Land soil temperature data/moisture data only for a single layer as their input; potential contributions from other layers are ignored. From Wilheit's integral theory, it can be inferred that, if the dielectric constant and the wavelength are changing, each layer's contribution will also vary. The weighting function varies with soil moisture and soil temperature. TSOIL1 and TSOIL2 were selected as the inputs for T2C. While they perform relatively well, the physical reasons for this have yet to be explained. Given the layer's signal contribution, an attempt has been made to account for this.

Using Equation (4.3), the temporal average contribution of each layer can be calculated by using $\left(1-e^{-B_1}\right)$ for the first layer, $\left(1-e^{-B_i}\right)\prod_{j=1}^{i-1}e^{-B_j}$ for the middle layers, and $\prod_{j=1}^{n-1}e^{-B_j}$ for the bottom layer. In MERRA-Land, soil temperature is defined for seven layers (including surface soil temperature) with fixed thicknesses (depth), while soil moisture uses only two layers (DZSF and DZRZ) which vary for different pixels (Table 4.1). As shown in Table 4.1, Layer 1 uses the soil moisture of DZSF and the soil temperature of DZTS. Layers 2 and 3 both use the temperature of DZGT1, together with the soil moisture of DZSF (Layer 2) and DZRZ (Layer 3). Layers 4, 5 and 6 use the soil moisture of DZRZ, together with the soil temperature of DZGT2, DZGT3, and DZGT4 (Table 4.1). There is no corresponding soil moisture data for Layers 8 and 9, so these layers are not taken into account when using Lv's scheme. Even though the soil profile information provided by MERRA-Land cannot facilitate the straightforward application of Wilheit's theory, the treatment of soil layers (as indicated in Table 4.1) can be adapted to calculate the weighting of different layers (regarding their contribution to calculating T_{eff}), using Lv's multilayer scheme.

Figure 4.7 indicates the weighting of the contributions of layers 1 to 6, listed in Table 4.1. The weighting of Layer 1's contribution is small, only impacting a few tropical regions. As expected, the deeper

layers (Layer 2, 3 and 4 in Figures 4.7b, 4.7c, and 4.7d) account for more than half to T_{eff} for most of the regions, although the weighting is unevenly distributed around the globe. Layers 4 and 5 are not involved in the SMAP scheme for calculating T_{eff} , while Figures 4.7d and 4.7e indicate that these layers contribute at least 40% of all signals. In Wigneron's scheme, Layer 5 is treated as the deeper layer, so its temperature contribution is partially included. This results in a lower bias between T2C/T2W and TM than between T1 and TM (Figures 4.5 and 4.6). The contribution from Layer 6 is small (less than 5%, Figure 4.7f), thus soil temperatures in layers 7, 8 and 9 are negligible. Contribution from the layer below 10 cm accounts for more than 60% (the sum of Layers 3 to 6, Figures 4.7c/4.7d/4.7e/4.7f). Thus, with only TSURF and TSOIL1 are considered, T1 assumption is not appropriate. For T2C, TSOIL1 and TSOIL2 are taken as inputs corresponding to Layer 2 to 4 (Figures 4.7b/4.7c/4.7d). The contribution of these three layers amounts to more than 80% and partly explains the improvements seen from T1 to T2C.

4.3.4 Emissivity affected by soil effective temperature schemes

In addition to the difference in T_{eff} resulting from the use of different T_{eff} computation schemes, the actual error in soil moisture introduced by the various T_{eff} schemes (via emissivity) also needs to be quantified. In microwave remote sensing, emissivity is related to soil moisture (see Equation (4.1)). It also provides information valuable for other variables, such as salinity, frozen/thaw conditions, and sampling depth. For the analyzes are the SMOS brightness temperature at an incidence angle of 42.5° in this analysis. Since SMOS's maximum revisit interval is 3 days, the 2013 SMOS L3c data have been merged to create a global map. Only the maximum emissivity values for regions covered by the satellite overpasses are shown here. The SMOS L3c data was re-projected from its original coordinate systems onto a regular grid, using a Nearest Neighbor approach to match it to MERRA-Land´s EASE (Equal Area Scalable Earth) grid. Using the above configuration. Figure 4.8 shows the difference in derived estimates to the affected T_{eff} .

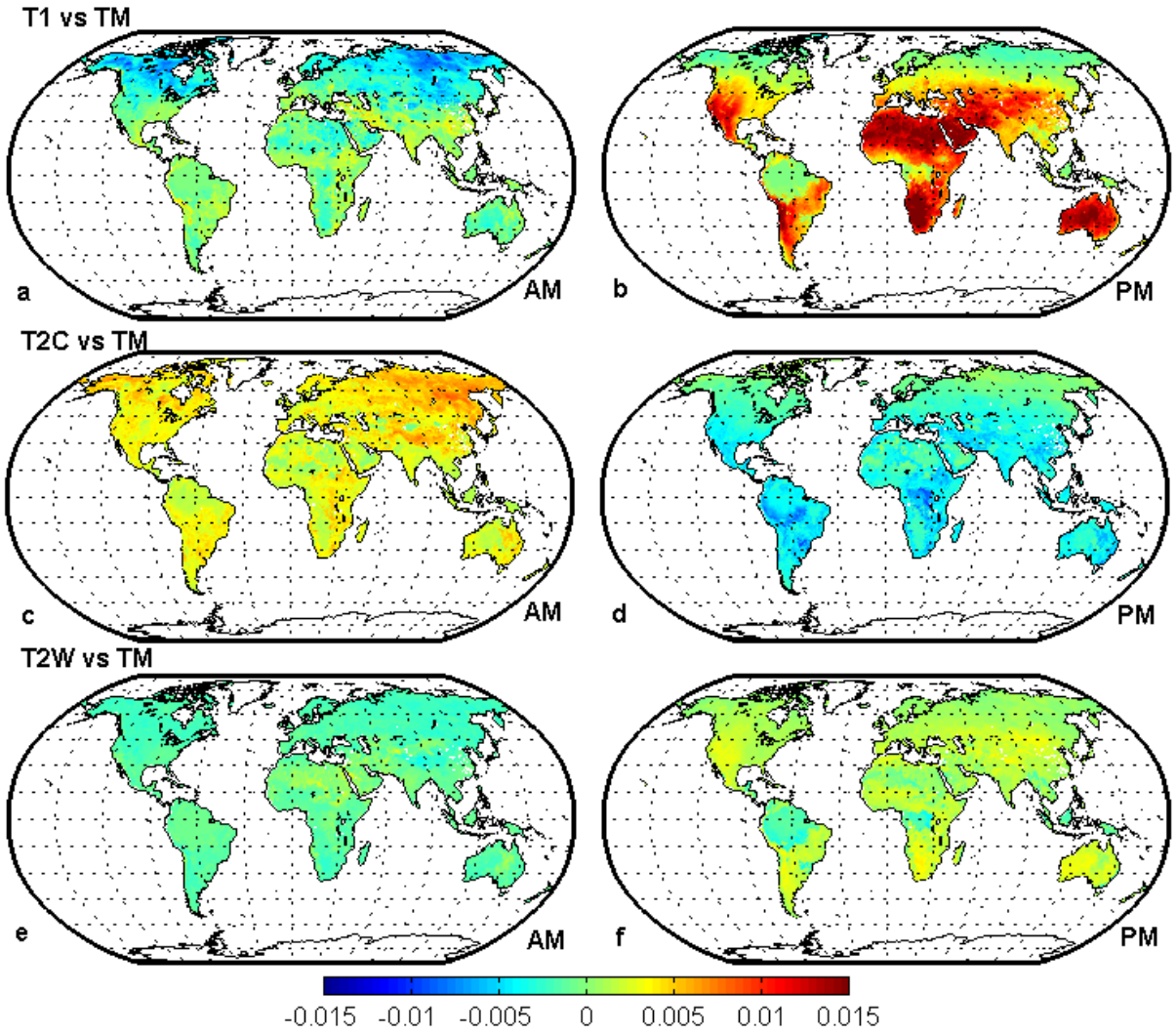

Figure 4.8 H Polarization Emissivity Difference between various T_{eff} schemes. Computed from MERRA-Land and SMOS L3c from July 1st to 3rd, 2010. a) T1 vs TM, descending; b) T1 vs TM, ascending; c) T2C vs TM, descending; d) T2C vs TM, ascending; e) T2W vs TM, descending; f) T2W vs TM,

The variation of estimated soil moisture can range from 0.01 to 0.04 $cm^3 \cdot cm^{-3}$ for each 0.01 change in emissivity [92, 156]. Regions, where the emissivity difference exceeds ±0.015, are marked in red/blue. For the comparison between T1 and TM, these regions include Siberia, Canada, the subtropical areas of Africa and Australia (Figures 4.8a and 4.8b). The total area with emissivity differences between T1 and TM greater than 0.01 is 0.04% (AM), and 16.56% (PM). When comparing T2C with TM (Figures 4.8c and 8d), these areas are reduced to 0.01% (AM) and 0.03% (PM). This shows that the update in the SMAP processing from T1 and T2C represents a large improvement. The areas with emissivity difference>0.01 are further reduced in the comparison between T2W and TM (Figures 4.8e and 4.8f). This shows the merit of including a moisture dependent weighting factor.

4.4 Conclusions

The bias and RMSD from various T_{eff} schemes – SMOS (T2W), the beta version of SMAP (T1) and T2C, to Lv's multilayer scheme (TM) as a good approximate to Wilheit's scheme can be 5 K for T1, but much lower for T2C and T2W. The differences relate not only to arid and semi-arid regions (where soil moisture is very low) but also to regions with other land-cover types. Differences can lead to different estimates of emissivity and, accordingly, of soil moisture. A comparison between T1 and TM reveals substantial bias and RMSD across the globe. Such a large difference or degree of uncertainty in calculating T_{eff} can significantly affect soil moisture retrieval. In summary, the main findings are:

1) The contribution to T_{eff} from the layer below 10 cm, which is not addressed in the Beta SMAP scheme (T1), can be as high as 60% for most parts of the globe. By including deeper layers, T2C effective accommodates this contribution. The soil texture restriction is not important T2W;
2) The updated SMAP T_{eff} calculation improves by incorporating both TSOIL1 and TSOIL2 as input layers in the weighting function;
3) When using MERRA-Land data, the Lv multilayer T_{eff} scheme is less dependent on the dielectric model. Only in desert areas can the effect of the soil dielectric model on the calculated T_{eff} reach 5 K.

Chapter

5 Estimation of Penetration Depth from Soil Effective Temperature at L-Band in Microwave Radiometry[4]

Abstract: Soil moisture is an essential variable in Earth surface modeling. Two dedicated satellite missions, the Soil Moisture and Ocean Salinity (SMOS) and the Soil Moisture Active Passive (SMAP), are currently in operation to map the global distribution of soil moisture. However, at the L-band wavelength at which these satellites measure, the emitting behavior of the land is complex due to the unknown and variable penetration depth. This variability creates uncertainty when calibrating and validating derived soil moisture products. In the framework of the zeroth-order incoherent microwave radiative transfer model, the soil effective temperature is the only component that contains depth information and thus provides the link to penetration depth. Using a multi-layer soil effective temperature scheme, we determined the relationship between penetration depth and soil effective temperature and verified it against field observations at the Maqu Network. Penetration depth can be estimated with Lv's T_{eff} scheme with the assumption of a constant soil temperature gradient in the soil layer significantly contributing to the brightness temperature T_B. Conversely, the soil temperature at the penetration depth should equal the soil effective temperature with the same linear assumption. The accuracy of this inference depends on to what extent the assumption of the linear soil temperature gradient is satisfied. The result of this study will advance our understanding of soil moisture products retrieved by SMOS and SMAP and improve data assimilation techniques in and help in climate research.

Keywords: microwave remote sensing; soil moisture; Maqu network; penetration depth; soil effective temperature

[4] This chapter is based on

Shaoning Lv, Yijian Zeng, Jun Wen, Hong Zhao, Zhongbo Su. 2018. Estimation of Penetration Depth from Soil Effective Temperature at Land in Microwave Radiometry. Remote Sensing 2018, 10, 519; doi:10.3390/rs10040519

5.1 Introduction

Soil moisture is a key variable in weather forecast and climate research because it plays a role in both the energy and water cycles [157-160]. It controls how much water returns to the atmosphere via land-atmosphere interactions, and it also carries the energy regarding the latent heat flux when evaporated to reshape the atmospheric circulation. Therefore, availability of accurate and near real-time global soil moisture is critical for the improvement of the weather forecast and climate projection skills [71, 161, 162].

Since the 1970s, satellite remote sensing has been used to estimate global soil moisture distributions with microwave frequencies, and more recently focus has been on L-band (1400–1427 MHz), which is sensitive to the dielectric constant and contributes a protected radio band with minimum radio frequency interference (RFI). Both the Soil Moisture and Ocean Salinity (SMOS) [40] and the Soil Moisture Active Passive (SMAP) [43] missions operate at L-band for providing the brightness temperature and derived soil moisture data products. With the SMOS and SMAP missions, abundant data have been produced and applied in various studies [115, 163-166].

Corresponding to the satellite missions, plenty of in situ soil moisture monitoring networks have been established to calibrate and validate (Cal/Val) L-band brightness temperatures (T_b) or derived soil moisture[24]. L-band emission is however strongly affected by both soil temperature and soil moisture [167, 168], which usually leads to questions on what the satellite is exactly sensing [90, 169, 170]. Usually, soil moisture and soil temperature sensors are installed at certain depths based on different preferences, e.g., 2.5 cm, 5 cm, 10 cm, or deeper, to match numerical simulations of soil moisture and soil temperature. However, depths do not necessarily cover the sensing depths, for which T_b or derived soil moisture data these are. Hence errors may arise because the Cal/Val data are not optimally sampled, and thus reprehensive are not comparable with the satellite observations. Different satellite soil moisture products may have different sensing depths, as different frequencies are used. As such, the various satellite soil moisture products may lack consistency and generate ambiguity in Cal/Val and their applications [154].

Regarding the profile of the dielectric constant with depth, the SMOS/SMAP sensors sense soil moisture over a deeper or less deep layer, which is deeper in the dry soil than in wet soil. Even for the same region, the depth with significant contributions may vary depending on soil moisture and to some extent also on soil temperature profiles [90, 92], which must be considered when computing different soil estimated products. Data assimilation is deemed the optimal method for estimating the soil moisture profile [92, 171] because it extrapolates the remotely sensed surface information to lower depths in the soil via a coupled heat and moisture flow model. It is, therefore, critical to understanding which depth is sensed by a satellite sensor. The knowledge of the sensing depth (penetration depth in this chapter) strongly affects the accuracy of the soil moisture and soil temperature profile, as the derived soil moisture and temperature near the surface may have strong gradients. One way to infer soil moisture sensing depth is by correlating brightness temperatures with *in-situ* soil moisture time-series at different depth so that the soil moisture layer

best correlates with the brightness temperature considered as the sensing layer [65, 172]. Another way is to use models to compute the sensing depth according to its definition [63, 173] or an empirical model [63, 174]. However, these methods need either vertically dense profile information or relies on prior knowledge, which is hard to acquire in practice. Besides soil, also vegetation affects the penetration depth. The attenuation by vegetation depends on the vegetation water content.

As the penetration depth (henceforth we use penetration depth synonymously with sensing depth and emission depth) is defined by energy attenuation, it is possible to infer it from T_{eff} in the zeroth-order incoherent model. Two-layer T_{eff} schemes contribute a weighted average of the soil temperature of an upper layer and a deeper layer. Such weighting functions can be a constant [86], a fitting function [80] and [87], or an exponential function [167, 168]. The weighting function is supposed to reflect the impact of soil moisture on the soil effective temperature. While the true weighting function considers the influence of both the soil moisture and soil temperature. However, it is difficult to quantify its effect on soil effective temperature, because soil temperature also affects the dielectric constant (e.g., as in dielectric constant models). In other words, T_{eff} is a weighted mean of the soil temperature along the vertical profile with the weight. Accordingly, $T_{\min} \le T_{eff} \le T_{\max}$. Considering the diurnal variation and a semi unbounded soil column, $T_{\max}$ and $T_{\min}$ usually appear at the surface skin or the deep layer where the soil temperature stays almost constant. A soil temperature profile is continuous, and there must be a layer where the soil temperature equals T_{eff}.

To investigate the relationship between penetration depth and T_{eff}, we first review the hypotheses of coherent/incoherent microwave radiative transfer models and the definition of satellite sensing depth (Section 5.2). We then analytically quantify the relationship between penetration depth and T_{eff} (Section 5.3). Next, we use soil moisture and soil temperature observations of the Maqu Network to verify the developed approach and demonstrate its application to SMAP (Section 5.4). Finally, we discuss the uncertainties of the developed method (Section 5.5) and conclude with final thoughts for future work (Section 5.6).

5.2 Theoretical Background

In this section, we first review the assumptions in the zeroth-order incoherent model, which assumes one emissivity for all layers, and then reformulate Lv's T_{eff} scheme concerning optical depth τ and clarify the meaning of penetration depth.

5.2.1 Microwave Radiative Transfer Model

The SMOS and SMAP soil moisture retrieval algorithms are based on

$$T_B = \varepsilon T_{eff} \tag{5.1}$$

where T_B is the brightness temperature detected by the radiometer, ε is the emissivity of the soil following the Fresnel reflectivity equation, and T_{eff} is the soil effective temperature [62]. Equation (5.1) implies that ε does not change with depth while T_{eff} is defined by $T_{eff} = \int_0^\infty T(x)\alpha(x)\exp\left[-\int_0^x \alpha(x')dx'\right]dx$ with α the radiative absorption coefficient given by $\alpha(x) = \frac{4\pi}{\lambda}\varepsilon''(x)\Big/2\left[\varepsilon'(x)\right]^{\frac{1}{2}}$ and approximated usually by a weighted average temperature of two layers as

$$T_{eff} = w_1 T_1 + w_2 T_2 \tag{5.2}$$

where T_1 represents the soil temperature at 0–5 cm and T_2 at 40–80 cm or even deeper depending on the soil texture. The weights w_1 and w_2 are mainly affected by soil moisture, wavelength and slightly also by soil temperature [168, 175] (Note: All variables used in this study are listed in Table 5.1). The sum of weights, which must be position being an approximation of $T_{eff} = \int_0^\infty T(x)\alpha(x)\exp\left[-\int_0^x \alpha(x')dx'\right]dx$, must satisfy:

$$w_1 + w_2 = 1 \tag{5.3}$$

Equations (5.1) and (5.2) assumes that the dielectric properties of the soil are uniform throughout the emitting layer. As we know, $T_{eff} \in (T_1, T_2)$ if $T_1 < T_2$. The opposite case is also possible as $T_{eff} \in (T_2, T_1)$ if $T_1 > T_2$. For a special case, when $T_1 = T_{eff}$ (or $T_2 = T_{eff}$), the only possible solution is $w_1 = 1$ (or $w_2 = 1$). $w_1 = 1$ is the necessary and sufficient condition for $T_1 = T_{eff}$.

In the following, we will prove that the soil temperature at one time the optical depth (penetration depth) equals T_{eff} with a linear soil temperature gradient assumption. The accuracy of this inference depends on whether the linear assumption is satisfied which is the case if more layers are observed.

Table 5.1. Variables used in this study.

Abbreviation	Definition	Unit	Expression
T_{eff}	soil effective temperature	K	Equations (5.5), (5.6), (5.12) and (5.13)
T_b	brightness temperature	K	
θ	soil moisture	Vol/Vol	
T_{max}	maximum soil temperature along soil temperature profile	K	
T_{min}	minimum soil temperature along soil temperature profile	K	

T_i	soil temperature of the i th layer	K	
w_i	Weightings of layer i for T_{eff}	-	Defined in [86, 87, 109]
Δx_i	soil thickness at i th layer	m	
$x_{(i)}$	soil depths at the bottom of the i th layer	m	$x_i = \sum_{j=1}^{i} \Delta x_j$
$\Delta \tau_i$	optical thickness of the i th layer	m	$\Delta \tau_i = \Delta x_i \frac{2\pi}{\lambda} \frac{\varepsilon''}{\sqrt{\varepsilon'}} = \Delta x_i \cdot \alpha_i$
$\tau_{i(x)}$	optical depth at the bottom of the i th layer (or corresponding to soil depth x)	m	$\tau_i = \sum_{j=1}^{i} \Delta \tau_j$
$T_{nor}\left(T_{inor}\right)$	normalized soil temperature of the i th layer	-	$T_{(i)nor} = \frac{T_{(i)} - T_{surf}}{T_{deep} - T_{surf}}$
T_{surf}	skin temperature	K	
T_{deep}	soil temperature at a deep layer the soil temperature can be considered constant	K	
a	soil temperature gradient with soil optical depth	K/τ	$a = dT/d\tau$
α_i	radiation absorption coefficient of the i th layer	-	$\alpha_i = \frac{4\pi}{\lambda} \varepsilon_i'' \Big/ 2\left[\varepsilon_i'\right]^{\frac{1}{2}}$
τ_{deep}	soil optical depth above which contributions to T_B are insignificant. This assumed that this is also the depth with soil temperature T_{deep}	-	$\tau_{deep} \approx 5$

5.2.2 Soil Effective Temperature

Accurate estimates of T_{eff} are critical for obtaining relevant values of soil emissivity from brightness temperature measurements. It follows that soil moisture can be retrieved from the estimate of soil emissivity [112]. Soil moisture and soil temperature profile information is usually limited even in field experiments because sensors are usually installed only a few depths. In Lv's scheme, Equation (5.1) can be written for a soil layer with constant temperature as

$$T_{eff} = T_1\left(1 - e^{-\Delta\tau_1}\right) + \sum_{i=2}^{n-1} T_i\left(1 - e^{-\Delta\tau_i}\right)\prod_{j=1}^{i-1} e^{-\Delta\tau_j} + T_n \prod_{j=1}^{n-1} e^{-\Delta\tau_j} \tag{5.4}$$

in which $\Delta\tau_i = \Delta x_i \frac{4\pi}{\lambda} \frac{\varepsilon''}{2\sqrt{\varepsilon'}}$ is the optical depth of layer i with soil depth Δx_i, and Lv's scheme uses an exponential function to distribute the weight among the different layers. T_i is the mean soil temperature of the i th layer, and $1 - e^{-\tau_i}\left(1 - e^{-\Delta\tau_i}\right)\prod_{j=1}^{i-1} e^{-\Delta\tau_j}$ is its weight in the calculation of T_{eff} . The dielectric constant varies with soil moisture and temperature.

As stated in Lv et al. (2016b), Δx_1 could be determined by considering τ_1 as a function of Δx_1 and the integral exponential function $\int_0^{\tau} e^{-\tau'} d\tau' = 1 - e^{-\tau}$,

$$e^{-\tau_{1s}} = \frac{1}{\tau_1}\int_0^{\tau_1} e^{-\tau} d\tau = \frac{1}{\tau_1}\left(1 - e^{-\tau_1}\right) \tag{5.5}$$

where τ_{1s} is calculated using the depth where the first layer sensors are installed (Δx_{1s}). See details in Chapter 2. With Equation (5.5), τ_1 can be determined as well as the Δx_1 used in Equation (5.4). The physical meaning of Δx_1 could be inferred from Equation (5.4) that T_1 matches the layer-averaged soil temperature integrated from the surface to the sampling depth Δx_1, which is used for calculating $1 - e^{-\tau_1}$. It is to note that Δx_1 (i.e., the bulk sampling layer thickness) is different from Δx_{1s} (i.e., the installation depth). Therefore, the soil moisture and soil temperature detected at Δx_{1s} represents average values from the surface to Δx_1, so that Δx_{1s} is the representative depth at the first layer. The representative depth is computed from the known installation depth for soil moisture and soil temperature sensors and has no deal with the deeper layers below. Let $\tau_1 = \Delta x_1 \cdot \frac{4\pi}{\lambda} \cdot \frac{\varepsilon''}{2\sqrt{\varepsilon'}}$ (noting $\Delta\tau_i = \tau_i - \tau_{i-1}, and\ \tau_{i-1} = 0$ for the first layer). Since soil depth at the bottom of the i th layer can be expressed as $x_i = \sum_{j=1}^{i} \Delta x_j$, it follows $\tau_i = \sum_{j=1}^{i} \Delta\tau_j$. Hence, τ monotonically increases with soil column depth x . With $\tau - T$ instead of $x - T$ we can compute the correlation coefficient (cc) along the profile.

5.2.3 Penetration Depth

The penetration depth Δx_T (Njoku and Entekhabi (1996)) can be defined by the following equation as:

$$\frac{\int_0^{\Delta x_T} T(x)\alpha(x)\exp\left[-\int_0^{x}\alpha(x')dx'\right]dx}{\int_0^{\infty} T(x)\alpha(x)\exp\left[-\int_0^{x}\alpha(x')dx'\right]dx} = \frac{1}{e} \tag{5.6}$$

Thus Δx_T is the depth when the optical thickness measured from the surface is equal to one, i.e., the depth when the intensity of radiation one a media (soil) is reduced to 1/e on the factors which influence the soil effective temperature (soil temperature, soil moisture, and wavelength λ) [73]. The dielectric model, while the soil moisture's influences dominate over the soil temperature one. When soil temperature is neglected, and soil moisture is vertically constant. Soil moisture and penetration depth ($\Delta x_T = f(\theta)$) are monotonically related. Δx_T in general, however, is a characteristic length, the value of which preserve the knowledge of the soil temperature profiles [176].

5.3 Method and Data

5.3.1 Predigest of Wilheit's T_{eff} Scheme

This subsection reformulates Equation (5.4) with the optical depth ($d\tau$), instead of geometrical depth (dx) with Lv's scheme. In the above sections, we stated that at the soil surface there is a superposition of the intensities emitted at various depths within the soil. In Lv's scheme,

$$\begin{cases} \Delta\tau_i = \Delta x_i \dfrac{2\pi}{\lambda}\dfrac{\varepsilon''}{\sqrt{\varepsilon'}} = \Delta x_i \cdot \alpha(x) & a) \\ \tau_i = \sum_{j=1}^{i} \Delta\tau_j & b) \\ x_i = \sum_{j=1}^{i} \Delta x_j & c) \end{cases} \tag{5.7}$$

According to Equation (5.7a) assuming that the apparent layer is homogenous and is sufficient that the penetration depth Δx_T can be expressed as,

$$\Delta x_T = \frac{\lambda}{2\pi}\cdot\frac{\sqrt{\varepsilon'}}{\varepsilon''} \tag{5.8}$$

The penetration depth does not only indicate the depth where transmitted radiation is reduced to $1/e$ but also the depth where the physical temperature represents the average temperature of that layer when the soil temperature profile is linear. Considering the pre-mentioned assumption that the dielectric and temperature properties of the soil are uniform throughout the emitting layer, this means $\exp\left[-\int_0^x \alpha(x')dx'\right] = e^{-\tau}$ and $\alpha(x)dx = d\tau$. Therefore Equation (5.4) could be simplified as

$$T_{eff} = \int_0^{\infty} T\left[x(\tau)\right]\mathrm{e}^{-\tau}d\tau \tag{5.9}$$

As such, Equation (5.9) can be rewritten by replacing physical depth $x\in[0,\infty)$ with the optical thickness $\tau\in[0,\infty)$ as follows:

$$T_{eff} = \int_0^{\infty} T(\tau)\mathrm{e}^{-\tau}d\tau \tag{5.10}$$

With Equation (5.10), we replace the integral item dx with $d\tau$. τ is also used in the description of radiometry in atmosphere and vegetation and it should also work with soil column. With $d\tau$, T_{eff} becomes concise and convenient for the following analysis.

5.3.2 Characteristic Expression of T_{eff}

For the following derivations, we normalize the soil temperature profile via:

$$T_{inor} = \frac{T_i - T_{surf}}{T_{deep} - T_{surf}} \tag{5.11}$$

where T_{surf} is the soil temperature at the soil surface and T_{deep} the soil temperature at a depth where soil temperature can be considered as constant at inter-annual scales.

What we assume is that soil temperature varies linearly with soil optical depths while it needs T_{deep} at τ_{deep}

$$\begin{cases} T_i = T_{surf} + a\tau_i \quad \left(for\ \tau < \tau_{deep} \right) \\ T_i = T_{surf} + a\tau_{deep} = T_{deep} \quad \left(for\ \tau \geq \tau_{deep} \right) \end{cases} \tag{5.12}$$

where a is the soil temperature gradient with optical depth (unit: K/τ). Assuming e.g. $\tau_{deep} = 5$, the contribution from deeper layers $\tau > 5$ is less than $e^{-5} \approx 0.0067$ which can be neglected. It does not matter where exactly τ_{deep} is as long as it is deep enough and Equation (5.12) is valid. We suggest $\tau_{deep} \geq 5$. According to Equation (5.10), we can calculate the normalized soil temperature:

$$\begin{aligned} T_{inor} &= \frac{T_i - T_{surf}}{T_{deep} - T_{surf}} \\ &= \frac{T_{surf} + a\tau_i - T_{surf}}{T_{surf} + a\tau_{ideep} - T_{surf}} \\ &= \frac{\tau_i}{\tau_{deep}} \quad \left(for\ \tau < \tau_{deep} \right) \end{aligned} \tag{5.13}$$

Put Equation (5.12) in Equation (5.10) leads to

$$\begin{aligned} T_{eff} &= \int_0^{\infty} T(\tau) e^{-\tau} d\tau \\ &= \int_0^{\tau_{deep}} \left(T_{surf} + a\tau \right) e^{-\tau} d\tau + \int_{\tau_{deep}}^{\infty} \left(T_{surf} + a\tau_{deep} \right) e^{-\tau} d\tau \\ &= \int_0^{\tau_{deep}} T_{surf} e^{-\tau} d\tau + \int_0^{\tau_{deep}} a\tau e^{-\tau} d\tau + T_{deep} \int_{\tau_{deep}}^{\infty} e^{-\tau} d\tau \\ &= T_{surf} \left(1 - e^{-\tau_{deep}} \right) + a\left[1 - e^{-\tau_{deep}} \cdot \left(\tau_{deep} + 1 \right) \right] + T_{deep} \cdot e^{-\tau_{deep}} \\ &= T_{surf} + a \qquad \left(if\ e^{-\tau_{deep}} \approx 0 \right) \end{aligned} \tag{5.14}$$

Thus T_{eff} equals the soil temperature at $\tau = 1$, with the linear assumption soil temperature profile, and from Equation (5.13) follows:

$$\frac{T_{eff} - T_{surf}}{T_{deep} - T_{surf}} = \frac{T_{eff} - T_{surf}}{T_{surf} + a\tau_{deep} - T_{surf}} = \frac{T_{surf} + a - T_{surf}}{a\tau_{deep}} = \frac{1}{\tau_{deep}} \tag{5.15}$$

Using $\frac{T_i - T_{surf}}{T_{deep} - T_{surf}}$ to normalize Equation (5.10) on both sides, we get,

$$\begin{aligned}\frac{T_{eff} - T_{surf}}{T_{deep} - T_{surf}} &= \int_0^{\infty} \frac{T - T_{surf}}{T_{deep} - T_{surf}} \mathrm{e}^{-\tau} d\tau \\ &= \int_0^{\infty} T_{nor} e^{-\tau} d\tau \\ &\approx \int_0^{\tau_{deep}} \frac{\tau}{\tau_{deep}} e^{-\tau} d\tau \\ &= \frac{1}{\tau_{deep}} \left[1 - \mathrm{e}^{-\tau_{deep}} \cdot (\tau_{deep} + 1)\right] \\ &\approx \frac{1}{\tau_{deep}}\end{aligned} \tag{5.16}$$

where τ_x is a mark for τ at x. $1-\mathrm{e}^{-\tau_x} \cdot (\tau_x + 1)$ is the characteristic expression for T_{eff} calculation in the linear case because it is not related to the gradient a and τ_{deep}. The term $1-\mathrm{e}^{-\tau_x} \cdot (\tau_x + 1)$ describes the distribution of radiation along τ. Equation (5.16) is an analytic solution for Equations (5.9) and (5.10) with the assumption of a soil temperature profile which is linear in τ above τ_{deep}. It reflects the cumulative energy starting from $1-\mathrm{e}^{-\tau_x} \cdot (\tau_x + 1)\big|_0 = 0$ to deep layer where $1-\mathrm{e}^{-\tau_x} \cdot (\tau_x + 1)\big|_{+\infty} = 1$. Since this distribution is not related to a and τ_{deep}, $1-\mathrm{e}^{-\tau_x} \cdot (\tau_x + 1)$ is universal for all linear cases. Therefore, $T_{eff} \sim \tau \sim x$ relationship (Equations (5.7) and (5.16)) is quantified by $1-\mathrm{e}^{-\tau_x} \cdot (\tau_x + 1)$ which is fundamental if we want to determine $T_b \sim T_{eff} \sim \tau \sim x$ (Equations (5.1), (5.7) and (5.16)) in the future. It is to note that $0 < \tau_x < \tau_{deep}$. Equation (5.16) is based on the assumption that $dT/d\tau$ is constant. Later we use the correlation coefficient (cc) between T and τ along soil profile to estimate this assumption.

5.3.3 *In-Situ* Data, MERRA-2, and SMAP

We use the Maqu network to evaluate the validity of the expressions derived in the previous chapters. The Maqu network is located at the northeast margin of the Tibetan Plateau (Figure 5.1). The average elevation is about 3300 m above the sea level. The network was built in 2008, and continuously provides soil moisture and soil temperature profile information at 20 sites [117]. Since its establishment, the Maqu Network has provided accurate soil moisture and soil temperature measurements for evaluating soil moisture data from satellites [42, 177]. The vegetation cover the network area consists of meadow and grass with heights less than 1 m and rooting depth of tens of centimeters. An accumulated humus layer of around 10 cm is mixed with the soil. Bushes and trees are scarce, while desert dunes appear along the rivers off and on. Besides the 20 sites, a complete land-atmosphere interaction observation site which consists of a boundary layer meteorology tower, an eddy covariance system and two dense soil moisture and soil temperature profile measurements.

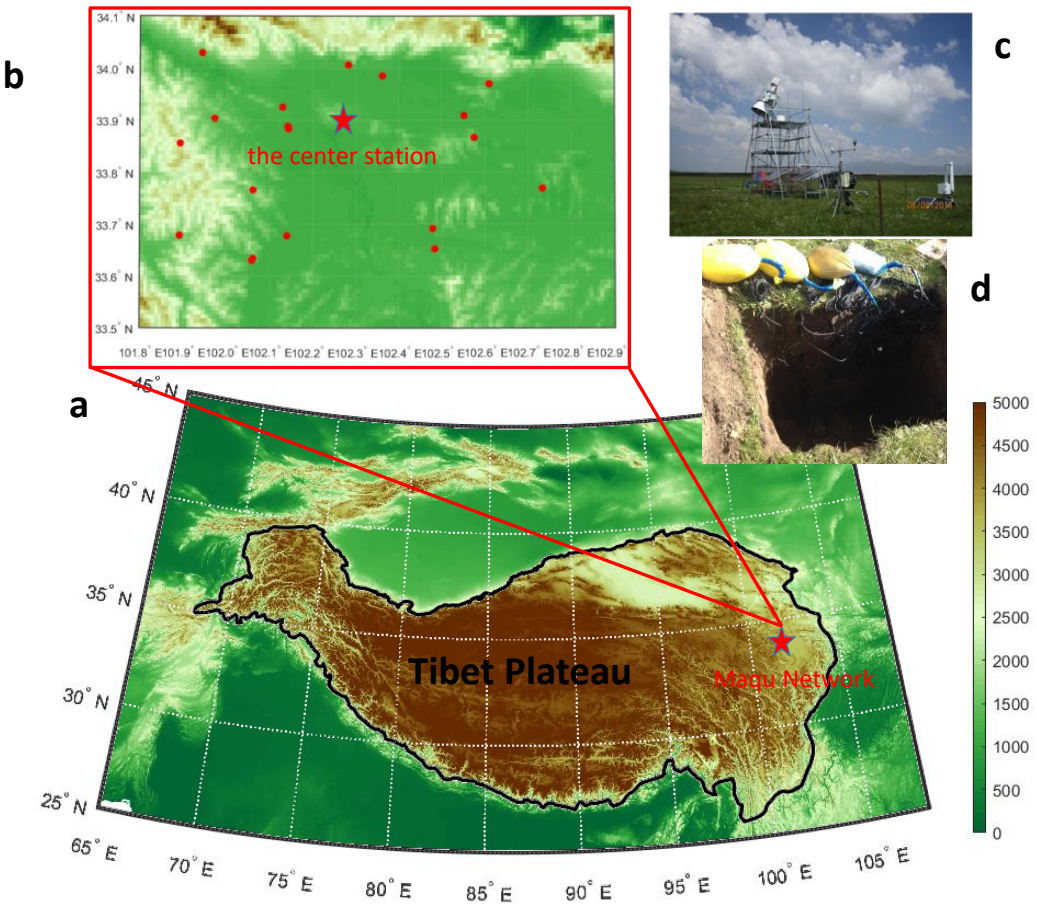

Figure 5.1. (a) Geographical location of the Maqu network on the Tibetan Plateau. The background indicates the elevation from USGS 1 km topography and the border in black is where elevation > 2500 m; (b) The distribution of all sites at the Maqu network and the central site (ELBARA) located in the center; (c) ELABRA; (d) the detailed soil moisture and soil temperature profile.

The vertically densely resulted in soil moisture and soil temperature profile observation at the central station is used in this study (Figures 5.1d and 5.2). The profile data used in this study were measured by ECH20 5TM soil moisture/soil temperature sensors. We use the period from 6 August to 27 November 2016 (Figure 5.2). 20 sensors are installed at 19 layers, with two sensors at 2.5 cm. The depth configuration is illustrated in Figure 5.2d. Soil moisture sensors are calibrated with soil texture, bulk density, and organic matter content. According to soil samples collected near the micro-meteorological observing system, the soil consists of a sand fraction of 26.95% and a clay fraction of 9.86% at 0.05 m while the fractions are 29.2% and 10.15% at 0.2 m, 31.6% and 10.43% at 0.4 m[178]. The layer settings for the other sites of the network are 5 cm, 10 cm, 20 cm, 40 cm, and 80 cm or only 5 cm and 10 cm and an infrared sensor for the skin temperature. Mironov's dielectric constant model was for calculating the real and complex parts of dielectric constants in this study[83].

To extend the understanding of the relationship between soil effective temperature and penetration depth, we also use MERRA-2 (The Modern-Era Retrospective analysis for Research and Applications, Version

2) [179] and the SMAP Level 3 global daily 36 km EASE-Grid soil moisture, Version 4 product in this study. MERRA-2 is supposed to replace former the MERRA dataset with the advances made in the assimilation system that enable the assimilation of hyperspectral radiance and microwave observations, along with GPS-Radio Occultation datasets. The spatial resolution used in this study is 0.625 × 0.5 degree. While soil properties are retrieved from the MERRA-2 constant fields, soil temperature, soil moisture and surface temperature at SMAP overpassing time are collected globally during the year of 2016. Since March 2015, SMAP is providing the global soil moisture distribution [44]. The spatial resolution for the passive sensor is 36 km that is double the resolution of MERRA-2. Thus, the SMAP L3 product is downscaled with the nearest neighbor interpolation method to construct soil moisture maps matching MERRA-2. In this study, the in situ soil moisture and soil temperature data at Maqu Center Station were used to directly compute the T_{eff} and penetration depth within the soil column, and vegetation effects are assumed to be negligible. In the SMAP soil moisture product, the impact of vegetation is accounted for in retrieval procedure. The SMAP soil moisture product is derived from an average emissivity with the soil moisture at fixed depth is not the same as the average soil moisture.

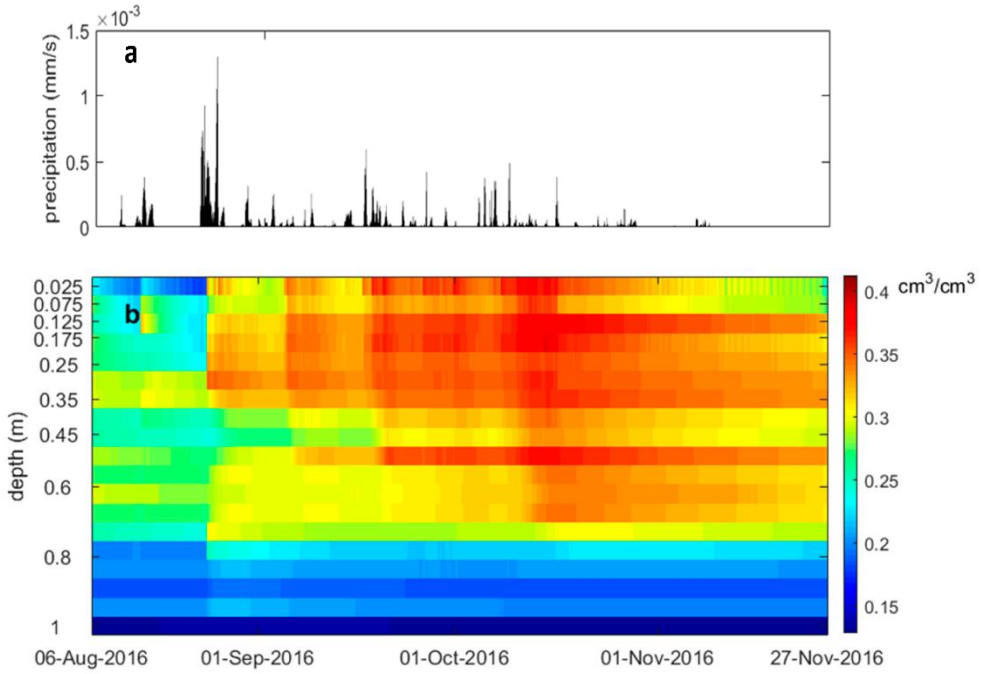

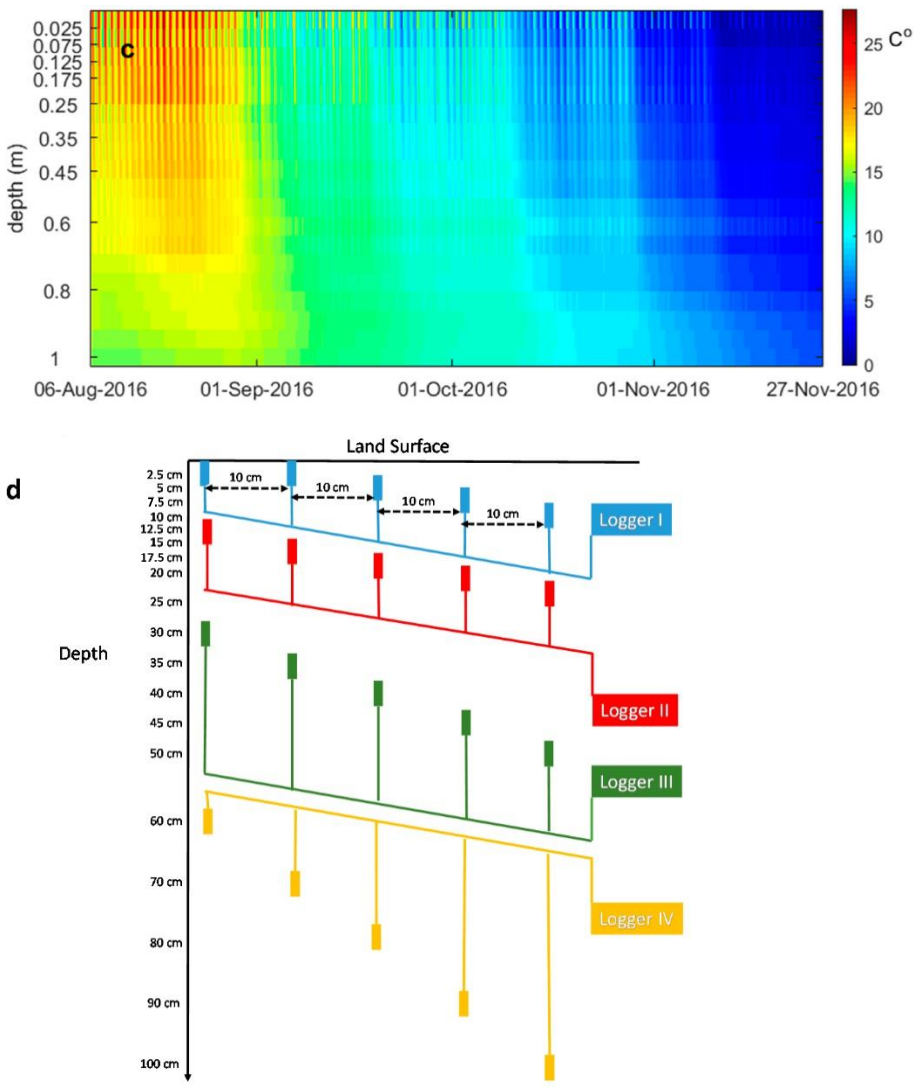

Figure 5.2. (a) precipitation; (b) the time series of soil moisture and (c) soil temperature profiles at Maqu Network Center Station; (d) the installation configuration of 20 sensors.

5.4 Results

In this section, the penetration depth is first calculated according to Equation (5.8) for 1.4 GHz to give a broad view of how penetration depth is affected by soil moisture and soil temperature. After that, Equation (5.6) and Equation (5.9) are applied to the observation of the Maqu Center Station to derive penetration depth time series. Finally, we compare the soil temperature at the penetration depths with the soil effective temperature following Equation (5.10).

Figure 5.3 showsobserving the effect of the soil moisture and soil temperature on the penetration depth. Soil moisture is the dominant factor when the soil is dry, while soil temperature has always impact on the penetration depth of wet soil. Over the range of soil moisture of 0.01–0.6 cm^3 cm^{-3} and soil

temperatures of 0–60 °C, the penetration depth ranges from 3–70 cm. When the soil is very dry (i.e., soil moisture is less than 0.01 $cm^3\ cm^{-3}$), the penetration depth is the greatest. The penetration depth is 12 cm at 0.3 $cm^3\ cm^{-3}$ and 30 °C. The penetration depth could be 11 cm as soil moisture 0.55 $cm^3\ cm^{-3}$ and soil temperature is 50 °C, but the same depth is found for soil moisture of 0.2 $cm^3\ cm^{-3}$ and soil temperature of 10 °C. For any soil, the penetration depth strongly depends on the dielectric constant model, but the difference can be ignored because the gradient of penetration depth in Figure 5.3 would follow the soil moisture mainly.

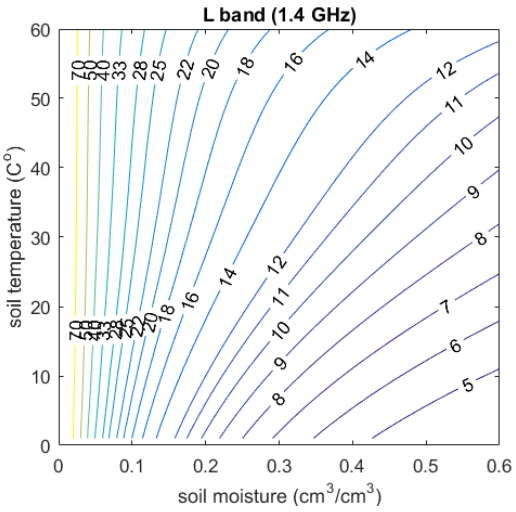

Figure 5.3. Penetration depth at L band (1.4 GHz) in centimeters shown as contour lines, depending on the soil moisture and soil temperature. Mironov's dielectric constant model was used for calculating the real and complex parts of dielectric constants.

Figure 5.4 shows the time series of the penetration depth (blue) and the correlation coefficient (red) between soil temperature at penetration depth and the soil effective temperature. While soil moisture ranges from 0.15 to 0.45 $cm^3\ cm^{-3}$, the penetration depth varies from 6 to 10 cm at the center site. The average penetration depth is about 9 cm for the time before August 25 and 7 cm for the rest. The variation of soil moisture in Figure 5.2, as well as the time series of penetration depth in Figure 5.4 are strongly correlated. The soil moisture explains the variation of penetration depth in the period. The penetration depth has a diurnal change of about 2 cm, and this diurnal variation is affected dominantly by soil temperature according to Equation (5.8).

From the preceding, we highlighted the essence of T_{eff} as the soil temperature ($d\tau = 1$) which may represent the average soil temperature of the soil column influencing. Soil moisture detected by satellites is also assumed to be the average soil moisture of the soil column in the range of the emission depth. With T_{eff} computed from MERRA-2 and global soil moisture map acquired from SMAP, Figure 5.5 illustrates a global distribution of the estimated penetration depth by Equation (5.8).

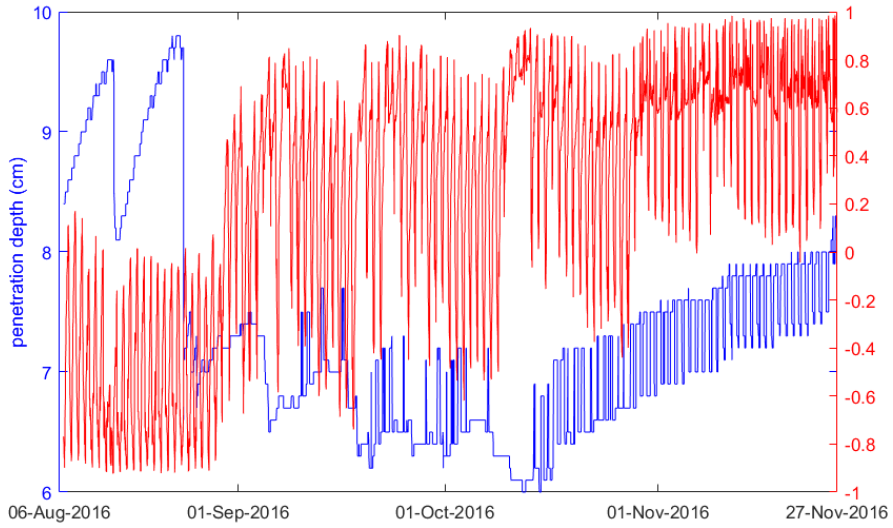

Figure 5.4. The time series of the estimated penetration depth (blue) and the correlation coefficient between the soil temperature profile and soil optical depth profile (red) at Maqu Center Station as computed from the soil temperature/moisture profiles between 6 August and 27 November 2016.

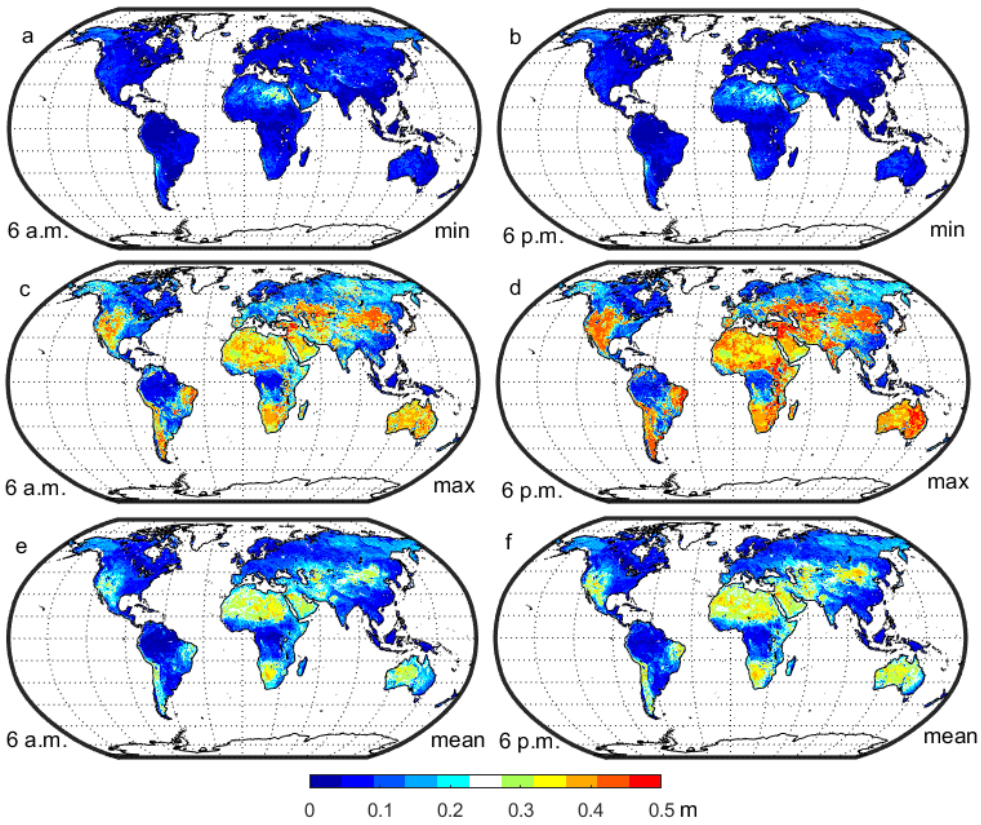

Figure 5.5. Global map of the penetration depth (PD) for SMAP with (a) minimum at 6 a.m.; (b) minimum at 6 p.m.; (c) maximum at 6 a.m.; (d) maximum at 6 p.m.; (e) mean at 6 a.m.; (f) mean at 6 p.m. Data used are SMAP soil moisture passive L3 product and the corresponding soil effective temperature calculated from

MERRA-2 for 2016. The SMAP soil moisture and soil effective temperature are considered as the mid-level values for each pixel vertically.

The minimum penetration depths (Figure 5.5a,b) are especially observed after rainfall event when the upper-layer soil moisture is high. Maximum penetration depths (Figure 5.5c,d) occur after a long drying period are found in arid regions like central Asia, Australia, and Sahara where the penetration depth can be deeper than 0.3 m. The annual mean penetration depth (Figure 5.5e,f) ranges from 0.05 to 0.2 m except for extremely dry regions. The SMAP soil moisture and soil effective temperature are considered as the mid-level values for each pixel vertically. The soil moisture/temperature sampled at 0.05 m represents the radiative contribution from 0 m to more than 0.1 m (depending on the specific profile), so 0.05 m samples may match with the satellite signal in most regions. In general, the 6 a.m. and 6 p.m. sampling depths do not differ much while the latter may be deeper by a few centimeters because T_{eff} is higher (Figure 5.3).

5.5 Discussion

Because the penetration depth is defined as the depth at which the intensity of transmitted inside a medium reduces to about 37% of the signal comes from beneath it. Several factors influence the penetration depth and due to its diurnal variations. Cal/Val efforts require the knowledge of the overpassing time. Equations (5.10) and (5.16) are known derived based on the assumption, $\frac{dT}{d\tau} = const$ are the depth influencing T_{eff} . If the soil temperature profiles are more complex, T_{eff} will have errors and the estimated the remotely sensed soil moisture would also have layer error.

The absolute value of the correlation coefficient $|cc|$ between the soil temperature profile and the optical depth profile at Maqu Center Station quantifies the validity of the $\frac{dT}{d\tau}$ assumption (Figure 5.6). $|cc| > 0.8$ occurs only during 10.89% of the observations and mainly around 10:00 o'clock (local time) at about 40% of the observation period. Another time with high correlation occurs at about 18:00 o'clock (local time) which coincides with SMOS/SMAP descending/ascending overpassing times repeatedly. From above, we conclude that the linear assumption concerning the soil temperature profile ($\frac{dT}{d\tau}$ = constant) is most not valid but only in few times.

The soil temperature at the penetration depth allowed a good estimate of the soil effective temperature. The soil temperature observed at 5 cm, 10 cm, 40 cm and of the penetration depth is compared with the soil effective temperature calculated by Wilheit's scheme in Figure 5.7. The soil temperature at 2.5 cm (Figure 5.7a) has a slight negative bias and a large scatter than the temperature at the penetration depth (Figure 5.7d). For the soil temperature between 15 and 20 °C, differences can reach 5 °C. The soil temperature at 10 cm (Figure 5.7b) matches better with 1:1, but is still worse than at penetration depth. From Figure 5.4, it is known that the average penetration depth is about 7 cm after 20 August. Therefore

the relatively similar accuracy is reasonable between Figure 5.7b,d. RMSE reaches 3.3°C. 40 cm cannot represent the soil profile (Figure 5.7c) to calculate T_{eff} .

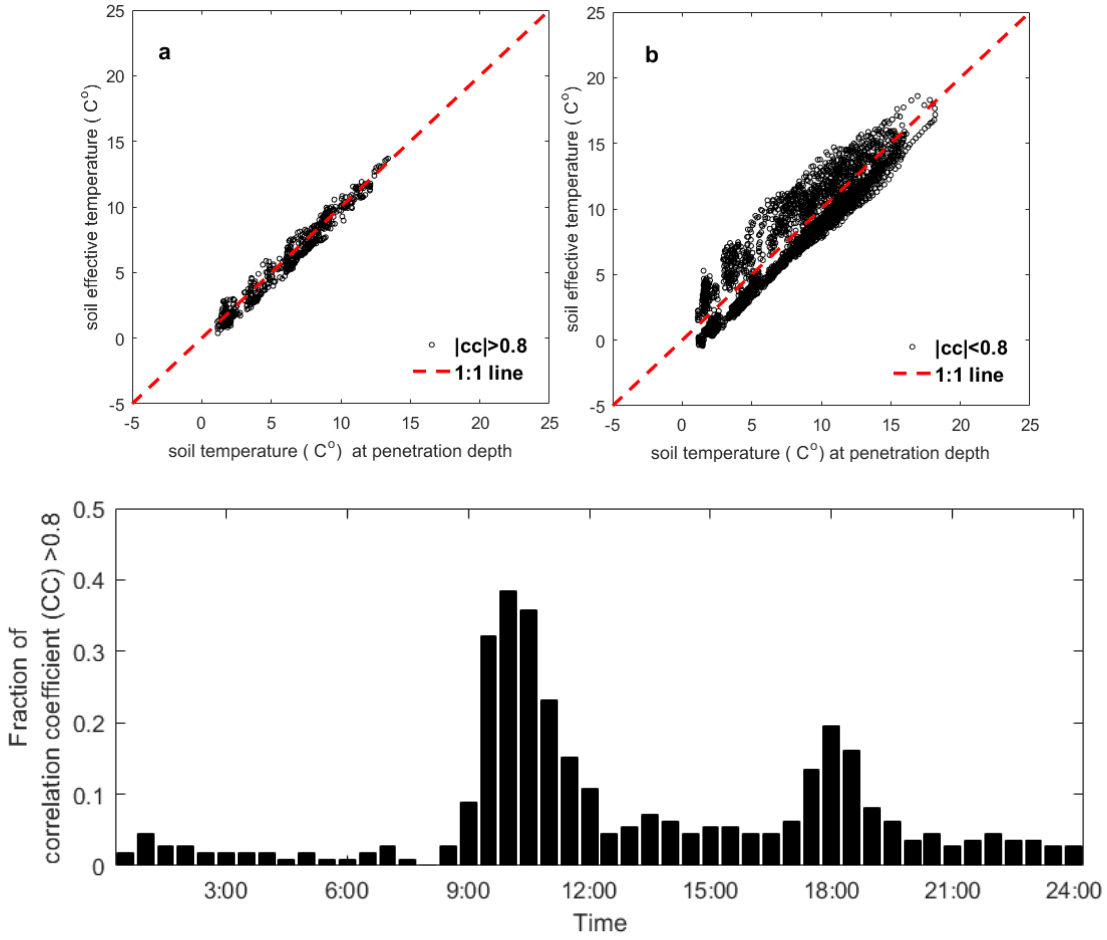

Figure 5.6. Comparison of soil temperature at the penetration depth vs. soil effective temperature at Maqu Center Station for a percentage of cases with $|cc| > 0.8$ (a) and $|cc| < 0.8$ (b). The bottom figure shows the daily distribution of the moment when the correlation coefficient $|cc| > 0.8$.

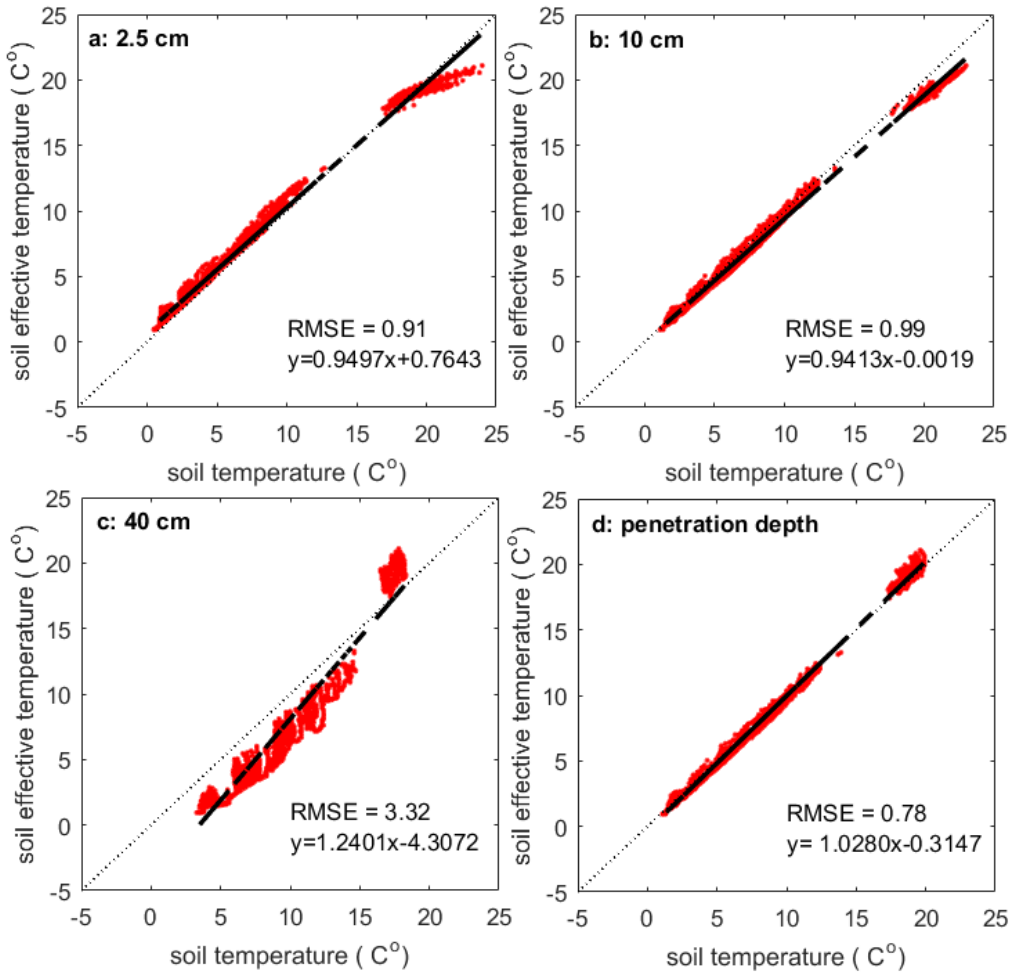

Figure 5.7. Comparison of soil effective temperature calculated by Wilheit's integral scheme against soil temperature observed at Maqu Center Station: (a) 2.5 cm; (b) 10 cm; (c) 40 cm observation and (d) the penetration depth. Data are shown only when $|cc| > 0.8$ and the dashed line is the regression line. The period is from 6 August to 27 November 2016.

5.6 Conclusions

The concept of penetration depth in microwave radiometry was published more than four decades ago, and its knowledge becomes especially important with the longer wavelengths of the dedicated soil moisture missions SMOS/SMAP. The soil temperature at penetration depth is only related to the case when the soil temperature changes linearly with soil optical depth τ, and only then a two-layer soil model can capture it. This link with satellite soil moisture sensing depth has not been determined yet.

We have proved that the penetration depth is emitting behavior of a soil column in microwave radiometry. The optical depth τ appears in T_{eff} and thus unifies the radiative transfer processes in the atmosphere, vegetation, and soil. τ quantifies the attenuation of radiation transfer in a medium, being the air dielectric properties in the atmosphere, vegetation optical thickness (mainly the water content in leaves)

in vegetation, as well as soil dielectric properties (e.g., mainly soil moisture) in the soil. The use of τ instead of soil geometric depth x is proposed in this study for the first time, and with τ appearing in T_{eff}. Using τ, it is proved that the penetration is not just the depth where the energy is reduced to 1/*e* of its original value, but it is also the median value of soil temperature in the soil column in the linear profile. The penetration depth is strongly related to soil moisture and has a diurnal variation which may have an amplitude of several centimeters.

The question of at which depth L-band soil moisture monitoring satellites such as SMOS/SMAP measure has confused the soil moisture community at large. As stated in the introduction, the sensitive layer is supposed to be the depth where these satellites are sensing in previous studies. In SMAP retrievals [180], vegetation and soil surface roughness are accounted regarding soil moisture calibration. The final soil moisture product is derived from a smooth emission model. A precise estimation of vegetation and roughness is critical before determining the penetration depth. Particularly, the global map of penetration depth in Figure 5.5 depends on a correct vegetation calibration. Therefore, the penetration depth over dense vegetation zone, for instance, the tropics may be even smaller. In contrast, in the desert area with few or no vegetation, the penetration depth is usually large, and vegetation calibration is not so important except after rainfall events. The conclusion in this study would be most useful to the transition zone where soil moisture variation is larger and affects climate/hydro-process more intensively. Different to the view that considers soil moisture sensitive layer in emissivity, we proposed in this study a median value view and found the soil temperature median value under the linear assumption. From the hypothesis of zeroth-order incoherent microwave transfer frame, the median soil temperature layer represents not only T_{eff} but also provides the depth information contained in this frame. The soil moisture retrieved from microwave (e.g., L-band) observation should be the average radiative emission capacity of the soil column, and there should be a median soil moisture depth as well. This study has successfully developed such a new method to find this median soil moisture depth by relating the penetrating depth regarding temperature to radiative energy attenuation. This is done by building up a $T_b \sim T_{eff} \sim \tau \sim depth$ relationship with median theory in which a median value of T could be found at the penetration depth with a certain condition. The method is verified with in situ data from the Maqu observation site, and the conclusion is valid whenever the field condition satisfies the assumption. This is critical to the application of SMOS/SMAP soil moisture product because a difference of several centimeters between the depth of in situ measurement and the satellite sensing depth will lead to systematic bias in evaluating the satellite products. Based on an application of the developed method to SMAP passive L3 soil moisture product and the corresponding soil effective temperature calculated from MERRA-2 for 2016, it may be concluded that it is appropriate to use 5 cm depth of soil moisture measurement as a ground reference to calibrate and validate satellites soil moisture product because 5 cm captures the main signal source on average. However, for some extreme cases like arid region or the region after a long drought event, 5 cm may not represent the dominant emission layer. In other words, it means that even though the satellite product is precise, we may still get a biased conclusion, if the ground measurement is inappropriately organized, and the comparability between

satellite and in situ measurement is not established [181]. The developed method should also be beneficial to the Earth surface modeling in improving the consistency in the dynamics of the soil moisture processes and satellite observations.

Chapter

6 A Closed-form Expression of Soil Temperature Sensing Depth at L-band[5]

Abstract: L-band passive microwave remote sensing is one of the most effective methods to map the global soil moisture distribution, yet, at which soil depth satellites are measuring is still inconclusive. Recently, with the Lv's multilayer soil effective temperature scheme, such depth information can be revealed in the framework of the zeroth-order incoherent model when soil temperature varies linearly with soil optical depth. In this study, we examine the relationships between soil temperature microwave sensing depth, penetration depth and soil effective temperature, considering the nonlinear case. The soil temperature sensing depth often also named penetration depth, is redefined as the depth where soil temperature equals the soil effective temperature. A method is developed to estimate soil temperature sensing depth from one pair of soil temperature and moisture measurement at an arbitrary depth, the soil surface temperature, and the deep soil temperature which is assumed to be constant in time. The method can be used to estimate the soil effective temperature and soil temperature sensing depth.

Keywords: Microwave Remote Sensing; Soil Temperature Sensing Depth; Penetration Depth; Soil Optical Depth; Soil Effective Temperature

[5] This chapter is based on

Shaoning Lv, Yijian Zeng, Jun Wen, Zhongbo Su. 2018. A Closed-form Expression on Optical Depth and Soil Effective Temperature. IEEE Transactions on Geoscience and Remote Sensing; doi: 10.1109/TGRS.2019.2893687.

6.1 Introduction

Soil moisture strongly impact the energy and water balance over the land since the heat capacity of wet soil is larger than that of dry soil, more heat energy can be stored in wet soil. On the other hand, soil moisture can be transferred into water vapor and thus latent heat, which can be transferred to the atmosphere by evaporation. This feature makes soil moisture a key variable for the weather forecasting, climate, and agriculture. Many devices exist which measure soil moisture either locally or at the regional scale. L-band microwave remote sensing is recognized as the most promising tool for mapping the regional and global soil moisture distribution [24, 40, 43, 60] because of the strong relation between soil emissivity and soil moisture at this frequency. Soil heterogeneity, however, make this relation uncurtains. Since the 1970s, the effects of dielectric constant, vegetation, and soil roughness, on the observed signal has been studied, Radio Frequency Interference (RFI) and others [182].

The zeroth-order incoherent model is currently the theoretical basis for soil moisture retrieval at L-band, which states that the observed brightness temperature T_B can be written as $T_B = \varepsilon T_{eff}$ with ε soil emissivity and T_{eff} as effective soil temperature. However, only a few studies work on the soil depth to which one T_{eff} referred to. In forward simulations, emissivity is often assumed as the emissivity of the upper layer, while no explicated depth is attributed to that layer. Similarly, calibrations/validations usually soil moisture measurement at a fixed layer is used. Such fixed soil moisture depth, however, does not reflect the dynamics and status of dielectric profiles. In reality, soil moisture gradients can be very sharp especially after the rainfall. Neglecting such effects will cause uncertainties of soil moisture retrievals with errors caused by roughness and vegetation [64].

Escorihuela et al. (2010) defined the moisture sensing depth as the soil moisture layer, which has the highest correlation coefficient with T_b [65]. Since the near surface layers usually contribute most to the emission, its soil moisture is mostly used to compute the emissivity in radiative transfer models. Zhou et al. [63] claimed that the attenuation of radiation by the soil is too weak to evoke noticeable effects. But, without a clear definition of moisture and temperature sensing depths, it is difficult to quantify the relationship between T_b and soil moisture including its effective depth.

Usually, the microwave penetration depth is assumed to be equal to the soil temperature sensing depth, i.e., the depth at which impinging radiation is reduced to $1/e$ [62]. In this study, we revisited these concepts of penetration depth and soil temperature sensing depth. The incoherent model reads

$$T_b = \varepsilon T_{eff} \tag{6.1}$$

where T_b is the brightness temperature detected by the radiometer and ε is the soil bulk emissivity which is strongly related to the soil moisture, since its dielectric constant varies from 3 to 80 at L-band. The zeroth-order incoherent model is an approximation of the coherent model thus the zeroth-order incoherent model, and coherent model should lead to the same results if one can find the effect soil temperature and effective

soil moisture for the non-uniform soil moisture and temperature profiles. is a virtual concept and cannot be directly observed but is required to determine the effective emissivity of a soil layer. In the coherent model, reflectivity and absorption are calculated for each layer and thus does not require T_{eff} .

Based on the zeroth-order incoherent model, only one soil moisture value can be retrieved from the brightness temperature, while T_{eff} needs to consider the effects of soil moisture/temperature gradients. Thus soil moisture derived from ε cannot be simply attributed to a specific depth. Thus only T_{eff} is associated with depth and is the parameter in incoherent models for understanding satellite sensing depth.

The calculation of T_{eff} from its integral formula requires the accurate knowledge of both the profiles of temperature and soil moisture (Wilheit, 1978). The accuracy also depends on the precision of the dielectric constant model which contains soil moisture and soil temperature to permittivity (the real part) and attenuation (the imaginary part). In practice, these details are neither known in land surface models which assume uniform soil moisture/temperature values within each layer, nor in used field observations. Choudhury et al. (1982) developed a simplified form of the integral formula which requires only the surface temperature (0~2 cm) and the deep soil temperature (~80 cm) besides a constant *C* which depends on wavelength and was determined from laboratory experiment [86]. Choudhury's scheme proved to work well for C-band (6.9 GHz) but not for L-band (1.4 GHz), the wavelength used by the SMOS and SMAP satellite. Another two schemes were proposed by Wigneron, 2001 and Holmes, 2006 with more specific parameterization of "*C*" [80, 87]. All these schemes are semi-empirical based on particular experiment datasets. Lv et al. (2014) developed a new T_{eff} scheme (Lv's scheme hereafter) which preserves most of the physics without semi-empirical parameters [127]. The scheme gives a physical interpretation of the parameter C and bridges the gap between the two-layer and the integral schemes by accounting for multi-layer soil moisture/temperature information[127]. The scheme can also be used to T_{eff} consistency checks between *in-situ* observation at different depths and SMOS/SMAP observation, by evaluating the contributions from different soil layers. As such, all sorts of specific depth configurations of land surface model or non-uniform field observations can be used in the Lv's scheme [175]. With the scheme, also the relationship between soil moisture and soil temperature profiles can be explored with just a few sampling points along the depth. In the previous study, we proved that the soil temperature at the penetration depth is equal to T_{eff} when the soil temperature varies linearly with soil optical depth[183]. Here we will first review this linear assumption and infer the soil optical depth-soil temperature relationship for non-linear cases. A semi-empirical model of soil temperature-soil optical depth scheme is developed and tested against *in-situ* observation at the Maqu network over Tibetan Plateau (Su et al., 2011).

6.2 Methodology and data

6.2.1 Soil Optical Depth and Soil Effective Temperature

Here we explore the relationship between penetration depth, soil temperature sensing depth and T_{eff} . Section 6.2.1 introduces how the soil geometric depth can be expressed as $1-e^{-\tau}$ with τ the soil optical depth. In Section 6.2.3 we express that the soil temperature profile $T(x)$ as a normalized soil temperature profile $\Delta T_{nor}(\tau)$ with soil optical depth as coordinate. While Chapter 5 presents a soil temperature sensing depth estimation method for soil temperature profiles linear in τ , its extension to the non-linear case is discovered in Section 6.2.4. All variables used in this study are summarized in Table 6.1.

Table 6.1. Variables used in this study.

Abbreviation	Definition	Unit	Expression
B	The former parameter in Lv's scheme and is replaced by τ	-	See Lv et al., 2014
T_{eff}	soil effective temperature	K	
T_b	brightness temperature	K	
θ	soil moisture	Vol/Vol	
$x_{1-e^{-\tau}}$	x-axis with $t=1-e^{-\tau}$	-	Equation (6.3)
y_{nst}	y-axis with the normalized soil temperature	-	Equation (6.4)
$T(t)$	soil temperature at $y_{nst}-x_{1-e^{-\tau}}$ coordinate where $t=1-e^{-\tau}$	K	
$T(\tau)$	soil temperature at soil optical depth τ	K	
$T(x)$	soil temperature at geometric soil depth x	K	
$\Delta T_{nor}(\tau)$	Normalized soil temperature at soil optical depth τ	-	Equation (6.4)
$\Delta T_{nor}(t)$	Normalized soil temperature in the $y_{nst}-x_{1-e^{-\tau}}$ coordinate where $t=1-e^{-\tau}$	-	
T_{surf}	skin temperature	K	
T_{deep}	soil temperature at a deep layer that the soil temperature could be considered as constant	K	
a	Soil temperature gradient	K/τ	$a=dT/d\tau$
$\alpha(x)$	attenuation parameter	-	$\alpha(x)=\frac{4\pi}{\lambda}\varepsilon''(x)\Big/2\left[\varepsilon'(x)\right]^{\frac{1}{2}}$
τ_{deep}	τ deep enough that the soil temperature could be considered as constant	-	
b	The parameter to adjusting Equation (6.13) and Equation (6.12) to cases in Figure 6.2	-	Equation (6.15)
τ_{Teff}	Soil temperature sensing depth	-	Equation (6.17)

6.2.2 Formulation of T_{eff} in soil optical depth and transmitting

T_{eff} can be understood as a superposition of the intensities emitted at various depths within the soil. $T_{eff} = \int_0^{\infty} T(x)\alpha(x)\exp\left[-\int_0^{x}\alpha(x')dx'\right]dx$ with α the volume absorption coefficient of the soil. Assuming a layered soil $\alpha(x)$. Δx is the optical depth $\Delta\tau$ of the particular layer for which holds $\Delta\tau = \Delta x \cdot \alpha(x)$ (See Equation (5.7)), $\Delta x = \frac{2\pi}{\lambda}\frac{\varepsilon''}{\sqrt{\varepsilon'}}$ and $\exp\left[-\int_0^{x}\alpha(x')dx'\right] = e^{-\tau}$. Thus T_{eff} can be rewritten as

$$T_{eff} = \int_0^{\infty} T\left[x(\tau)\right]\mathrm{e}^{-\tau}d\tau = \int_0^{+\infty} T(\tau)e^{-\tau}d\tau \tag{6.2}$$

where τ increases with soil depth. With both soil depth and τ between $[0,+\infty)$, we can define $t = 1-e^{-\tau}$ $\in [0,1)$, and further rewrite the equation to

$$T_{eff} = \int_0^1 T(t)dt \tag{6.3}$$

6.2.3 Normalization of the soil temperature profile

If we know the surface temperature T_{surf} (e.g., from infrared observations) and the deep soil temperature T_{deep} (e.g., from climatology), the profile T can be expressed by

$$T_{nor}(\tau) = \frac{T(\tau) - T_{surf}}{T_{deep} - T_{surf}} \tag{6.4}$$

$T_{nor}(\tau)$ varies from 0 to 1 from the surface to the deep soil. $1-e^{-\tau}$, T_{eff} and τ strongly depends on the soil moisture profile but also the temperature profile. The impact of soil temperature on τ dominates in arid and semi-arid areas, where the change of soil moisture is tightly coupled with soil heat dynamics [129, 130, 184, 185]. By $\tau = \int_0^{x}\frac{2\pi}{\lambda}\frac{\varepsilon''}{\sqrt{\varepsilon'}}dx$, τ is related to physical depth and soil moisture and varies monotonously along the soil profile. Figure 6.1 shows six typical soil temperature and soil moisture profiles [90]. The soil temperature profiles 1-4 and 6 represent stages during diurnal heating and cooling. Profile 5 was chosen to investigate the sensitivity of T_{eff} to subsurface temperature anomalies such as occurred in areas of geothermal activities [90]. Only Case 3 and Case 4 are not monotonous, but their vertical average soil temperature variation (not gradient) is relatively small, and similar effects to the uniform soil temperature profile Case 4, and measurement at any depth x could be used without layer errors any formulator for T_{eff}.

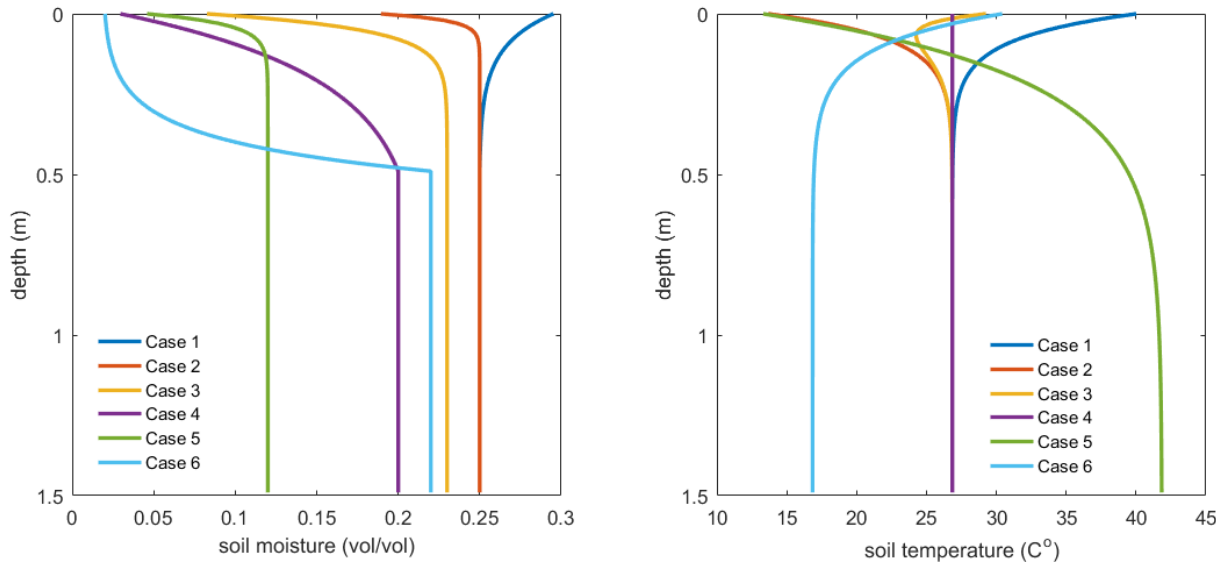

Figure 6.1 Six typical soil moisture (left) and soil temperature profiles (right). Therefore, it is possible to create 36 dielectric profiles where $\varepsilon = f(\theta, T)$ with different soil temperature/moisture combinations.

Figure 6.1 shows a range of potential soil temperature and soil moisture profile types under different hydrothermal soil conditions. Soil moisture profile 1 may occur during rain. Profiles 2-5 can represent stages of soil surface drying out for different soil types. Profile 6 simulates a possible moisture profile in the presence of a water table at a depth of 0.5 m [90].

Figure 6.2 shows the profiles of the normalized temperature T_{nor} plotted against t for all combinations of soil temperature and moisture profiles. Except for temperature profile 3, all curves show similar behavior. Thus we may further simplify them by a common parameterization. Besides the profiles in Figure 6.1, we will use a soil temperature profile linear in τ as a reference that is indicated by the green line in Figure 6.2 to derive an expression for non-linear cases.

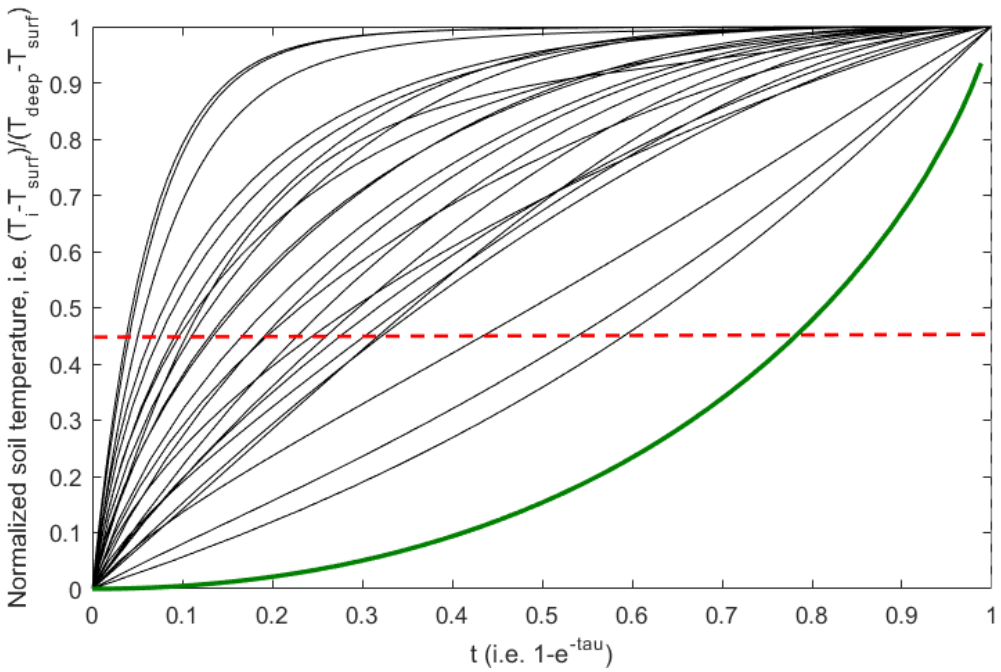

Figure 6.2 Normalized soil temperature/moisture profile combination against $t = 1 - e^{-\tau}$. The solid lines indicate all profiles combinations except soil temperature profile 3. The green line is drawn from Equation(6.13) for a constant $\frac{dT}{d\tau}$ (i.e. the linear case).

The soil temperature profile linear in τ can be expressed as

$$\begin{cases} T(\tau) = T_{surf} + a\tau \quad (\tau < \tau_{deep}) \\ T(\tau) = T_{surf} + a\tau_{deep} = T_{deep} \quad (\tau \geq \tau_{deep}) \end{cases} \tag{6.5}$$

where $\frac{dT}{d\tau} = a$ a constant. Transformed in the normalized temperature profile T_{nor} leads to

$$\begin{aligned} T_{nor}(\tau) &= \frac{T(\tau) - T_{surf}}{T_{deep} - T_{surf}} \\ &= \frac{T_{surf} + a\tau - T_{surf}}{T_{surf} + a\tau_{deep} - T_{surf}} \\ &= \frac{\tau}{\tau_{deep}} \quad (\tau < \tau_{deep}) \end{aligned} \tag{6.6}$$

Inserting Equation (6.5) & (6.6) in Equation (6.2) leads to

$$
\begin{aligned}
T_{eff} &= \int_0^{\infty} T(\tau) e^{-\tau} d\tau \\
&= \int_0^{\tau_{deep}} \left(T_{surf} + a\tau\right) e^{-\tau} d\tau + \int_{\tau_{deep}}^{\infty} \left(T_{surf} + a\tau_{deep}\right) e^{-\tau} d\tau \\
&= \int_0^{\tau_{deep}} T_{surf} e^{-\tau} d\tau + \int_0^{\tau_{deep}} a\tau e^{-\tau} d\tau + \left(T_{surf} + a\tau_{deep}\right) \int_{\tau_{deep}}^{\infty} e^{-\tau} d\tau \\
&= T_{surf} \left(1 - e^{-\tau_{deep}}\right) + a\left[1 - e^{-\tau_{deep}} \cdot \left(\tau_{deep} + 1\right)\right] + \left(T_{surf} + a\tau_{deep}\right) \cdot e^{-\tau_{deep}} \\
&= T_{surf} + a \left(e^{-\tau_{deep}} \approx 0\right)
\end{aligned}
\tag{6.7}
$$

Hence, $T_{eff} = T_{surf} + a$ equals the soil temperature at $\tau = 1$ for soil temperature profiles varying linearly in τ. Thus the soil temperature at the penetration depth equals T_{eff} for the linear case. Normalizing the left side of Equation (6.7) using Equation (6.5) and (6.6), we get:

$$
\frac{T_{eff} - T_{surf}}{T_{surf} + a\tau_{deep} - T_{surf}} = \frac{T_{surf} + a - T_{surf}}{a\tau_{deep}} = \frac{1}{\tau_{deep}} \tag{6.8}
$$

Another way to get the above results is to normalize both sides of Equation (6.3), we have

$$
\begin{aligned}
\frac{T_{eff} - T_{surf}}{T_{deep} - T_{surf}} &= \int_0^{\infty} \frac{T - T_{surf}}{T_{deep} - T_{surf}} \mathrm{e}^{-\tau} d\tau \\
&= \int_0^{\infty} \Delta T_{nor}(\tau) e^{-\tau} d\tau \\
&= \int_0^{\infty} \frac{\tau}{\tau_{deep}} e^{-\tau} d\tau \\
&= \frac{1}{\tau_{deep}} \left[1 - \mathrm{e}^{-\tau} \cdot (\tau + 1)\right] \Big| \qquad for\ \tau \to \infty \\
&= \frac{1}{\tau_{deep}}
\end{aligned}
\tag{6.9}
$$

It means we need to find a τ value to satisfy $T_{nor}(\tau) = \frac{T_{eff} - T_{surf}}{T_{deep} - T_{surf}}$. The linear assumption for the soil temperature profile, i.e. $T_{nor}(\tau) = \frac{\tau}{\tau_{deep}}$, is, of course, valid only to a depth, when T approximately reaches the climatological deep soil temperature, T_{deep}. We approximate soil temperature profile by adding an exponential decay term to the linear assumption, i.e. $a \to ae^{-\tau}$. Thus, we start with a linear T profile near the surface, which decay gradually to a constant T profile with depth,

$$
T(\tau) = \int_0^{\tau} \left(T_{surf} + ae^{-\tau}\tau\right) d\tau \tag{6.10}
$$

So Equation (6.6) turns to be,

$$\begin{aligned}\Delta T_{nor}(\tau) &= \frac{T(\tau)-T_{surf}}{T_{deep}-T_{surf}} \\ &= \frac{\int_0^{\tau_x}\left(T_{surf}+ae^{-\tau}\tau-T_{surf}\right)d\tau}{\int_0^{\tau_{deep}}\left(T_{surf}+ae^{-\tau}\tau-T_{surf}\right)d\tau} \\ &= \frac{\int_0^{\tau_x}e^{-\tau}\tau d\tau}{\int_0^{\tau_{deep}}e^{-\tau}\tau d\tau}\ \left(\tau<\tau_{deep}\right)\end{aligned} \tag{6.11}$$

Equation (6.11) is a dummy format of the linear assumption in Equation (6.6). Because $\int_0^{\tau_{deep}} e^{-\tau}\tau d\tau = 1$, then we create a formula,

$$T_{nor}(\tau) = 1-\mathrm{e}^{-\tau_x}\cdot(\tau_x+1) \tag{6.12}$$

then if we use $t = 1-e^{-\tau_x}$ to replace τ_x and let $1-\mathrm{e}^{-\tau_{deep}} \approx 1$, Equation (6.12) turns into

$$T_{nor}(t) = 1-(1-t)\cdot\left(-\ln(1-t)+1\right) \tag{6.13}$$

Equation (6.13) is actually plotted as the green line in Figure 6.2.

6.2.4 T_{eff} features in a $y_{nst}-x_{1-e^{-\tau}}$ coordinate: the nonlinear case

Equation (6.12) is a linear case and all other 24 nonlinear cases could be expressed with adding just one parameter as,

$$T_{nor}(t) = 1-(1-t)^{b}\cdot\left(-\ln(1-t)+1\right) \tag{6.14}$$

The values of b corresponds to ΔT_{nor} almost one by one because there are rare crossing points in Figure 6.2 among these curves.

$$b = \ln_{e^{-\tau}}\frac{1-\Delta T_{nor}(\tau)}{\tau+1} = -\frac{1}{\tau}\ln\frac{1-\Delta T_{nor}(\tau)}{\tau+1} \tag{6.15}$$

The curve fitting is not shown and hereafter we will prove its efficiency from its inference (Figure 6.2). Now, it is possible to infer T_{eff} and the depth (τ) with $T(\tau) = T_{eff}$ once we know a pair of $(t, \Delta T_{nor})$ or $(\tau, \Delta T_{nor})$ because

$$\begin{aligned}T_{eff} &= \int_0^{\tau_x} T(\tau)e^{-\tau}d\tau \\ &= \int_0^{\tau_x}\left[\left(T_{deep}-T_{surf}\right)\cdot\Delta T_{nor}+T_{surf}\right]e^{-\tau}d\tau \\ &= \left(T_{deep}-T_{surf}\right)\cdot\int_0^1\Delta T_{nor}dt+T_{surf}\end{aligned} \tag{6.16}$$

To acquire the soil optical depth where the soil temperature equals T_{eff} (hereafter as τ_{Teff}), we solve

$$\tau_{Teff} = -\ln\left(1 - t\Big|_{\frac{T_{eff}}{T_{deep}-T_{surf}}=1-(1-t)^b\cdot(-\ln(1-t)+1)}\right) \tag{6.17}$$

If T_{eff} , T_{surf} , T_{deep} are given and the parameter b determined by fitting given profile observations of $T(\tau)$ to the parameterization Equation (6.14), we can infer τ_{Teff} via Equation (6.17). Soil moisture/temperature profiles could be taken from field measurement or from model simulation, while the surface temperature could be retrieved from infra-red sensors on satellites or other platforms. T_{deep} can be assumed from climatology. Equation (6.14) postulates a monotonic soil temperature profile with soil optical depth (τ). Once τ_{Teff} is estimated, the soil temperature sensing depth can be retrieved from $\tau_{eff} = \int_0^{x_{sensing}} \frac{2\pi}{\lambda}\frac{\varepsilon''}{\sqrt{\varepsilon'}}dx$.

6.2.5 *In-situ* Data

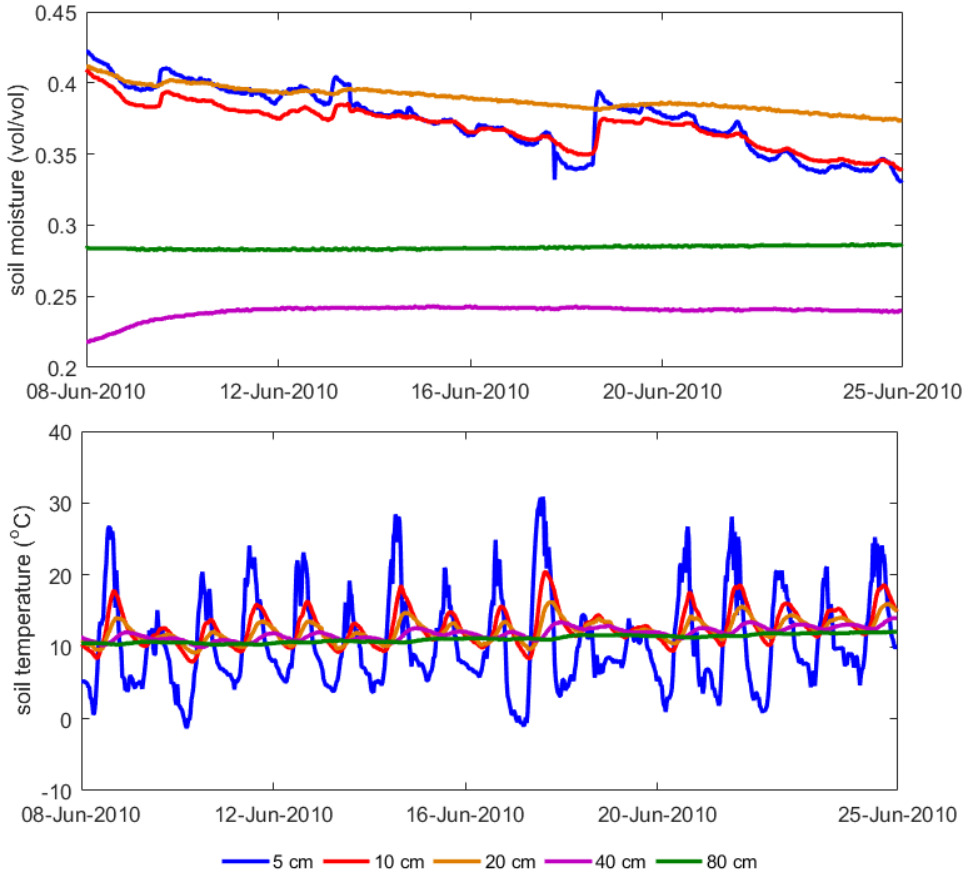

Figure 6.3 The time-series of inputs: soil moisture profile (top) and soil temperature profile (bottom panel).

The Maqu Network locates in Gansu, China, in the northeast margin of the Tibet plateau, and has an average elevation around 3300 m [117, 118]. Vegetation consists of alpine scrublands and meadows, with grass heights less than one meter and roots extending tens of centimeters in depth. The upper 10 cm of the

soil consists of an accumulated humus layer. Shrubs and trees are scarce, while desert dunes sometimes appear along the Yellow River, which runs from the eastern border to its northern border. The Maqu network was installed in 2008. Since then, at least 20 sites of soil moisture/temperature profile observations are being maintained which sufficiently cover one satellite footprint. At each site, soil moisture and temperature probes manufactured by the Decagon Devices Company were deployed. The soil moisture data collected were calibrated according to soil texture and organic content [115-118]. Usually, the depth sampling is 5/10/20/40/80 cm, but for some sites, it is only 5/10 cm.

The center station (Figure 6.3) measures at 5 cm/10 cm/20 cm/ 40 cm/ 80 cm and an infrared sensor provides the surface temperature, so the soil temperature gradient in the top 5 cm can also be inferred. Soil samples are collected near the micro-meteorological observing system, which indicates that the soil at 5 cm depth consists of a sand fraction of 26.95% and clay of 9.86%. The fractions are 29.2% and 10.15% at 0.2 m and 31.6% and 10.43% at 0.4 m[178]. In Figure 6.3, soil moisture and temperature at 80 cm have almost no diurnal variation. Soil temperature at 5 cm/10 cm/ 20 cm/ 40 cm indicate diurnal variation and a phase lag in deeper layers. Soil moisture at 5 cm/10 cm/ 20 cm is more sensitive to precipitation events and evaporation.

6.3 Results and Discussion

6.3.1 Estimation of T_{eff}

We assume that Equation (6.14) sufficiently and accurately describes the soil optical depth-soil temperature relationship. Different soil temperature/moisture profile combinations will result in a different parameter b and accurately enough reproduce the true profiles (Figure 6.4 top panels). If we know one point of such a curve, we know all points. Figure 6.4 (bottom panels) compares $\frac{T_{eff}-T_{surf}}{T_{deep}-T_{surf}}$ based on the observation shown in Figure 6.3. From the theoretical profiles we may conclude that T_{eff} can be estimated with an error of less than 5% (e.g., 2.5 K if $T_{deep}-T_{surf}=50K$). Figure 6.4 (bottom panel) shows that for real profiles $\frac{T_{eff}-T_{surf}}{T_{deep}-T_{surf}}$ only observation at 5 cm or 10 cm is usable for this method. The strong gradients in soil temperature and soil moisture happen already at that depth range. At deeper layers, soil temperature is already too close to T_{deep}, which presents a sufficiently accurate determination of the parameter b.

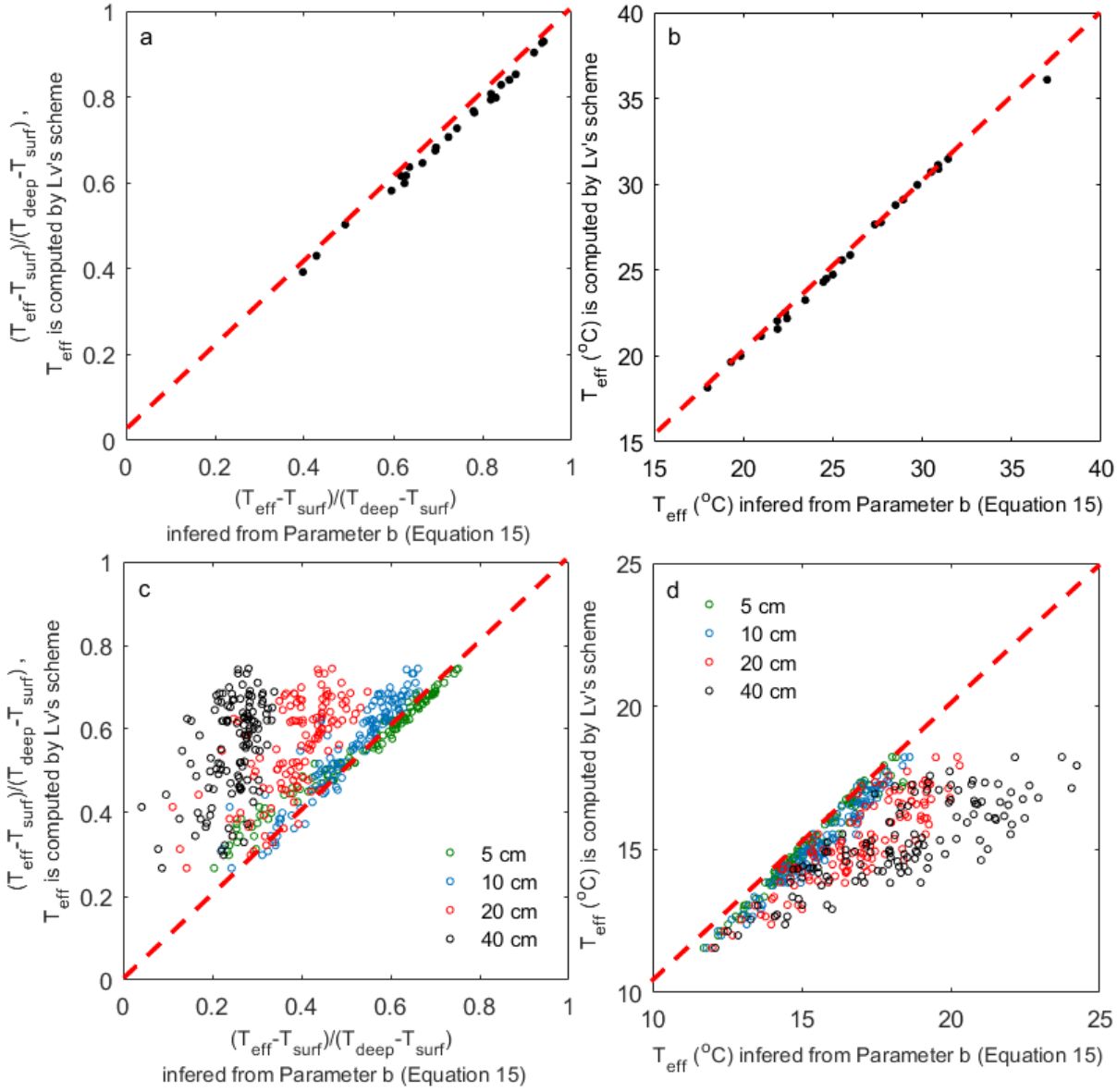

Figure 6.4 The soil effective temperature values inferred from Equation (6.16) vs. the one computed from Lv's scheme for the cases in Figure 6.1 (a,b) and against the field observation at the Maqu network from 2010/6/8 to 2010/6/25 (c,d). Parameter b is calculated from Equation (6.15) while T_{surf} and T_{deep} are taken from the ideal cases or field observation.

6.3.2 Estimation of τ_{Teff}

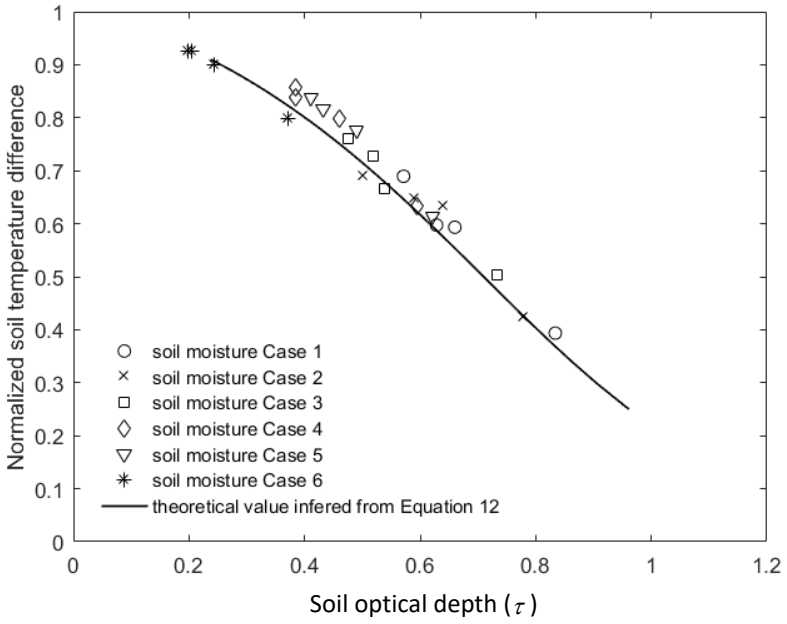

Figure 6.5 τ_{Teff} estimation from Equation (6.17) for soil temperature/moisture profiles in Figure 6.1 except soil temperature Cases 3 and 4 due to monotonic assumption.

For soil temperature Case 3, the gradient is quite small thus $T_{eff} \approx T_i$. The same situation happens for Case 4 which exhibits no soil temperature gradient at all. Figure 6.5 shows for all other profiles the soil optical depth τ_{eff} where the soil temperature equals to T_{eff}. The points follow the theoretical estimation line (Equation (6.17)). It should be noted that τ in this study is computed by Peplinski's dielectric mixing model [186].

While Figure 6.5 shows the ideal cases in Figure 6.1, the result in Figure 6.6 shows the application of Equation (6.17) to the field measurement. Figure 6.6 shows the time series for cases with monotonic soil temperature profiles. This condition is usually satisfied from 10 a.m. to 6 p.m. because after sunrise, the soil temperature gradient is increasing. For T profiles linear in τ, τ_{eff} is the penetration depth. Our results show, however, that the average τ_{eff} is around 0.5, and values may vary between 0.4 to 0.5. The corresponding average geometric depth is 5 cm and varies from 4 cm to 6 cm, i.e., soil temperature sensing depth where its soil temperature equals T_{eff}. The overpassing times of SMOS [60] and SMAP [24] are around at 6 a.m. and 6 p.m., however, the average τ_{eff} (and its geometric depth) does not coincide with τ_{eff} during the overpassing times of the satellites. To investigate τ_{eff} and its corresponding depth during the satellite overpassing time, it requires that the monotone condition is satisfied. It is nevertheless possible to find a depth where the soil temperature equals to T_{eff} by the method introduced in this study, and as such, it may give some clue to find where the soil moisture equals to what is retrieved from the satellites.

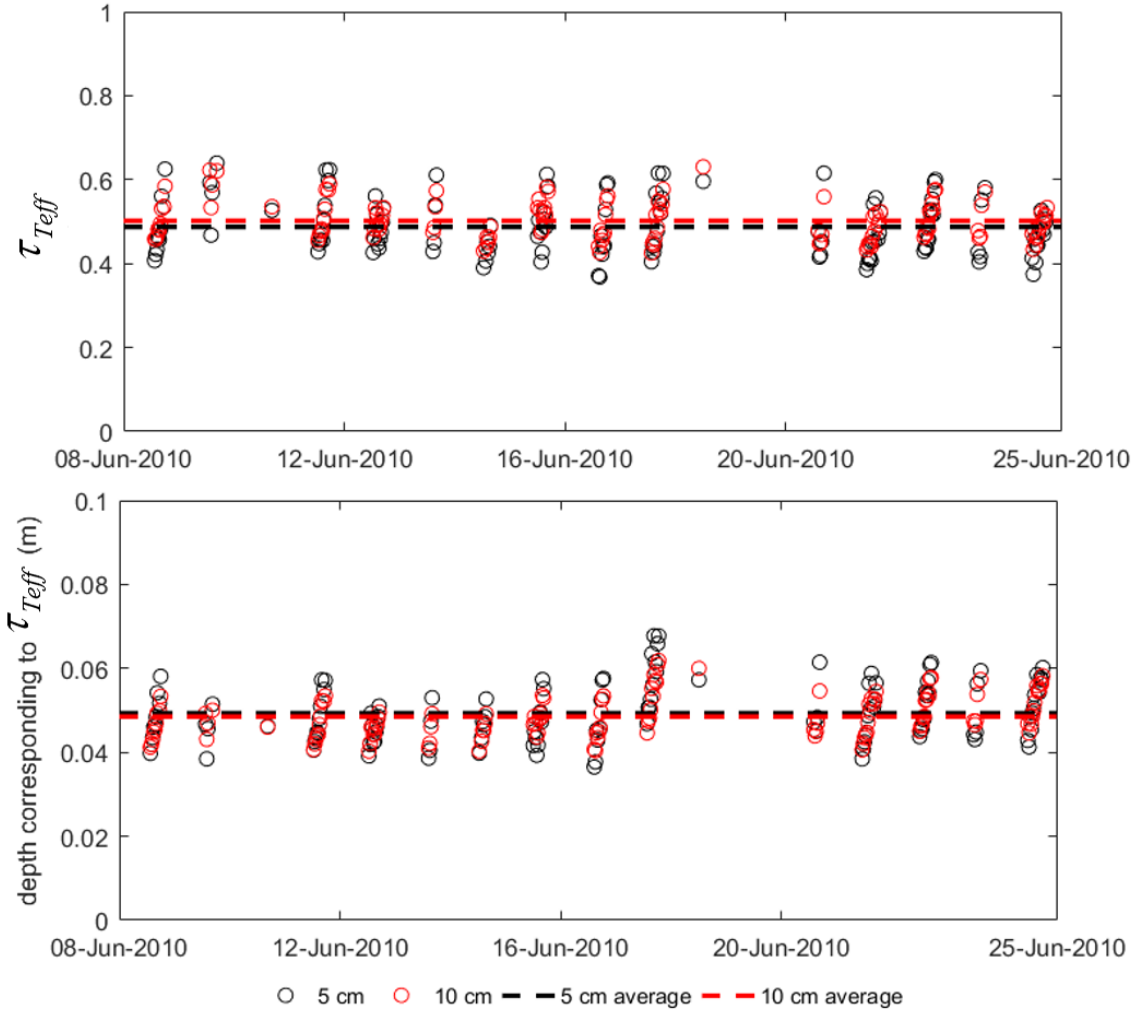

Figure 6.6 The time series of τ_{Teff} (top) and its corresponding soil temperature sensing depth (bottom panel). The points are estimation from Equation (6.17). The depth are computed by $\Delta x = \tau_{Teff} \Big/ \left(\frac{2\pi}{\lambda} \frac{\varepsilon''}{\sqrt{\varepsilon'}} \right)$.

6.3.3 Application to SMAP

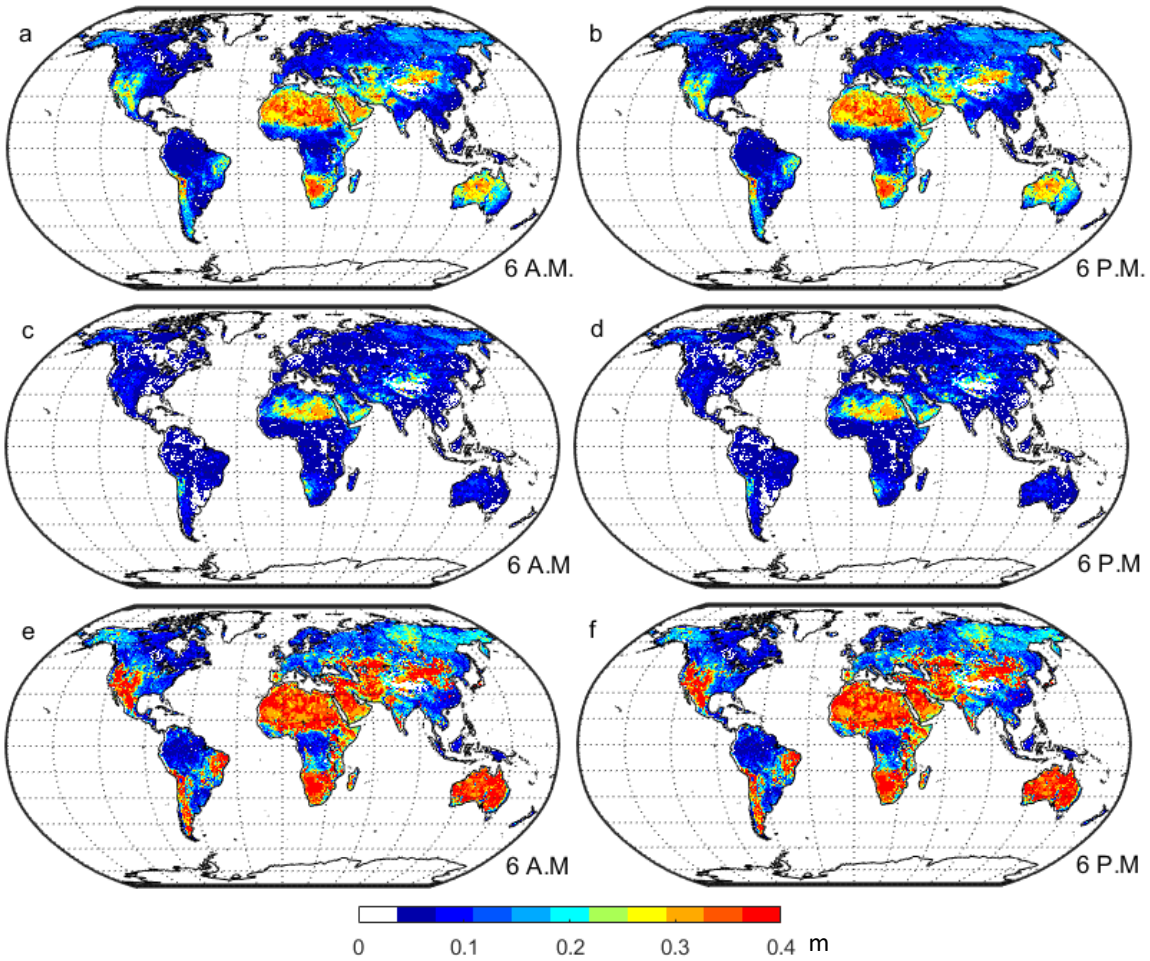

Figure 6.7 The global map of soil temperature sensing geometric depth: a) mean at 6 a.m. local time; b) mean at 6 p.m. local time; c) minimum at 6 a.m. local time minimum; d) minimum at 6 p.m. local time; e) maximum at 6 a.m. local time; f) maximum at 6 p.m. local time.

Surface soil temperature is available from satellites observation, and deep soil temperature can be inferred from the average of soil temperature at any depth, e.g., from models. As T_{eff} is the equivalent soil temperature and the soil moisture retrieved from the zeroth-order incoherent model representing the effective emissivity in Equation (6.1), one may use T_{eff} and the satellite soil moisture product to estimate the soil temperature sensing depth.

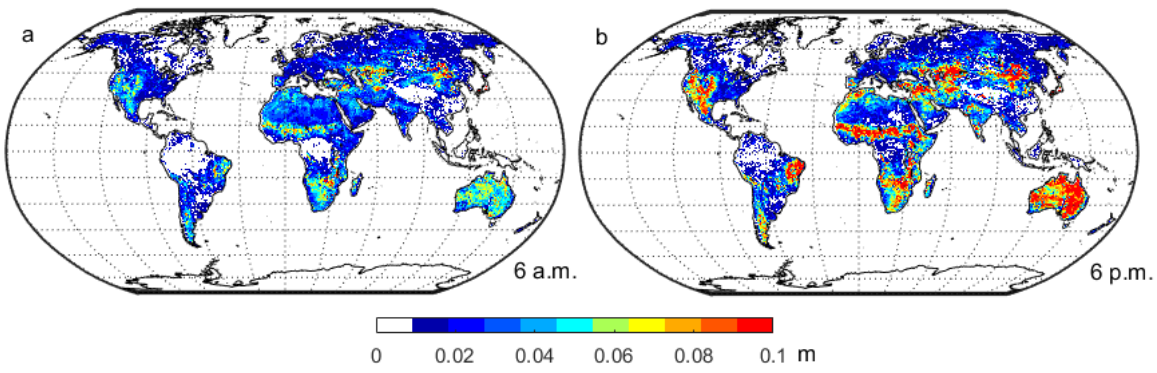

Figure 6.8 The global map of soil temperature sensing depth Standard deviation (RMSD) for: a) 6 a.m.; b) 6 p.m.

Figure 6.7 shows the estimated soil temperature sensing depth map at L-band with the soil effective temperature calculated by MERRA-2 and the SMAP L3 soil moisture for the overpassing times at 6 a.m. and 6 p.m. For most of the area, the soil temperature sensing depth is around 0.05 cm (Figure 6.7 a and b). Extreme cases appear in sub-tropical zones like North Africa, Australia, central Asia, and southern Africa. Among these regions, only North Africa and central Asia persistently result in soil temperature sensing depths of more than 20 cm because of the dry conditions (Figure 6.7 c and d). For the rest area, the soil temperature sensing depth is reduced to about 5 cm once it rains. Figure 6.7 e and f show that the soil temperature sensing depth usually does not reach deeper than 0.1 m except for the sub-tropical zones and other dry areas. The minimum/maximum values are controlled by the variation of soil moisture. The variation of soil temperature sensing depth should be taken into account where the annual soil moisture variation is strong (Figure 6.8). When surface soil is wet, T_{eff} is close to the surface temperature value. On the opposite, T_{eff} approaches the deep soil temperature if the surface soil is dry.

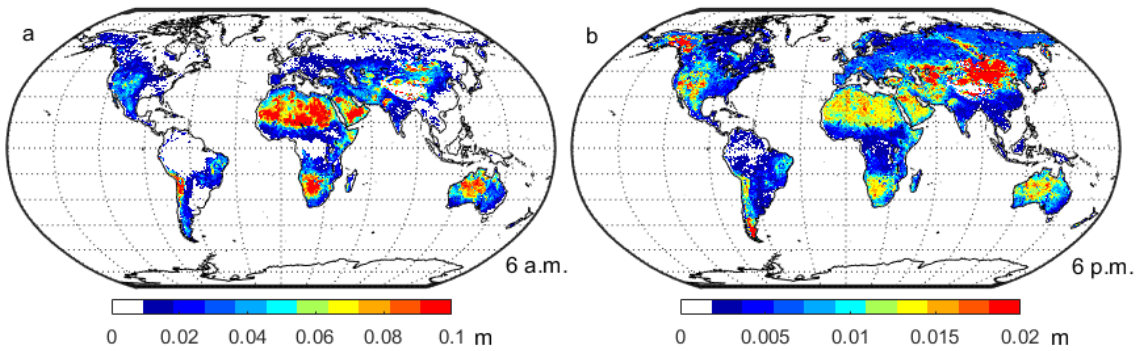

Figure 6.9 The mean difference between penetration depth by Equation (5.8) and soil temperature sensing depth (penetration depth minus soil temperature sensing depth) for: a) 6 a.m.; b) 6 p.m.

In this study, we distinguish soil temperature sensing depth and penetration depth while previous works [62] assume that both are identical. Figure 6.9 gives a global map of the difference between both,

which shows that the penetration depth is always deeper than the soil temperature sensing depth. The difference can reach 10 cm at 6 a.m. but only 2 cm at 6 p.m. because the soil temperature profile is monotonic in the latter case. Main differences appear in the subtropics.

6.4 Conclusions

This research aims to improve our understanding of the assumptions and hypothesis when simplifying the incoherent model to a coherent model. In particular, we developed an objective method to estimate the soil temperature sensing depth, i.e., the depth at which the soil temperature equals the soil effective temperature in the coherent model. In the incoherent model, just one layer is assumed to represent the soil moisture retrieved from L-band satellites (i.e., one brightness temperature value corresponds to one emissivity, therefore, one soil moisture value). Such assumption challenges our understanding about the depth the satellite is observing. The effective soil temperature depends on the profiles of soil temperature and soil moisture thus the information on the layer the satellites are sensing is possibly hidden in the T_{eff} scheme. Here we revisited the concepts of penetration depth and soil temperature sensing depth which are only identical when T varies linearly with soil optical depth. For non-linear but still monotonous cases, the method developed here can be useful.

The new T_{eff} model proposed by Lv et al. (2014), is a flexible approximation to Wilheit's model, which easily accommodates arbitrary layering assumptions, which can reach from two layers as the minimum to as many layers as needed while approaching the accuracy of Wilheit's model. Thus the scheme can be easily applied to field observation and model output. In this study, a semi-empirical model is developed to describe the common features of various soil moisture/temperature profile combinations. With this model, it is possible to identify the relationship between geometric soil depth, penetration depth, and the soil temperature sensing depth and allows to estimate the depth SMOS and SMAP are observing.

As a final note, we would like to highlight that the problem about where the satellites are observing still needs extensive research. To investigate this problem further, the detailed soil moisture & soil temperature profiles are needed as well as corresponding ground-based radiometer observations, to be deployed across different climate zones. Only in this way, we can exclude other influence factors like scale, sub-pixel landscape mixture, RFI, etc. Furthermore, the observation period should cover years and seasons, and must not be limited by the satellites' overpassing times.

Chapter

7 Synthesis

7.1 Summary

This research aims to improve our understanding of the implications resulting from assumptions made when simplifying a coherent model to become an incoherent model for microwave radiative transfer at the soil-atmosphere boundary. Currently, the soil emissivity used in the incoherent approach is attributed to only one layer for L-band satellite retrievals. One brightness temperature value corresponds to one emissivity, and thus to one soil moisture value. However, it is not clear which depth this emissivity refers to. For the soil effective temperature, assumptions are usually made about the retrieval profiles of both soil moisture and soil temperature. We hypothesize that the layer weight in the T_{eff} formulation and the depth attribution also apply to the emissivity.

Lv's soil effective temperature scheme is introduced as a variant of Wilheit's integral T_{eff} model, which allows to easily accommodates different soil profile information. With an increasing number of layers, the model converges to Wilheit's integral T_{eff} model. This feature allows for the easy application of Lv's model with both field observations and model outputs. In its formulation for two layers, Lv's model for T_{eff} explicitly contains depth information, which is neglected in the current existing two-layer models and compensated for by an empirical parameter.

After derivation of Lv's scheme (Chapter 2), its physical interpretations are elaborated on (Chapter 3) and then compared to other T_{eff} schemes (Chapter 4). In Chapter 5 and 6, Lv's scheme is further investigated concerning its applicability to soil moisture retrievals. We proved the following:

1) Lv's scheme is applicable to field observations and model outputs. Its accuracy is comparable to other current two-layer soil effective temperature schemes.
2) With the linear assumption, the microwave penetration depth is equal to the depth where $T_{eff} = T(z)$. In this case, the penetration depth is thus also the depth at which the soil moisture is retrieved via the Fresnel model. For non-linear T-profiles, the penetration depth is not equal to the depth at which $T_{eff} = T(z)$, but we can estimate it from the soil effective temperature.
3) We developed a method to retrieve the depth where $T_{eff} = T(z)$ and thus the depth at which soil moisture is retrieved by the Fresnel model, from observations of the skin temperature only and the

climatological soil temperature at a deep layer. Required is, however, a representative data set of sufficiently sampled profiles of soil moisture and temperature as well as information on the soil moisture retrieval scheme.

We have fully explained the physics behind the soil temperature sensing depth as defined by Ulaby et al. [62]. Retrieving the soil temperature sensing depth would help us further investigate the moisture sensing depth. If the Fresnel model is interpreted as a simplified coherent model, then we can infer that: given a monotonic soil temperature profile, the soil moisture at the depth where the soil temperature equals the soil effective temperature determines the (effective) emissivity used in the Fresnel model and thus is where the soil moisture is retrieved. The temperature sensing depth is related to the moisture sensing depth since the weighting function $de^{-\tau}$ is the same.

As a final note, we would like to highlight that the problem of at which depth satellites are observing is still in need of extensive research. To investigate this problem further, refined soil moisture & soil temperature profiles are needed, as well as corresponding ground radiometers, which need to be deployed across different climate zones. Only in this way, can we exclude other influencing factors such as scale, sub-pixel landscape mixture, and RFI. Observations should cover all time scales when soil temperature profiles vary a lot (i.e., not be limited by the satellites' over-passing time). As more observation datasets are made available, the conclusions reached in this thesis can then be further verified.

7.2 Discussion

Lv's soil effective temperature scheme is an analytical expression that accommodates all dielectric information just like an integral scheme (e.g., Wilheit's scheme). The scheme can be applied with arbitrary numbers of soil layers and converges to the integral scheme. Lv's scheme could also be compressed to just one layer, to explain the physical meaning behind penetration depth. The key feature of Lv's scheme is that it connects the optical thickness (τ) in microwave remote sensing with the physical depth that is usually used in models and *in-situ* measurements. Thus, Lv's scheme bridges the existing two-layer T_{eff} schemes and the integral scheme. In Chapter 4, we demonstrated that the different two-layer schemes could differ in T_{eff} by >5 K, which can lead to a difference in emissivity of 0.015. Such differences lead to errors of 0.04 $cm^3\ cm^{-3}$ in soil moisture. With the formulation of Lv's scheme, we tried to further answer the following questions:

1) How can we evaluate the appropriateness of ground networks for SMOS/SMAP calibration and validation? Are sensors mounted at optimal depth for L-band remote sensing?
2) Where exactly are the radiometers observing soil moisture? In other words, how does satellite soil moisture correspond to field observations?

These issues are vital to the application of SMOS/SMAP soil moisture products. The answers can help to improve not only the calibration/validation of satellite soil moisture but also the data assimilation of soil moisture for climate/weather forecasts.

As discussed in Chapter 5 and 6, the penetration depth is equal to the depth where $T_{eff} = T(z)$ and T increases/decreases monotonically with the optical depth τ . Biases between satellite soil moisture products and ground observation can be reduced by considering the penetration depth. Depending on the frequency used, satellite soil moisture products refer to different sensing depths, which must be considered for the inter-comparison between satellite soil moisture products. Moreover, soil sensing depth depends on soil moisture if the SMOS/SMAP product refers to soil moisture at greater depth over arid regions than over humid regions. Even within one region, the sensing depths may vary considerably, depending on the soil moisture & soil temperature profiles (Njoku 1977; Njoku and Entekhabi 1996). For that reason, different satellite soil moisture products can only be compared, after sensing depths are defined precisely. Data assimilation of T_b deploying land surface models is deemed the most productive method for estimating soil moisture profiles (Entekhabi et al. 1994, Njoku et al. 1996). With a coupled heat and moisture flow model, the remotely sensed information can be extrapolated to arbitrary depths. It is, therefore, critical to understanding the satellite signal.

An 'ELBARA III' L-band radiometer built by the GAMMA company in Switzerland was installed on the Tibetan Plateau to support the project "Modelling Freeze-Thaw Processes with Active and Passive Microwave Observations." The interpretation of its measurements, as well as of the satellite observations, requires a thorough observation of the soil dielectric constant profile.

For validation purpose, the *in-situ* network consists of several sites within one or more satellite pixels. These sites should cover the typical landscapes in these pixels such as grassland and bare soil for the Tibetan Plateau. The optimal retrieval depth of profiles, given limited resources, yet needs to be discussed. Chapter 3 suggests the best depth combination when only two layers can be observed and discusses its implications for affecting emissivity.

Since T_{eff} is a weighted mean of the soil temperature along the profile, $T_{\min} \le T_{eff} \le T_{\max}$. Typical diurnal variation usually puts $T_{\max}$ and $T_{\min}$ usually at the surface or in the deep layer where the soil temperature is almost constant. It is paramount that observations should always restrict T_{eff} . Figure 7.1 is an illustration of this concept, T_{eff} will vary over time and be closer to the surface when the soil is wet and closer to the deep soil temperature when the soil is dry. If the variation of the penetration depth is within the range of two sensor-mounting depths, the weighting function for any two-layer soil effective temperature scheme will produce a relatively accurate estimated penetration depth. T_{eff} depends on the soil moisture gradient. B_{1s} and B_{2s} are the sampling optical depths corresponding to the geometric depths of Δx_{1s} and Δx_{2s} , respectively (see Chapter 3). Figure 7.1 shows the relationship between the representativeness of the sensors and the variation in real sensing depth. Next, we will discuss the error caused by this representativeness.

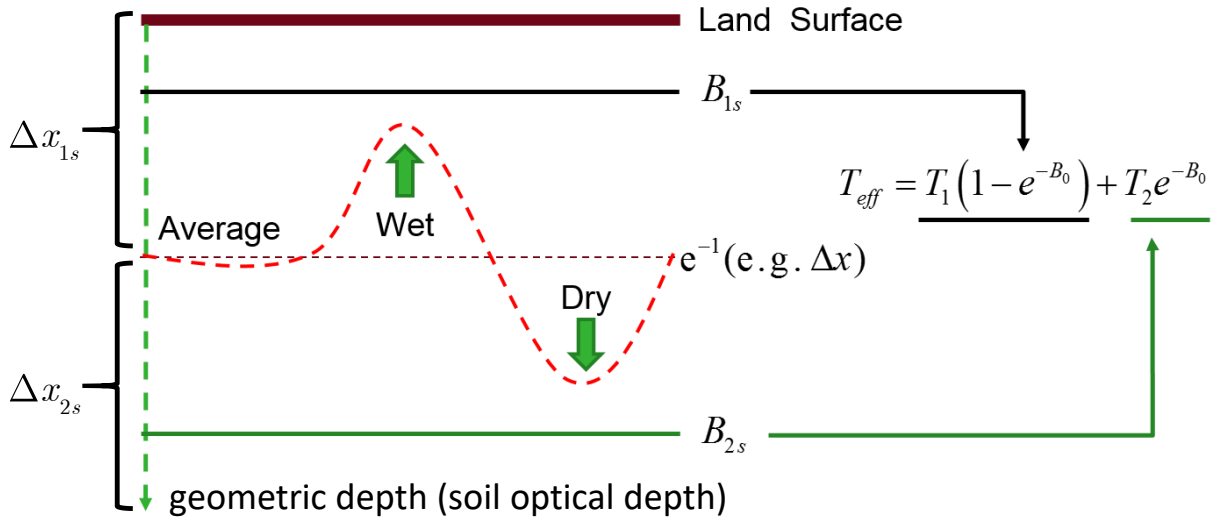

Figure 7.1 The framework of varying sensing depth in terms of Lv's T_{eff} model. B_{1s} and B_{2s} are the soil optical depth where sensors are mounted (see their definition in Chapter 3). The red dashes line is the temporal variation of soil moisture sensing depth while the black dashed line is its temporal average.

Chapter 5 proves that the soil temperature at penetration depth is T_{eff} when the T profile is linear. For non-linear cases, we named τ_{Teff} the soil temperature sensing optical depth. The sensing depth is affected mainly by the soil moisture profile. For a certain period, there must be a mean soil moisture layer as well as a mean soil temperature layer, which can be called effective soil moisture and temperature layers, respectively. Hence, there will be a mean depth time-series of the penetration depth (the dashed line in Figure 7.2). There are three possibilities for a single layer mounting of the sensor: 1) at the average penetration depth; 2) above the average sensing depth, which means that the observed soil temperature will have a larger variation than T_{eff} ; or 3) below the average sensing depth, where the observed soil temperature will show less variation than T_{eff} . To quantify the potential bias in calibration/validation work, we have to estimate the distance between mounting depth and sensing depth, which is difficult in a one-layer setting.

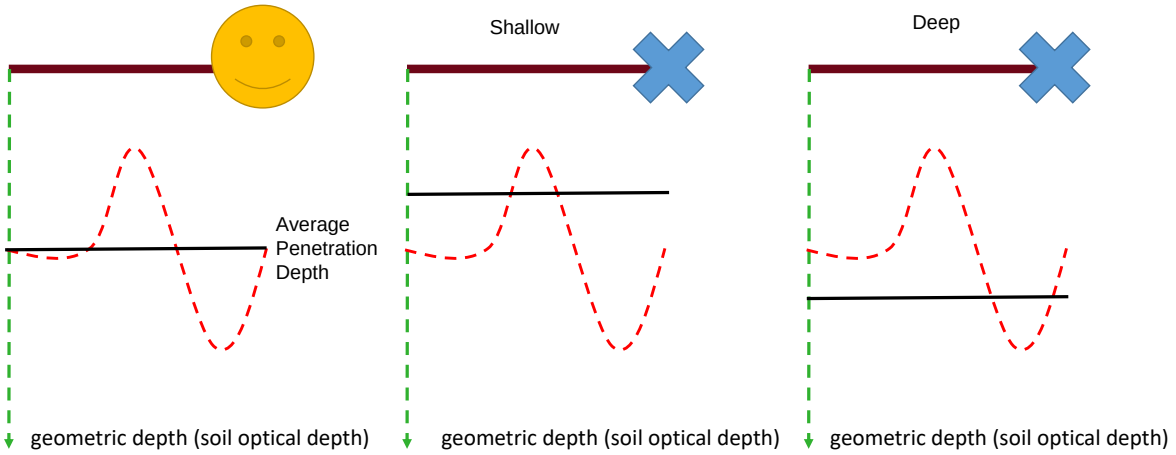

Figure 7.2 An illustration of the best mounting depth if just one layer soil moisture/temperature observation is available.

Figure 7.3 illustrates the appropriate mounting depths for two-layer models. If these two layers cover the variation in T_{eff} , it is possible to acquire an accurate estimation of penetration depth and then pick up the correct soil moisture layer to compare, e.g., with the SMOS/SMAP soil moisture products. The estimation would also be a prospective way to apply the $T_b - T_{eff} - \tau - depth$ relationship in practice by using the sensing depth estimation model established in Chapter 6.

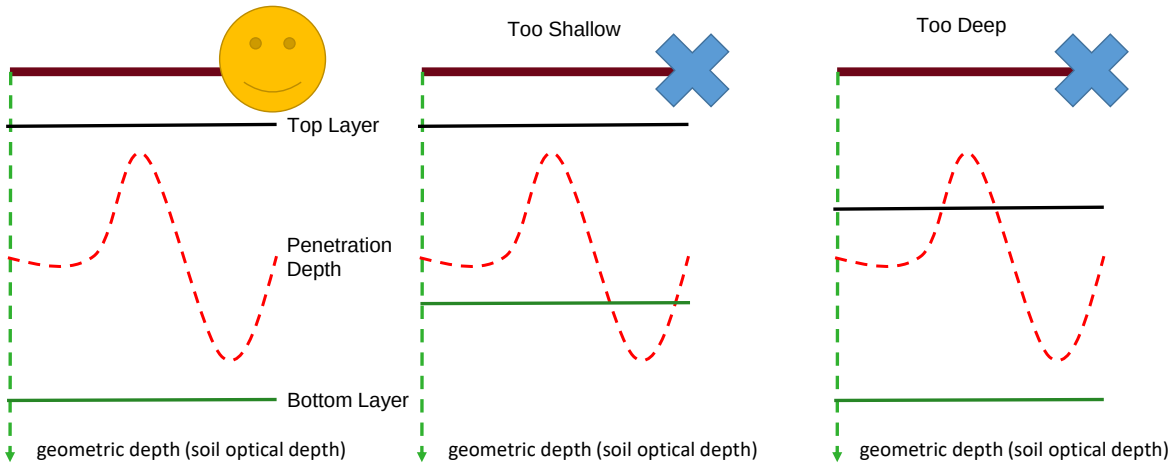

Figure 7.3 Scheme for two soil moisture and temperature observations. With this setup, it is possible to determine whether the penetration depth lies between these two layers or not. If the penetration depth does lie between them, it is possible to use Lv's effective temperature scheme to estimate it.

7.3 Future Perspectives

7.3.1 Forward simulations to determine the soil moisture sensing depth

T_{eff} is a variable that only appears in zeroth-order incoherent emission models. With Chapter 3 to 6, we explored its formulation and the physics related to the optimal mounting depth in the field. We also evaluated its impact on the emissivity error at the L-band. Furthermore, we investigated the link among T_b, T_{eff}, τ and geometric depth, which improved our understanding to the physics of coherent models. However, due to limited observations, this study did not further investigate the connection between soil temperature sensing depth and soil moisture sensing depth. Two further pathways may be pursued:

1) In the forward microwave radiative transfer model, the simulated brightness temperature based on dynamic sensing depth would result in a smaller RMSE (not unRMSE) for radiometer measurements than when based on a fixed soil moisture layer. As shown in Figure 7.1, the real sensing depth varies with different dielectric constant profiles;

2) Current satellite soil moisture retrievals use the Fresnel model (zeroth-order incoherent model), which has only one emissivity to transfer into one soil moisture value. We expect that retrieved soil moisture will correspond better to a varying sensing depth. This will need to be better researched.

We already tested L-MEB (Land Parameter Retrieval Model) and CMEM at the Maqu network and the MELBEX site. The simulations for these two sites are encouraging, but also indicate a clear bias, especially after rainfall when the soil moisture gradient is very sharp (results not shown). To formulate the bias regarding a mounting moisture sensing depth, we need vertically dense soil temperature/moisture profiles and ground-based radiometer observations. Different to the default in the CMEM, where the soil moisture at the first layer stands for the emissivity of the entire column, the soil moisture at the sensing depth would be useful to know to understand microwave remote sensing of soil moisture better. A simulation considering the sensing depth is expected to have less RMSE (not unRMSE) than if only one fixed soil moisture layer is considered.

7.3.2 Application in SMAP Cal/Val

As shown in Chapter 5, penetration depths range from several centimeters to 50 cm for the arid zone. However, according to the current standard of the SMAP Cal/Val project, all ground networks are configured to measure soil moisture at 5 cm. This is questionable because the source of an emission signal varies with the dielectric profile. This variation exists both in the spatial distribution and the temporal dynamics. SMAP Cal/Val ignores this phenomenon and uses statistic performance indicators to prove that the soil moisture retrieval is successful. These statistics are more or less reasonable because, without the Fresnel model, brightness temperature can still be assimilated into weather/climate forecasting. However, the improvement in comparing values between ground measurement and satellite-derived soil moisture cannot be achieved without a clear definition of soil moisture sensing depth. Escorihuela et al. (2010) found that the average soil moisture sensing depth is around 0-2 cm. Different to conclusions by Escorihuela et al.

(2010)[65], our study reveals that T_{eff} represents the "average value" of soil temperature of a soil column and may lead to effective soil moisture representing the "average emissivity value."

In short, the SMOS/SMAP soil moisture (emissivity) retrieval from satellites should also be an "average value" of the whole soil column. Soil temperature sensing depth and soil moisture sensing depth are both addressed in Ulaby's book [62], though no clear math expression for the soil moisture sensing depth is presented. With clearly defined soil sensing depth, the bias between satellite soil moisture products and ground measurements will be understood. The Maqu network was built up in 2008. The network includes about 20 sites, and the average figures for these sites are supposed to be the true ground values to be compared with satellite footprint observations. Most of these sites measurements are configured at 5 layers (5cm, 10cm, 20cm, 40cm and 80cm), which is at much finer than seen in most of the other similar networks around the globe (i.e., only two layers, at 5cm and 10cm). We need very detailed land surface models to generate a continuous soil profile so that we can capture the dynamics of moisture sensing depth. This modeling is beyond the scope of this thesis and may be attempted in the future.

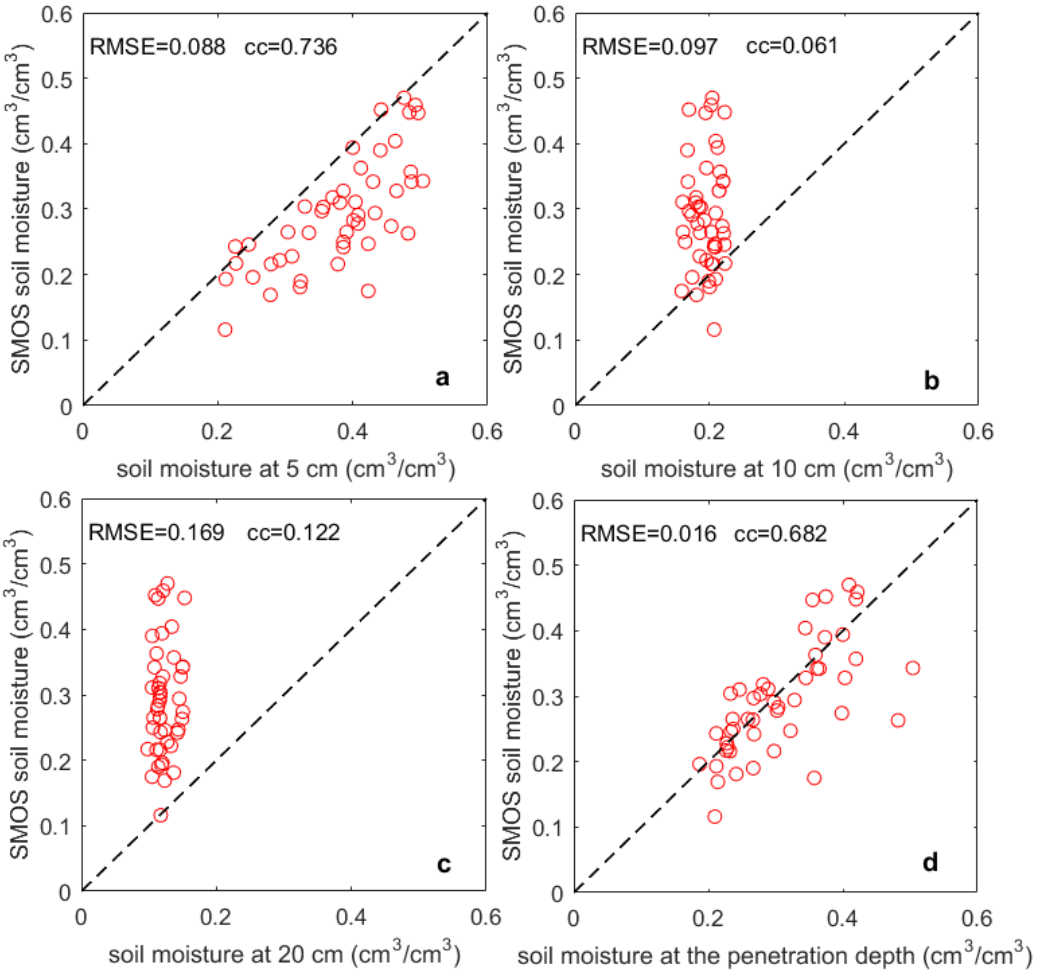

Figure 7.4 Comparison of the SMOS soil moisture product against *in-situ* soil moisture observation at 5 cm (a), 10 cm (b), 20 cm (c), and at the penetration depth (d). The soil moisture observation at the penetration depth is interpolated by using in-situ measured soil moisture profiles. The period is from June 12th to 28th, 2010.

Figure 7.4 compares the SMOS soil moisture product with soil moisture observations at penetration depth at Maqu center station, as well as soil moisture observed at different depths. Observations at 5 cm depth correlate better with the SMOS soil moisture product than other layers do (Figure 7.4a), but shows a clear bias. Deeper layers show no correlation with SMOS observations (Figure 7b&c). When the penetration depth is used (Figure 7.4d) a good match with SMOS is achieved although with a slightly lower correlation than for the 5 cm observation. As is well known, soil temperature along the depth (or τ) could be monotonous at particular hours before sunset. However, we argued that this bias is simply due to the sensing depth. In this study, a penetration depth that is varying along with the dielectric profile could reduce the bias introduced by inappropriate ground Cal/Val depths.

7.3.3 Application in model assimilation

The limit in deterministic weather forecasting is about 14 days [187, 188]. Data assimilation, especially from satellites forms the key to improving the initial condition. However, soil moisture products from SMOS and SMAP are not optimal for data assimilation, because soil moisture is not directly observed. With the help of an approximated observation operator in the data assimilation system, the physics and dynamics contained in soil moisture can be linked with the brightness temperature and updated accordingly. As such, the problem of improperly assumed moisture sensing depth does in principle not occur. However, when using only limited retrieval due to computational power limitation, the moisture sensing depth may come into play again. Instead of updating the entire soil temperature/moisture profile, it would be more efficient to include the layers which correspond with T_B. Considering sensing depth would mean that we could limit the data volume in the data assimilation with improved efficiency. This strategy will be used in my future work at the University of Bonn.

Samenvatting

Dit onderzoek heeft als doel het beter begrijpen van de implicaties ter gevolge van de aannames die gedaan worden als een coherent radiative transfer-model wordt versimpeld naar een incoherent radiative transfer-model in de context van microgolfstraling bij een materie overgang van lucht naar grond. Uitgaande van de incoherente aanpak wordt op dit moment bij satellietmetingen in L-band de microgolfemissie afkomstig van de grond toegekend aan één (homogene) grondlaag. Eén helderheidstemperatuurwaarde correspondeert met één emissiewaarde, en dus tevens één waarde voor het grondvocht gehalte. Het is echter niet duidelijk naar welke diepte deze enkele emissiewaarde refereert. Voor het berekenen van de effectieve grondtemperatuur T_{eff} wordt meestal gewerkt met bepaalde aannames voor de diepteprofielen van de grondtemperatuur en het grondvocht-gehalte. Hier stellen wij de hypothese dat het gebruik van weegtermen voor de verschillende gronddieptes én het gebruik van een zogenoemde toekenningsdiepte, zoals bij de formulering van T_{eff}, tevens is toegestaan voor de emissie.

Lv's methode voor de berekening van T_{eff} wordt geïntroduceerd als zijnde een variant op de T_{eff} integraalmethode van Wilheit. Deze integraalmethode maakt het mogelijk om op een gemakkelijke manier met verschillende bodem profielen te werken. Als het aantal grondlagen toeneemt convergeert Lv's model naar Wilheit's T_{eff} integraalmodel. Deze convergerende eigenschap zorgt ervoor dat Lv's model makkelijk kan worden gebruikt met zowel veldobservaties als modelresultaten. Toegepast op het geval van twee grondlagen bevat Lv's model expliciete informatie over de diepte. Bij huidige 2-laagsmodellen is deze diepte-informatie niet voorhanden. In plaats daarvan wordt er gebruikt gemaakt van empirische parameters.

Na de afleiding van Lv's model (hoofdstuk 2) zullen zijn fysische interpretaties worden toegelicht (hoofdstuk 3) waarna vervolgens een vergelijking met andere T_{eff} modellen zal worden gemaakt (hoofdstuk 4). In hoofdstukken 5 en 6 zal Lv's model verder worden onderzocht met betrekking tot de toepasbaarheid bij het achterhalen van het grondvocht gehalte. Het volgende is bewezen:

1. Lv's model kan worden gebruikt met zowel veldobservaties als modelresultaten. De nauwkeurigheid van Lv's model is vergelijkbaar met dat van andere 2-laags T_{eff} modellen.
2. Uitgaande van de lineaire aanname is de penetratiediepte van microgolven gelijk aan die diepte waarvoor geldt $T_{eff} = T(z)$. In dat geval is de penetratie diepte dus gelijk aan dezelfde diepte waarbij, als gebruik wordt gemaakt van het Fresnel model, het grondvocht gehalte wordt afgeleid. Bij niet-lineaire grondtemperatuurprofielen is de penetratie diepte niet gelijk aan de diepte waarvoor geld $T_{eff} = T(z)$, maar kunnen we de penetratie diepte toch schatten met behulp van de effectieve grondtemperatuur.

3. We hebben een methode ontwikkeld om de diepte te achterhalen waarvoor geldt: $T_{eff} = T(z)$. Zoals hierboven vermeldt is dit tevens de diepte waarbij, gebruik makend van het Fresnel model, het grondvocht wordt bepaald. Deze methode gebruikt enkel de door observaties verkregen oppervlaktetemperatuur en de klimatologische bodemtemperatuur op grote diepte. Het is echter wel noodzakelijk dat er een representatieve datareeks voorhanden is van grondvocht- en temperatuurprofielen bestaande uit voldoende meetpunten. Tevens moet er informatie voorhanden zijn over hoe het grondvochtgehalte verkregen wordt.

We hebben de fysica achter de meetgevoeligheidsdiepte van de grondtemperatuur, zoals gedefinieerd in Ulaby [60], volledig toegelicht. Het achterhalen van de meetgevoeligheidsdiepte van de grondtemperatuur zal verder onderzoek naar een soortgelijke meetgevoeligheidsdiepte van grondvocht mogelijk maken. Als het Fresnel model als versimpeld coherent model wordt opgevat en als het grond temperatuur –profiel monotoom is, dan kunnen we als gevolg daarvan in het Fresnel model het grondvochtgehalte op de diepte z waarvoor geldt $T_{eff} = T(z)$ de (effectieve) als bepalend beschouwen voor de emissie. Andersom redenerend is dus het verkregen grondvochtgehalte een eigenschap behorend bij de diepte z. Immers, de meetgevoeligheidsdiepte van de grondtemperatuur is gerelateerd aan de meetgevoeligheidsdiepte van het grondvocht omdat de weegfunctie de- hetzelfde is.

Als laatste willen we nog opmerken dat het vraagstuk van op welke diepte satellieten eigenlijk meten nog veel aandacht nodig heeft. Om dit verder te onderzoeken is het nodig om grondvocht- en grond temperatuurprofielen met hogere diepte resolutie te meten. Ook zijn bijbehorende metingen met radiometers, geïnstalleerd nabij het grondoppervlak, nodig. Beide metingen zouden in de verschillende klimaatzones moeten worden uitgevoerd. Alleen op deze manier kunnen ongewenste invloeden zoals; verschillende types land oppervlak per satelliet pixel en RFI (interferentie van ongewenste radiogolf bronnen) uitgesloten worden. Deze observaties zouden over alle tijdschalen moeten worden uitgevoerd, mochten de grond temperatuurprofielen erg dynamisch zijn. Met andere woorden: de overvlieg tijd van satellieten zou voor dit onderzoek niet de limiterende factor mogen zijn. De conclusies van dit proefschrift zouden verder kunnen worden getoetst als er meer datasets beschikbaar zullen zijn.

References

1. Koster, R.D., et al., *Observational evidence that soil moisture variations affect precipitation.* Geophysical Research Letters, 2003. **30**(5).
2. Koster, R.D., et al., *Contribution of land surface initialization to subseasonal forecast skill: First results from a multi-model experiment.* Geophysical Research Letters, 2010. **37**.
3. Dirmeyer, P.A., C.A. Schlosser, and K.L. Brubaker, *Precipitation, Recycling, and Land Memory: An Integrated Analysis.* Journal of Hydrometeorology, 2009. **10**(1): p. 278-288.
4. Koster, R.D., et al., *Realistic initialization of land surface states: Impacts on subseasonal forecast skill.* Journal of Hydrometeorology, 2004. **5**(6): p. 1049-1063.
5. Seneviratne, S.I., et al., *Investigating soil moisture-climate interactions in a changing climate: A review.* Earth-Science Reviews, 2010. **99**(3-4): p. 125-161.
6. Douville, H., *Relative contribution of soil moisture and snow mass to seasonal climate predictability: a pilot study.* Climate Dynamics, 2010. **34**(6): p. 797-818.
7. Zaitchik, B.F., et al., *Representation of Soil Moisture Feedbacks during Drought in NASA Unified WRF (NU-WRF).* Journal of Hydrometeorology, 2013. **14**(1): p. 360-367.
8. Wolters, D., et al., *Effects of soil moisture gradients on the path and the intensity of a West African squall line.* Quarterly Journal of the Royal Meteorological Society, 2010. **136**(653): p. 2162-2175.
9. Svensson, G., et al., *Evaluation of the Diurnal Cycle in the Atmospheric Boundary Layer Over Land as Represented by a Variety of Single-Column Models: The Second GABLS Experiment.* Boundary-Layer Meteorology, 2011. **140**(2): p. 177-206.
10. Pal, J.S. and E.A.B. Eltahir, *A feedback mechanism between soil-moisture distribution and storm tracks.* Quarterly Journal of the Royal Meteorological Society, 2003. **129**(592): p. 2279-2297.
11. Overpeck, J.T., *Climate science: The challenge of hot drought.* Nature, 2013. **503**(7476): p. 350-1.
12. Orth, R. and S.I. Seneviratne, *Analysis of soil moisture memory from observations in Europe.* Journal of Geophysical Research-Atmospheres, 2012. **117**.
13. Miralles, D.G., et al., *Soil moisture-temperature coupling: A multiscale observational analysis.* Geophysical Research Letters, 2012. **39**.
14. Kim, J.-E. and S.-Y. Hong, *Impact of soil moisture anomalies on summer rainfall over East Asia: A regional climate model study.* Journal of Climate, 2007. **20**(23): p. 5732-5743.
15. Frye, J.D. and T.L. Mote, *The Synergistic Relationship between Soil Moisture and the Low-Level Jet and Its Role on the Prestorm Environment in the Southern Great Plains.* Journal of Applied Meteorology and Climatology, 2010. **49**(4): p. 775-791.
16. Frye, J.D. and T.L. Mote, *Convection Initiation along Soil Moisture Boundaries in the Southern Great Plains.* Monthly Weather Review, 2010. **138**(4): p. 1140-1151.
17. Bothe, O., K. Fraedrich, and X.H. Zhu, *The large-scale circulations and summer drought and wetness on the Tibetan plateau.* International Journal of Climatology, 2010. **30**(6): p. 844-855.
18. Betts, A.K., et al., *The land surface-atmosphere interaction: A review based on observational and global modeling perspectives.* Journal of Geophysical Research-Atmospheres, 1996. **101**(D3): p. 7209-7225.
19. Beljaars, A.C.M., et al., *The anomalous rainfall over the United States during July 1993: Sensitivity to land surface parameterization and soil moisture.* Monthly Weather Review, 1996. **124**(3): p. 362-383.
20. Robock, A., et al., *Use of midlatitude soil moisture and meteorological observations to validate soil moisture simulations with biosphere and bucket models.* Journal of Climate, 1995. **8**(1): p. 15-35.
21. Wang, A.H., D.P. Lettenmaier, and J. Sheffield, *Soil Moisture Drought in China, 1950-2006.* Journal of Climate, 2011. **24**(13): p. 3257-3271.

22. Yu, G.R., et al., *Overview of ChinaFLUX and evaluation of its eddy covariance measurement.* Agricultural and Forest Meteorology, 2006. **137**(3-4): p. 125-137.
23. Evans, J., et al., *Soil water content in southern England derived from a cosmic-ray soil moisture observing system–COSMOS-UK.* Hydrological Processes, 2016. **30**(26): p. 4987-4999.
24. Colliander, A., et al., *Validation of SMAP surface soil moisture products with core validation sites.* Remote Sensing of Environment, 2017. **191**: p. 215-231.
25. Dorigo, W., et al., *A new international network for in situ soil moisture data.* Eos, Transactions American Geophysical Union, 2011. **92**(17): p. 141-142.
26. Chen, F. and J. Dudhia, *Coupling an advanced land surface-hydrology model with the Penn State-NCAR MM5 modeling system. Part I: Model implementation and sensitivity.* Monthly Weather Review, 2001. **129**(4): p. 569-585.
27. Webster, P.J. and S. Yang, *Monsoon and Enso - Selectively Interactive Systems.* Quarterly Journal of the Royal Meteorological Society, 1992. **118**(507): p. 877-926.
28. Szczypta, C., et al., *Suitability of modelled and remotely sensed essential climate variables for monitoring Euro-Mediterranean droughts.* Geoscientific Model Development, 2014. **7**(3): p. 931-946.
29. Balsamo, G., et al., *A Revised Hydrology for the ECMWF Model: Verification from Field Site to Terrestrial Water Storage and Impact in the Integrated Forecast System.* Journal of Hydrometeorology, 2009. **10**(3): p. 623-643.
30. Bosilovich, M.G., F.R. Robertson, and J.Y. Chen, *Global Energy and Water Budgets in MERRA.* Journal of Climate, 2011. **24**(22): p. 5721-5739.
31. Balsamo, G., et al., *ERA-Interim/Land: a global land water resources dataset.* Hydrol. Earth Syst. Sci. Discuss., 2013. **10**(12): p. 14705-14745.
32. Koster, R.D., et al., *On the Nature of Soil Moisture in Land Surface Models.* Journal of Climate, 2009. **22**(16): p. 4322-4335.
33. Rudiger, C., et al., *An Intercomparison of ERS-Scat and AMSR-E Soil Moisture Observations with Model Simulations over France.* Journal of Hydrometeorology, 2009. **10**(2): p. 431-447.
34. Moncet, J.L., et al., *Land surface microwave emissivities derived from AMSR-E and MODIS measurements with advanced quality control.* Journal of Geophysical Research-Atmospheres, 2011. **116**.
35. Al-Shrafany, D., D. Han, and M.A. Rico-Ramirez, *Near-surface soil moisture estimation using AMSR-E brightness temperature.* Remote Sensing and Hydrology, 2012. **352**: p. 11-15.
36. Cavalieri, D.J. and J.C. Comiso, *Algorithm theoretical basis document (ATBD) for the AMSR-E sea ice algorithm.* NASA Goddard Space Flight Center, 2000.
37. Jackson, T.J., et al., *Validation of Advanced Microwave Scanning Radiometer Soil Moisture Products.* IEEE Transactions on Geoscience and Remote Sensing, 2010. **48**(12): p. 4256-4272.
38. Njoku, E.G., et al., *Soil moisture retrieval from AMSR-E.* Ieee Transactions on Geoscience and Remote Sensing, 2003. **41**(2): p. 215-229.
39. Kerr, Y.H., et al., *The SMOS Mission: New Tool for Monitoring Key Elements of the Global Water Cycle.* Proceedings of the Ieee, 2010. **98**(5): p. 666-687.
40. Kerr, Y.H., et al., *The SMOS Soil Moisture Retrieval Algorithm.* Ieee Transactions on Geoscience and Remote Sensing, 2012. **50**(5): p. 1384-1403.
41. Le Vine, D.A., et al., *Aquarius: An instrument to monitor sea surface salinity from space.* Ieee Transactions on Geoscience and Remote Sensing, 2007. **45**(7): p. 2040-2050.
42. Wang, Q., R. van der Velde, and Z. Su, *Use of a discrete electromagnetic model for simulating Aquarius L-band active/passive observations and soil moisture retrieval.* Remote Sensing of Environment, 2017. **205**: p. 434-452.

43. Entekhabi, D., et al., *The Soil Moisture Active Passive (SMAP) Mission.* Proceedings of the Ieee, 2010. **98**(5): p. 704-716.
44. O'Neill, P., et al., *Soil Moisture Active Passive (SMAP), Algorithm Theoretical Basis DocumentLevel 2 & 3 Soil Moisture (Passive) Data Products, Revison B.* 2015.
45. Pan, M., et al., *An Initial Assessment of SMAP Soil Moisture Retrievals Using High Resolution Model Simulations and In-situ Observations.* Geophysical Research Letters, 2016: p. 9662-9668.
46. Dorigo, W., et al., *ESA CCI Soil Moisture for improved Earth system understanding: State-of-the art and future directions.* Remote Sensing of Environment, 2017. **203**: p. 185-215.
47. Gruber, A., et al., *Triple Collocation-Based Merging of Satellite Soil Moisture Retrievals.* IEEE Transactions on Geoscience and Remote Sensing, 2017. **55**(12): p. 6780-6792.
48. De Lannoy, G.J.M. and R.H. Reichle, *Global Assimilation of Multiangle and Multipolarization SMOS Brightness Temperature Observations into the GEOS-5 Catchment Land Surface Model for Soil Moisture Estimation.* Journal of Hydrometeorology, 2016. **17**(2): p. 669-691.
49. Drusch, M., et al., *Towards a Kalman Filter based soil moisture analysis system for the operational ECMWF Integrated Forecast System.* Geophysical Research Letters, 2009. **36**(10): doi:10.1029/2009GL037716
50. de Rosnay, P., et al., *A simplified Extended Kalman Filter for the global operational soil moisture analysis at ECMWF.* Quarterly Journal of the Royal Meteorological Society, 2013. **139**(674): p. 1199-1213.
51. Munoz-Sabater, J., et al., *Sensitivity of Soil Moisture Analyses to Contrasting Background and Observation Error Scenarios.* Water, 2018. **10**(7). doi:10.3390/w10070890
52. van der Schalie, R., et al., *SMOS soil moisture retrievals using the land parameter retrieval model: Evaluation over the Murrumbidgee Catchment, southeast Australia.* Remote Sensing of Environment, 2015. **163**(Supplement C): p. 70-79.
53. Chen, Y., et al., *Evaluation of SMAP, SMOS, and AMSR2 soil moisture retrievals against observations from two networks on the Tibetan Plateau.* Journal of Geophysical Research: Atmospheres, 2017. **122**(11): p. 2016JD026388.
54. Shi, C.X., et al., *China land soil moisture EnKF data assimilation based on satellite remote sensing data.* Science China-Earth Sciences, 2011. **54**(9): p. 1430-1440.
55. Yang, K., et al., *Land surface model calibration through microwave data assimilation for improving soil moisture simulations.* Journal of Hydrology, 2016. **533**: p. 266-276.
56. Yang, K., et al., *Auto-calibration system developed to assimilate AMSR-E data into a land surface model for estimating soil moisture and the surface energy budget.* Journal of the Meteorological Society of Japan. Ser. II, 2007. **85**: p. 229-242.
57. De Lannoy, G.J.M., et al., *State and bias estimation for soil moisture profiles by an ensemble Kalman filter: Effect of assimilation depth and frequency.* Water Resources Research, 2007. **43**(6).
58. Lewis, P., et al., *An Earth Observation Land Data Assimilation System (EO-LDAS).* Remote Sensing of Environment, 2012. **120**: p. 219-235.
59. Draper, C.S., et al., *Assimilation of passive and active microwave soil moisture retrievals.* Geophysical Research Letters, 2012. **39**. doi.org/10.1029/2011GL050655
60. Wigneron, J.P., et al., *Modelling the passive microwave signature from land surfaces: A review of recent results and application to the L-band SMOS & SMAP soil moisture retrieval algorithms.* Remote Sensing of Environment, 2017. **192**: p. 238-262.
61. Al-Yaari, A., et al., *Evaluating soil moisture retrievals from ESA's SMOS and NASA's SMAP brightness temperature datasets.* Remote Sensing of Environment, 2017. **193**: p. 257-273.
62. Ulaby, F.T., R.K. Moore, and A.K. Fung, *Microwave Remote Sensing Active and Passive-Volume III: From Theory to Applications*. 1986: Artech House, Inc.

63. Zhou, F.C., et al., *An Effective Emission Depth Model for Passive Microwave Remote Sensing.* Ieee Journal of Selected Topics in Applied Earth Observations and Remote Sensing, 2016. **9**(4): p. 1752-1760.
64. Shellito, P.J., et al., *SMAP soil moisture drying more rapid than observed in situ following rainfall events.* Geophysical Research Letters, 2016. **43**(15): p. 8068-8075.
65. Escorihuela, M.J., et al., *Effective soil moisture sampling depth of L-band radiometry: A case study.* Remote Sensing of Environment, 2010. **114**(5): p. 995-1001.
66. Liu, P.W., et al., *Impact of Moisture Distribution Within the Sensing Depth on L- and C-Band Emission in Sandy Soils.* Ieee Journal of Selected Topics in Applied Earth Observations and Remote Sensing, 2013. **6**(2): p. 887-899.
67. Entekhabi, D., et al., *Performance Metrics for Soil Moisture Retrievals and Application Requirements.* Journal of Hydrometeorology, 2010. **11**(3): p. 832-840.
68. van der Schalie, R., et al., *Global SMOS Soil Moisture Retrievals from The Land Parameter Retrieval Model.* International Journal of Applied Earth Observation and Geoinformation, 2016. **45**: p. 125-134.
69. Zeng, J., et al., *A Preliminary Evaluation of the SMAP Radiometer Soil Moisture Product Over United States and Europe Using Ground-Based Measurements.* IEEE Transactions on Geoscience and Remote Sensing, 2016. **54**(8): p. 4929-4940.
70. Rosnay, P.d., M. Drusch, and J. Muñoz-Sabater, *Milestone 1 Tech Note - Part 1: SMOS Global Surface Emission Model.* 2009.
71. de Rosnay, P., et al., *AMMA Land Surface Model Intercomparison Experiment coupled to the Community Microwave Emission Model: ALMIP-MEM.* Journal of Geophysical Research-Atmospheres, 2009. **114**.
72. Drusch, M., et al., *Comparing ERA-40-Based L-Band Brightness Temperatures with Skylab Observations: A Calibration/Validation Study Using the Community Microwave Emission Model.* Journal of Hydrometeorology, 2009. **10**(1): p. 213-226.
73. Wilheit, T.T., *Radiative-Transfer in a Plane Stratified Dielectric.* Ieee Transactions on Geoscience and Remote Sensing, 1978. **16**(2): p. 138-143.
74. Jackson, T.J. and T.J. Schmugge, *Vegetation Effects on the Microwave Emission of Soils.* Remote Sensing of Environment, 1991. **36**(3): p. 203-212.
75. Pellarin, T., et al., *Hydrologic visibility of weather radar systems operating in mountainous regions: Case study for the Ardeche catchment (France).* Journal of Hydrometeorology, 2002. **3**(5): p. 539-555.
76. Wigneron, J.P., et al., *L-band Microwave Emission of the Biosphere (L-MEB) Model: Description and calibration against experimental data sets over crop fields.* Remote Sensing of Environment, 2007. **107**(4): p. 639-655.
77. Kirdyashev, K., A. Chukhlantsev, and A. Shutko, *The Microwave emission of the Earth in the presence of a vegetation canopy.* Radiotechnika i Electronika, 1979(2): p. 256.
78. Wegmüller, U. and C.L. Werner, *SAR interferometric signatures of forest.* IEEE Transactions on Geoscience and Remote Sensing, 1995. **33**(5): p. 1153-1161.
79. Wang, J.R. and B.J. Choudhury, *Remote-Sensing of Soil-Moisture Content over Bare Field at 1.4 Ghz Frequency.* Journal of Geophysical Research-Oceans and Atmospheres, 1981. **86**(Nc6): p. 5277-5282.
80. Wigneron, J.P., L. Laguerre, and Y.H. Kerr, *A simple parameterization of the L-band microwave emission from rough agricultural soils.* Ieee Transactions on Geoscience and Remote Sensing, 2001. **39**(8): p. 1697-1707.

81. Kerr, Y., P. Waldteufel, and P. Richaume, *Algorithm Theoretical Basis Document (ATBD) for the SMOS Level 2 Soil Moisture Processor Development Continuation Project.* SMOS Internal Report, 2014. **2**.
82. Wegmuller, U. and C. Mätzler, *Rough bare soil reflectivity model.* IEEE Transactions on Geoscience and Remote Sensing, 1999. **37**(3): p. 1391-1395.
83. Mironov, V.L., et al., *Generalized refractive mixing dielectric model for moist soils.* Ieee Transactions on Geoscience and Remote Sensing, 2004. **42**(4): p. 773-785.
84. Dobson, M.C., et al., *Microwave Dielectric Behavior of Wet Soil .2. Dielectric Mixing Models.* Ieee Transactions on Geoscience and Remote Sensing, 1985. **23**(1): p. 35-46.
85. Wang, J.R. and T.J. Schmugge, *An Empirical-Model for the Complex Dielectric Permittivity of Soils as a Function of Water-Content.* Ieee Transactions on Geoscience and Remote Sensing, 1980. **18**(4): p. 288-295.
86. Choudhury, B.J., T.J. Schmugge, and T. Mo, *A Parameterization of Effective Soil-Temperature for Microwave Emission.* Journal of Geophysical Research-Oceans and Atmospheres, 1982. **87**(Nc2): p. 1301-1304.
87. Holmes, T.R.H., et al., *A new parameterization of the effective temperature for L band radiometry.* Geophysical Research Letters, 2006. **33**(7).
88. de Rosnay, P., et al., *SMOSREX: A long term field campaign experiment for soil moisture and land surface processes remote sensing.* Remote Sensing of Environment, 2006. **102**(3-4): p. 377-389.
89. Wen, J., et al., *Retrieval of soil moisture and vegetation water content using SSM/I data over a corn and soybean region.* Journal of Hydrometeorology, 2005. **6**(6): p. 854-863.
90. Njoku, E.G. and J.-A. Kong, *Theory for passive microwave remote-sensing of near-surface soil-moisture.* Journal of Geophysical Research, 1977. **82**(20): p. 3108-3118.
91. Jackson, T.J. and P. Oneill, *Temporal Observations of Surface Soil-Moisture Using a Passive Microwave Sensor.* Remote Sensing of Environment, 1987. **21**(3): p. 281-296.
92. Njoku, E.G. and D. Entekhabi, *Passive microwave remote sensing of soil moisture.* Journal of Hydrology, 1996. **184**(1-2): p. 101-129.
93. Owe, M. and R. De Jeu, *Surface parameter retrieval at global scales by microwave remote sensing*, in *Remote Sensing for Agriculture, Ecosystems, and Hydrology Iv*, M. Owe, G. Durso, and L. Toulios, Editors. 2003. p. 202-210.
94. Barrett, B.W., E. Dwyer, and P. Whelan, *Soil Moisture Retrieval from Active Spaceborne Microwave Observations: An Evaluation of Current Techniques.* Remote Sensing, 2009. **1**(3): p. 210-242.
95. Jackson, T.J. and D.E. LeVine, *Mapping surface soil moisture using an aircraft-based passive microwave instrument: Algorithm and example.* Journal of Hydrology, 1996. **184**(1-2): p. 85-99.
96. Schmugge, T., P.E. Oneill, and J.R. Wang, *Passive Microwave Soil-Moisture Research.* Ieee Transactions on Geoscience and Remote Sensing, 1986. **24**(1): p. 12-22.
97. Jackson, T.J., et al., *Soil moisture retrieval and AMSR-E validation using an airborne microwave radiometer in SMEX02.* Igarss 2003: Ieee International Geoscience and Remote Sensing Symposium, Vols I - Vii, Proceedings, 2003: p. 401-403
98. Ulaby, F.T., P.P. Batlivala, and M.C. Dobson, *Microwave backscatter dependence on surface-roughness, soil-moisture, and soil texture .1. Bare soil.* Ieee Transactions on Geoscience and Remote Sensing, 1978. **16**(4): p. 286-295.
99. Kerr, Y.H. and E.G. Njoku, *A Semiempirical Model for Interpreting Microwave Emission from Semiarid Land Surfaces as Seen from Space.* Ieee Transactions on Geoscience and Remote Sensing, 1990. **28**(3): p. 384-393.
100. Tian, H., et al., *Soil moisture estimation over an arid environment in Mongolia from passive microwave remote sensing based on a simplified parameterization method.* Chinese Journal of Geophysics-Chinese Edition, 2012. **55**(2): p. 415-427.

101. Njoku, E.G. and L. Li, *Retrieval of land surface parameters using passive microwave measurements at 6-18 GHz.* Ieee Transactions on Geoscience and Remote Sensing, 1999. **37**(1): p. 79-93.
102. Jackson, T.J. and T.J. Schmugge, *Passive Microwave Remote-Sensing System for Soil-Moisture - Some Supporting Research.* Ieee Transactions on Geoscience and Remote Sensing, 1989. **27**(2): p. 225-235.
103. Dobson, M.C. and F.T. Ulaby, *Active microwave soil-moisture research.* Ieee Transactions on Geoscience and Remote Sensing, 1986. **24**(1): p. 23-36.
104. Jackson, T.J., *Soil moisture estimation using special satellite microwave/imager satellite data over a grassland region.* Water Resources Research, 1997. **33**(6): p. 1475-1484.
105. Crow, W.T., M. Drusch, and E.F. Wood, *An observation system simulation experiment for the impact of land surface heterogeneity on AMSR-E soil moisture retrieval.* Ieee Transactions on Geoscience and Remote Sensing, 2001. **39**(8): p. 1622-1631.
106. Jackson, T.J. and A.Y. Hsu, *Soil moisture and TRMM microwave imager relationships in the Southern Great Plains 1999 (SGP99) Experiment.* Ieee Transactions on Geoscience and Remote Sensing, 2001. **39**(8): p. 1632-1642.
107. Schmugge, T. and T.J. Jackson, *Mapping Surface Soil-Moisture with Microwave Radiometers.* Meteorology and Atmospheric Physics, 1994. **54**(1-4): p. 213-223.
108. Chanzy, A., S. Raju, and J.P. Wigneron, *Estimation of soil microwave effective temperature at L and C bands.* Ieee Transactions on Geoscience and Remote Sensing, 1997. **35**(3): p. 570-580.
109. Wigneron, J.P., et al., *Estimating the effective soil temperature at L-band as a function of soil properties.* Ieee Transactions on Geoscience and Remote Sensing, 2008. **46**(3): p. 797-807.
110. Saleh, K., et al., *Estimates of surface soil moisture under grass covers using L-band radiometry.* Remote Sensing of Environment, 2007. **109**(1): p. 42-53.
111. Wigneron, J.P., et al., *Retrieving near-surface soil moisture from microwave radiometric observations: current status and future plans.* Remote Sensing of Environment, 2003. **85**(4): p. 489-506.
112. De Rosnay, P., et al., *Parameterizations of the effective temperature for L-band radiometry. Inter-comparison and long term validation with SMOSREX field experiment.* Mtzler, C., PW Rosenkranz, A. Battaglia and JP Wigneron (eds.)," Thermal Microwave Radiation-Applications for Remote Sensing", IET Electromagnetic Waves Series 52, London, UK, Christian Matzler (Ed.), Product code: EW 052 ISBN: 0-86341-573-3 and 978-086341-573-9, 2006. **573**.
113. Ulaby, F.T., G.A. Bradley, and M.C. Dobson, *Microwave backscatter dependence on surface-roughness, soil-moisture, and soil texture .2. Vegetation-covered soil.* Ieee Transactions on Geoscience and Remote Sensing, 1979. **17**(2): p. 33-40.
114. Peplinski, N.R., F.T. Ulaby, and M.C. Dobson, *Dielectric properties of soils in the 0.3-1.3-GHz range* Ieee Transactions on Geoscience and Remote Sensing, 1995. **33**(6): p. 1340-1340.
115. Dente, L., Z.B. Su, and J. Wen, *Validation of SMOS Soil Moisture Products over the Maqu and Twente Regions.* Sensors, 2012. **12**(8): p. 9965-9986.
116. Dente, L., et al., *Maqu network for validation of satellite-derived soil moisture products.* International Journal of Applied Earth Observation and Geoinformation, 2012. **17**: p. 55-65.
117. Su, Z., et al., *The Tibetan Plateau observatory of plateau scale soil moisture and soil temperature (Tibet-Obs) for quantifying uncertainties in coarse resolution satellite and model products.* Hydrology and Earth System Sciences, 2011. **15**(7): p. 2303-2316.
118. Su, Z., et al., *Evaluation of ECMWF's soil moisture analyses using observations on the Tibetan Plateau.* Journal of Geophysical Research: Atmospheres, 2013. **118**(11): p. 5304-5318.
119. van den Hurk, B., et al., *Acceleration Of Land Surface Model Development Over A Decade Of Glass.* Bulletin of the American Meteorological Society, 2011. **92**(12): p. 1593-1600.

120. Zhang, J.Y., L.Y. Wu, and W.J. Dong, *Land-atmosphere coupling and summer climate variability over East Asia.* Journal of Geophysical Research-Atmospheres, 2011. **116**.
121. Santanello, J.A., C.D. Peters-Lidard, and S.V. Kumar, *Diagnosing the Sensitivity of Local Land-Atmosphere Coupling via the Soil Moisture-Boundary Layer Interaction.* Journal of Hydrometeorology, 2011. **12**(5): p. 766-786.
122. van den Hurk, B. and E. van Meijgaard, *Diagnosing Land-Atmosphere Interaction from a Regional Climate Model Simulation over West Africa.* Journal of Hydrometeorology, 2010. **11**(2): p. 467-481.
123. Panciera, R., et al., *Evaluation of the SMOS L-MEB passive microwave soil moisture retrieval algorithm.* Remote Sensing of Environment, 2009. **113**(2): p. 435-444.
124. Wigneron, J.P., et al., *First evaluation of the simultaneous SMOS and ELBARA-II observations in the Mediterranean region.* Remote Sensing of Environment, 2012. **124**: p. 26-37.
125. Wigneron, J.P., et al., *Evaluating an Improved Parameterization of the Soil Emission in L-MEB (vol 49, pg 1177, 2011).* Ieee Transactions on Geoscience and Remote Sensing, 2013. **51**(5): p. 3200-3208.
126. England, A.W., *Thermal Microwave Emission from a Scattering Layer.* Journal of Geophysical Research, 1975. **80**(32): p. 4484-4496.
127. Lv, S., et al., *An improved two-layer algorithm for estimating effective soil temperature in microwave radiometry using in situ temperature and soil moisture measurements.* Remote Sensing of Environment, 2014. **152**(0): p. 356-363.
128. Bancerek, G., *The fundamental properties of natural numbers.* Formalized Mathematics, 1990. **1**(1): p. 41-46.
129. Zeng, Y.J., et al., *Diurnal soil water dynamics in the shallow vadose zone (field site of China University of Geosciences, China).* Environmental Geology, 2009. **58**(1): p. 11-23.
130. Zeng, Y., et al., *Diurnal pattern of the drying front in desert and its application for determining the effective infiltration.* Hydrology and Earth System Sciences, 2009. **13**(6): p. 703-714.
131. Hillel, D., *Introduction to environmental soil physics*. 2003: Academic press.
132. Owe, M. and A.A. Van de Griend, *Comparison of soil moisture penetration depths for several bare soils at two microwave frequencies and implications for remote sensing.* Water Resources Research, 1998. **34**(9): p. 2319-2327.
133. Ulaby, F.T., R.K. Moore, and A.K. Fung, *Microwave remote sensing active and passive-volume III: from theory to applications.* 1986: Artech House, Inc.
134. Zheng, D., et al., *Assessment of Roughness Length Schemes Implemented within the Noah Land Surface Model for High-Altitude Regions.* Journal of Hydrometeorology, 2014. **15**(3): p. 921-937.
135. Dente, L., et al., *Combined use of active and passive microwave satellite data to constrain a discrete scattering model.* Remote Sensing of Environment, 2014. **155**: p. 222-238.
136. Dente, L., et al., *Seasonality and autocorrelation of satellite-derived soil moisture products.* International Journal of Remote Sensing, 2013. **34**(9-10): p. 3231-3247.
137. Holmes, T.R.H., et al., *A global simulation of microwave emission: Error structures based on output from ECMWF's operational integrated forecast system.* Ieee Transactions on Geoscience and Remote Sensing, 2008. **46**(3): p. 846-856.
138. Zeng, Y., et al., *Numerical Analysis of Air-Water-Heat Flow in the Unsaturated Soil Is it Necessary to Consider Air Flow in Land Surface Models.* Journal of Geophysical Research-Atmospheres, 2011. **116**: doi.org/10.1029/2011JD015835.
139. Zeng, Y., et al., *A Simulation Analysis of Advective Effect on Evaporation using a Two-Phase Heat and Mass Flow Model.* Water Resources Research, 2011. **47**: doi.org/10.1029/2011WR010701.
140. Team, S.A.D. and S.S. Team, *Ancillary Data Report-Surface Temperature* Version 2 SMAP Science Document no. 051, 2015.

141. Zeng, Y., et al., *Analysis of current validation practices in Europe for space-based Climate Data Records of Essential Climate Variables.* International Journal of Applied Earth Observation and Geoinformation, 2015: p. revision before re-submission.
142. Hirschi, M., et al., *Using remotely sensed soil moisture for land-atmosphere coupling diagnostics: The role of surface vs. root-zone soil moisture variability.* Remote Sensing of Environment, 2014. **154**: p. 246-252.
143. Wen, J., et al., *New evidence for the links between the local water cycle and the underground wet sand layer of a mega-dune in the Badain Jaran Desert, China.* Journal of Arid Land, 2014: p. 1-7.
144. Su, Z., et al., *First results of the earth observation Water Cycle Multi-mission Observation Strategy (WACMOS).* International Journal of Applied Earth Observation and Geoinformation, 2014. **26**: p. 270-285.
145. Ulaby, F.T., M. Razani, and M.C. Dobson, *Effects of vegetation cover on the microwave radiometric sensitivity to soil-moisture.* Ieee Transactions on Geoscience and Remote Sensing, 1983. **21**(1): p. 51-61.
146. Sabater, J.M., P. De Rosnay, and G. Balsamo, *Sensitivity of L-band NWP forward modelling to soil roughness.* International Journal of Remote Sensing, 2011. **32**(19): p. 5607-5620.
147. Suarez, M.J., et al., *The GEOS-5 Data Assimilation System-Documentation of Versions 5.0. 1, 5.1. 0, and 5.2. 0.* 2008.
148. Rienecker, M.M., et al., *MERRA: NASA's Modern-Era Retrospective Analysis for Research and Applications.* Journal of Climate, 2011. **24**(14): p. 3624-3648.
149. Mironov, V.L. and S.V. Fomin, *Temperature Dependable Microwave Dielectric Model for Moist Soils*, in *Piers 2009 Beijing: Progess in Electromagnetics Research Symposium, Proceedings I and Ii*, J.A. Kong, Editor. 2009, Electromagnetics Acad: Cambridge. p. 831-835.
150. Reichle, R., *The MERRA-land data product.* GMAO Office Note No. 3 (Version 1.2), 2012.
151. Mialon, A., et al., *Comparison of Dobson and Mironov Dielectric Models in the SMOS Soil Moisture Retrieval Algorithm.* Ieee Transactions on Geoscience and Remote Sensing, 2015. **53**(6): p. 3084-3094.
152. Al-Yaari, A., et al., *Global-scale evaluation of two satellite-based passive microwave soil moisture datasets (SMOS and AMSR-E) with respect to Land Data Assimilation System estimates.* Remote Sensing of Environment, 2014. **149**: p. 181-195.
153. Zeng, Y., et al., *Diurnal pattern of the drying front in desert and its application for determining the effective infiltration.* Hydrol. Earth Syst. Sci., 2009. **13**(6): p. 703-714.
154. Su, Z., et al., *Evaluation of ECMWF's soil moisture analyses using observations on the Tibetan Plateau.* Journal of Geophysical Research: Atmospheres, 2013. **118**: p. 5304-5318.
155. Parrens, M., et al., *Benchmarking of L-band soil microwave emission models.* Remote Sensing of Environment, 2014. **140**: p. 407-419.
156. Panciera, R., et al., *The Soil Moisture Active Passive Experiments (SMAPEx): Toward Soil Moisture Retrieval From the SMAP Mission.* Ieee Transactions on Geoscience and Remote Sensing, 2014. **52**(1): p. 490-507.
157. Yamada, T.J., et al., *The onset of the West African monsoon simulated in a high-resolution atmospheric general circulation model with reanalyzed soil moisture fields.* Atmospheric Science Letters, 2012. **13**(2): p. 103-107.
158. Douville, H., F. Chauvin, and H. Broqua, *Influence of soil moisture on the Asian and African monsoons. Part I: Mean monsoon and daily precipitation.* Journal of Climate, 2001. **14**(11): p. 2381-2403.
159. Douville, H., et al., *Soil moisture memory and West African monsoon predictability: artefact or reality?* Climate Dynamics, 2007. **28**(7-8): p. 723-742.

160. Lim, Y.J., J. Hong, and T.Y. Lee, *Spin-up behavior of soil moisture content over East Asia in a land surface model.* Meteorology and Atmospheric Physics, 2012. **118**(3-4): p. 151-161.
161. Kerr, Y.H., *Soil moisture from space: Where are we?* Hydrogeology Journal, 2006. **15**(1): p. 117-120.
162. Dedieu, G., P.Y. Deschamps, and Y.H. Kerr, *Satellite Estimation of Solar Irradiance at the Surface of the Earth and of Surface Albedo Using a Physical Model Applied to Meteosat Data.* Journal of Climate and Applied Meteorology, 1987. **26**(1): p. 79-87.
163. Dumedah, G., J.P. Walker, and C. Rudiger, *Can SMOS Data be Used Directly on the 15-km Discrete Global Grid?* Ieee Transactions on Geoscience and Remote Sensing, 2014. **52**(5): p. 2538-2544.
164. Reul, N., et al., *SMOS satellite L-band radiometer: A new capability for ocean surface remote sensing in hurricanes.* Journal of Geophysical Research-Oceans, 2012. **117**. doi.org/10.1029/2011JC007474.
165. Tranchant, B., et al., *Expected impact of the future SMOS and Aquarius Ocean surface salinity missions in the Mercator Ocean operational systems: New perspectives to monitor ocean circulation.* Remote Sensing of Environment, 2008. **112**(4): p. 1476-1487.
166. Tranchant, B., et al., *Data assimilation of simulated SSS SMOS products in an ocean forecasting system.* Journal of Operational Oceanography, 2008. **1**(2): p. 19-27.
167. Lv, S., et al., *Determination of the Optimal Mounting Depth for Calculating Effective Soil Temperature at L-Band: Maqu Case.* Remote Sensing, 2016. **8**(6): p. 476.
168. Lv, S., et al., *An improved two-layer algorithm for estimating effective soil temperature in microwave radiometry using in situ temperature and soil moisture measurements.* Remote Sensing of Environment, 2014. **152**: p. 356-363.
169. Burke, W.J., T. Schmugge, and J.F. Paris, *Comparison of 2.8-Cm and 21-Cm Microwave Radiometer Observations over Soils with Emission Model Calculations.* Journal of Geophysical Research-Oceans and Atmospheres, 1979. **84**(Nc1): p. 287-294.
170. Rao, K., G. Chandra, and P.N. Rao, *Study on penetration depth and its dependence on frequency, soil moisture, texture and temperature in the context of microwave remote sensing.* Journal of the Indian Society of Remote Sensing, 1988. **16**(2): p. 7-19.
171. Entekhabi, D., H. Nakamura, and E.G. Njoku, *Solving The Inverse Problems For Soil-Moisture And Temperature Profiles By Sequential Assimilation Of Multifrequency Remotely-Sensed Observations.* Ieee Transactions on Geoscience and Remote Sensing, 1994. **32**(2): p. 438-448.
172. Scheeler, R., E.F. Kuester, and Z. Popovic, *Sensing Depth of Microwave Radiation for Internal Body Temperature Measurement.* Ieee Transactions on Antennas and Propagation, 2014. **62**(3): p. 1293-1303.
173. Nolan, M. and D.R. Fatland, *Penetration depth as a DInSAR observable and proxy for soil moisture.* Ieee Transactions on Geoscience and Remote Sensing, 2003. **41**(3): p. 532-537.
174. Zhao, S., et al. *An empirical model to estimate the microwave penetration depth of frozen soil*. in *Geoscience and Remote Sensing Symposium (IGARSS), 2012 IEEE International*. 2012. IEEE.
175. Lv, S., et al., *A reappraisal of global soil effective temperature schemes.* Remote Sensing of Environment, 2016. **183**: p. 144-153.
176. Zwieback, S., S. Hensley, and I. Hajnsek, *Assessment of soil moisture effects on L-band radar interferometry.* Remote Sensing of Environment, 2015. **164**: p. 77-89.
177. Zheng, D., et al., *L-Band Microwave Emission of Soil Freezesc-Thaw Process in the Third Pole Environment.* IEEE Transactions on Geoscience and Remote Sensing, 2017.
178. Zhao, H., et al., *Analysis of Soil Hydraulic and Thermal Properties for Land Surface Modelling over the Tibetan Plateau.* Earth Syst. Sci. Data Discuss., 2018. **2018**: p. 1-40.
179. Gelaro, R., et al., *The Modern-Era Retrospective Analysis for Research and Applications, Version 2 (MERRA-2).* Journal of Climate, 2017. **30**(14): p. 5419-5454.

180. Entekhabi, D., et al., *SMAP Handbook–Soil Moisture Active Passive: Mapping Soil Moisture and Freeze/Thaw from Space.* 2014.
181. Zeng, J., et al., *Evaluation of remotely sensed and reanalysis soil moisture products over the Tibetan Plateau using in-situ observations.* Remote Sensing of Environment, 2015. **163**: p. 91-110.
182. Peng, B., et al., *Reappraisal of the roughness effect parameterization schemes for L-band radiometry over bare soil.* Remote Sensing of Environment, 2017. **199**: p. 63-77.
183. Lv, S., et al., *Estimation of Penetration Depth from Soil Effective Temperature in Microwave Radiometry.* Remote Sensing, 2018. **10**(4): p. 519.
184. Zeng, Y.J., et al., *Numerical analysis of air-water-heat flow in unsaturated soil: Is it necessary to consider airflow in land surface models?* Journal of Geophysical Research-Atmospheres, 2011. **116**.
185. Zeng, Y.J., et al., *A simulation analysis of the advective effect on evaporation using a two-phase heat and mass flow model.* Water Resources Research, 2011. **47**.
186. Peplinski, N.R., F.T. Ulaby, and M.C. Dobson, *DIELECTRIC-PROPERTIES OF SOILS IN THE 0.3-1.3-GHZ RANGE.* Ieee Transactions on Geoscience and Remote Sensing, 1995. **33**(3): p. 803-807.
187. Lorenz, E.N., *Energy and Numerical Weather Prediction.* Tellus, 1960. **12**(4): p. 364-373.
188. Lorenz, E.N., *DETERMINISTIC NONPERIODIC FLOW.* Journal of the Atmospheric Sciences, 1963. **20**(2): p. 130-141.